

ABSTRACT

Title of Dissertation: NOISE CONTROL OF AN ACOUSTIC CAVITY
COUPLED WITH A VIBRATING PLATE TREATED
WITH A SPATIALLY VARYING CONSTRAINED
VISCOELASTIC LAYER

Degree candidate: Mary F. Leibolt
Degree and year: Doctor of Philosophy, 2009
Dissertation directed by: Professor Amr Baz
Department of Mechanical Engineering

Viscoelastic layers have long been recognized as an effective means of reducing the structural vibrations that can generate undesirably high pressure levels in a coupled acoustic cavity. Constraining the viscoelastic layer increases the effectiveness of the viscoelastic layer by adding transverse shear as a dissipation mechanism in the system. It is proposed in this dissertation to replace the traditionally homogeneous core of a constrained damping layer treatment by a non-homogeneous viscoelastic material in order to further improve the effectiveness of the treatment.

A finite element model is developed to simulate the vibrations of plates treated with a non-homogeneous constrained layer treatment using Reissner-Mindlin plate theory. The predictions of the model are validated against the predictions of a commercially available finite element package (NASTRAN). The model of the plate/constraining layer treatment is then coupled with a finite element model of a coupled acoustic cavity. The integrated model is exercised to consider different material combinations and geometric layouts of the non-homogeneous damping treatment in order to determine general guidelines for

producing the largest reduction in sound pressure levels inside an acoustic cavity that is being driven by a flexible boundary.

The predictions of the integrated finite element model are validated through experimental and numerical work. Close agreements are found between theoretical predictions and experimental results. Generally, it is found that damping treatments with stiffer outer perimeters and softer cores are more effective in attenuating the sound pressure levels in the acoustic cavity than other configurations of the non-homogeneous treatment.

The theoretical and experimental techniques developed in this dissertation present invaluable tools for the design and performance predictions of plates treated with spatially varying damping treatments and coupled with acoustic cavities. These tools can be extended to include more complex structural/cavity systems such as automobile, aircraft, and helicopter cabins as well as ship interior spaces.

NOISE CONTROL OF AN ACOUSTIC CAVITY COUPLED WITH
A VIBRATING PLATE TREATED WITH A SPATIALLY
VARYING CONSTRAINED VISCOELASTIC LAYER

By

Mary F. Leibolt

Dissertation submitted to the Faculty of the Graduate School of the

University of Maryland, College Park in partial fulfillment

of the requirements for the degree of

Doctor of Philosophy

2009

Advisory Committee:

Professor A. Baz, Chair/Advisor

Professor B. Balachandran

Professor D. DeVoe

Professor A. Flatau

Professor E. Smela

ACKNOWLEDGEMENTS

Thank you to the many people who supported me in this work: my advisor, Dr. Amr Baz whose patience and advice throughout the extended period of completion is much appreciated, many colleagues at work including Dr. Paul Shang who provided the initial push and Dr. Bill Martin who provided the final "shove" to get this work finished, as well as Dr. Y.N. Liu and Dr. Ranganathan Vasudevan from whom I learned so much. Thanks to Ms. Deborah Nalchajian of ONR for providing the funding which resulted in the completion of this study. Finally, thanks to my family for their love and support, especially my wonderful husband Ed.

TABLE OF CONTENTS

List of Tables	v
List of Figures	vi
List of Abbreviations	x
Chapter 1: Introduction	1
1.1 Background.....	1
1.2 Scope of Dissertation.....	7
Chapter 2: Variational Modeling for Plates with Spatially Varying Moduli	9
2.1 Plate Theory.....	9
2.2 Reissner-Mindlin Plate Theory Assuming $E=E(x,y)$	10
2.3 Kirchoff (Thin) Plate Theory Assuming $E=E(x,y)$	19
2.4 Summary.....	25
Chapter 3: Preliminary Experimental Work	26
3.1 Experimental Setup.....	26
3.2 Configurations for Preliminary Experiment.....	30
3.3 Results.....	31
3.4 Summary.....	42
Chapter 4: Generation of Dataset for Validation of Finite Element Model	43
4.1 Plate Model.....	43
4.2 Cavity Model.....	46
4.3 Loading	48
4.4 Viscoelastic and Constraining Layer Models.....	50
4.5 Summary.....	53
Chapter 5: Finite Element Model of Viscoelastically Damped Plates Coupled with an Acoustic Cavity	54
5.1 Finite Element Model for Untreated Plate – Strain Energy	54
5.2 Discretization.....	56
5.3 Finite Element Model for Untreated Plate – Kinetic Energy	63
5.4 Finite Element Model– Load Vector.....	64
5.5 Finite Element Model for Acoustic Cavity.....	65
5.6 Acoustic Cavity Discretization.....	67
5.7 Fluid Structure Coupling.....	68
5.8 Finite Element Model for Viscoelastic Three Layer Plate Element.....	68
5.9 Kinematics for Three Layer Plate.....	69

5.10	Finite Element Model for Three Layer Plate – Strain Energy.....	74
5.11	Discretization for Three Layer Plate.....	77
5.12	Finite Element Model for Three Layer Plate – Kinetic Energy.....	78
5.13	Summary.....	80
Chapter 6: Validation of Finite Element Model of Plate/Cavity System.....		
6.1	Introduction.....	82
6.2	Base Plate Element.....	83
6.3	Acoustic Element.....	84
6.4	Coupled Plate and Cavity	85
6.5	Three Layer Plate Element	87
6.6	Summary	96
Chapter 7: Comparison of Geometrical Layouts for Constrained Layer Treatments.....		
7.1	Introduction.....	97
7.2	Single Material Property Variation	97
7.3	Geometric Layouts.....	105
7.4	Mixed Material Parametric Study Results.....	107
7.5	Displacements, Pressure Contours and Strains.....	111
7.6	Summary.....	118
Chapter 8: More Experimental Validation of Finite Element Model of Plate/Cavity System		
8.1	Experimental Setup.....	119
8.2	Experimental Results.....	122
8.3	Summary.....	125
Chapter 9: Conclusions and Recommendations.....		
9.1	Conclusions.....	126
9.2	Recommendations.....	127

LIST OF TABLES

Table 3.1:	Area under pressure spectra for each configuration	38
Table 4. 1:	A comparison of the eigenvalues calculated for some different mesh sizes and element types.....	46
Table 6.1:	Comparison of analytical solution, NASTRAN and MFLFE eigen values for an untreated plate.....	84
Table 6.2:	Comparison of analytical solution, NASTRAN and MFLFE eigen values for an acoustic cavity.....	85
Table 6.3:	Comparison of NASTRAN and MFLFE eigenvalues for a coupled plate and acoustic cavity.....	86

LIST OF FIGURES

Figure 1.1:	Frequency response of beam treated with multi-viscoelastic material	6
Figure 2.1	Coordinate system for plate.....	10
Figure 3.1:	Sketch of experimental setup for preliminary experiment.....	26
Figure 3.2:	Connections diagram for preliminary experiment.....	27
Figure 3.3:	Sketch of the four viscoelastic layer configurations.....	28
Figure 3.4:	Shear modulus G' and loss factor for viscoelastic materials.....	29
Figure 3.5:	Comparison of pressure levels for the four constrained viscoelastic layers.....	32
Figure 3.6:	Comparison of constrained layer pressure levels with those of an untreated plate.....	35
Figure 3.7:	Ambient data for inside and outside microphones.....	37
Figure 3.8:	The frequency response of the untreated plate	39
Figure 3.9:	LDV displacement measurement for untreated plate at first five resonance peaks.....	41
Figure 3.10:	Displacement patterns at the first resonance for the four constrained viscoelastic layers.....	42
Figure 4.1:	A comparison of wavelengths for different wave types.....	44
Figure 4.2:	Comparison of NASTRAN results with experimental data for the untreated plate/cavity system.....	49
Figure 4.3:	Comparison of NASTRAN model and experimental pressure data for unconstrained viscoelastic configurations.....	51
Figure 4.4:	Comparison of experimental pressure data and NASTRAN model for constrained configurations.....	52
Figure 5.1:	Geometry for plain plate kinematics.....	54
Figure 5.2:	Four node quadrilateral element.....	57

Figure 5.3:	Geometry for kinematics of three layer plate	69
Figure 5.4:	Angles for extensions in viscoelastic and constraining layers.....	70
Figure 5.5:	Model for the extensional displacements in the viscoelastic and constraining layers – exact expression and approximation	72
Figure 6. 1:	Comparison between MFLFE numerical pressure data and preliminary experiment pressure data for an untreated plate.....	86
Figure 6. 2:	Three possible configurations of three layer element.....	88
Figure 6. 3:	Comparison between MFLFE numerical pressure data and preliminary experiment pressure data for a plate with an unconstrained viscoelastic layer	89
Figure 6. 4:	Comparison between MFLFE numerical pressure data and preliminary experiment pressure data for a plate with a constrained single material viscoelastic layer	91
Figure 6. 5:	Comparison between MFLFE numerical pressure data and preliminary experiment pressure data for a plate with an unconstrained single material viscoelastic layer. Bolted boundary conditions	93
Figure 6. 6:	Comparison between MFLFE numerical pressure data and preliminary experiment pressure data for a plate with a constrained single material viscoelastic layer. Bolted boundary conditions	94
Figure 6. 7	Comparison between MFLFE numerical pressure data and preliminary experiment pressure data for a plate with a multiple material constrained viscoelastic layer	95
Figure 7. 1a	Pressures predicted in the acoustic cavity using MFLFE and parametric variation of Young's modulus in the viscoelastic layer for SC 601.....	98
Figure 7. 1b:	Pressures predicted in the acoustic cavity using MFLFE and parametric variation of the density in the viscoelastic layer for SC 601 (full frequency range)	99

Figure 7. 1c:	Pressures predicted in the acoustic cavity using MFLFE and parametric variation of the loss factor in the viscoelastic layer for SC 601(zoom).....	99
Figure 7. 2a:	Pressures predicted in the acoustic cavity using MFLFE and parametric variation of the density in the viscoelastic layer for SC 609 (Full frequency range).....	101
Figure 7. 2b:	Pressures predicted in the acoustic cavity using MFLFE and parametric variation of Young's modulus in the viscoelastic layer for SC 609.....	101
Figure 7. 2c:	Pressures predicted in the acoustic cavity using MFLFE and parametric variation of loss factor in the viscoelastic layer for SC 609 (zoom).....	102
Figure 7. 3a:	Sketch of the nomograph for SC 609.	103
Figure 7. 3b:	Sketch of the nomograph for SC 601.	104
Figure 7. 4:	Geometric layouts of the multi-viscoelastic material treatments....	106
Figure 7. 5a	Mixed material coinfiguration calculated pressure spectra (full frequency range).....	107
Figure 7. 5b	Mixed material coinfiguration calculated pressure spectra (zoom).....	108
Figure 7.6a:	Sorted mixed material configuration calculated pressure spectra-less effective configurations(zoom).....	109
Figure 7.6b:	Sorted mixed material configuration calculated pressure spectra- more effective configurations(zoom).....	110
Figure 7.7:	Out of plane displacements predicted by MFLFE in the treated region for various geometric layouts.....	111
Figure 7.8:	Pressure contour plots in the yz direction calculated by MFLFE.....	113
Figure 7.9:	Pressure contour plots in the xy plane at the microphone position.....	115
Figure 7.10:	Strain energy calculated on the plate for various configurations.....	117

Figure 8.1:	Experimental apparatus. Internal microphone, external microphone, flexible plate.....	120
Figure 8.2	Mixed material configurations used in final experiment.....	122
Figure 8.3a:	Comparison of the experimental pressure spectra for constrained layer treatments, for both single material and mixed material viscoelastic cores.....	123
Figure 8.3b:	Comparison of the predicted (MFLFE) pressure spectra for constrained layer treatments, for both single material and mixed material viscoelastic cores.....	123
Figure 8.3c:	Comparison of the predicted (MFLFE) and experimental pressure spectra for constrained layer treatments, for both single material and mixed material viscoelastic cores	124

LIST OF ABBREVIATIONS

Symbols

x, y, z	- Cartesian coordinate system
r, s	- element coordinate system
$\tilde{u}, \tilde{v}, \tilde{w}$	- actual displacements
$u, v, w, \theta_x, \theta_y$	- displacements as modeled
h	- plate thickness
E	- Young's modulus
L_d	- diffusion length
G	- shear modulus
ρ	- density
ν	- Poisson's ratio
U	- strain (potential) energy (PE)
T	- kinetic energy (KE)
Π	- system energy potential
Γ	- boundary
Ω	- interior domain
t	- time
n_x, n_y	- direction cosines
M_{xx}, M_{yy}, M_{xy}	- bending moments
F_{xx}, F_{yy}	- normal forces
V_{xz}, V_{yz}	- shear forces
ϵ	- normal strain
γ	- shear strain
W	- work energy
q_u, q_u	- distributed load
N_i	- shape function
σ	- stress
D	- bending stiffness

K	- stiffness matrix
M	- mass matrix
Q	- fluid/structure coupling
∇	- gradient operator
ϕ	- velocity potential
S	- length along boundary
p	- pressure
v_f	- fluid particle displacement
v_n	- displacement normal to fluid boundary
c	- speed of sound
a	- displacement vector
J	- Jacobian

Superscripts, Subscripts

B	- bending
LS	- longitudinal shear
TS	- transverse shear
T	- transpose of matrix
x,y,z	- Cartesian coordinate system
r,s	- element coordinate system
b	- base plate
v	- viscoelastic layer
cl	- constraining layer

Acronyms

MFLFE	Name of program developed in this study (MFL -author's initials - Finite Element)
NASTRAN	Name of commercial code used in this study (NAsa STRuctural ANalysis)

Chapter 1

Introduction

1.1 Background

It is of interest to those who are concerned with the design and use of vehicles, to be able to lower sound pressure levels within enclosed spaces. Frequently, the primary cause of high sound pressure levels within a cavity is the vibration of part of the structure that forms the boundaries of the cavity. Such structural vibrations cause the fluid within the cavity to move and pressure waves to be generated. In general, decreasing the amount of vibration experienced by the structural members lessens the amount of kinetic energy in the system and decreases the magnitude of the sound pressure inside the cavity.

The use of viscoelastic layers has long been recognized as an effective means of dissipating structural energy into heat. Typically, a thin layer of viscoelastic material is bonded to the structural member that has been identified as a source for the cavity pressure field. As discussed by Kerwin in 1959, dissipation occurs when there are extensional displacement and/or transverse shear deformation in the viscoelastic material. Additionally, application of a thin constraining layer to the outside surface of the viscoelastic layer increases the amount of transverse shear deformation present, and thereby increases the amount of structural energy dissipated by the layer.

In 1959, Kerwin developed an expression to describe the distance away from the point where a load is applied that a “localized shear deformation will make itself felt.” This quantity L_d , which is called “*the diffusion length*”, is expressed as

$$L_d = \frac{h_v h_{cl} E_{cl}}{G}$$

where h_v and h_{cl} are the thicknesses of the viscoelastic layer and constraining layer respectively, E_{cl} is the Young's Modulus of the constraining layer and G is the magnitude of the complex shear modulus of the viscoelastic layer. Shear is greatest at the point of load application and decreases to a very small value at L_d .

In 1962, Parfitt exploited this idea and introduced the concept of cutting the constraining layers at intervals to increase the regions of high transverse shear in the viscoelastic layer. He discusses the frequency dependency of the effectiveness of this technique.

Plunkett and Lee presented an analysis in 1970 that sought to optimize the length between cuts in the constraining layer with respect to maximizing the layer's ability to dissipate structural energy. They developed an expression for a system loss factor and extended their analysis to multiple layers through the thickness. Plunkett and Lee also presented plots of the transverse shear versus distance with the ratio of beam length to L_d as a parameter in their paper.

In many situations, for example in underwater vehicle applications, the cuts in a constraining layer render it more susceptible to damage while the vehicle is moving. With the goal of increasing the amount of transverse shear deformation in the viscoelastic material while leaving the constraining layer intact, it is proposed in this dissertation, that a viscoelastic layer formed of multiple materials with unlike material moduli be constructed and tested. Since the strain energy is the integrated product of the shear modulus and the shear strain squared, having material with a high shear modulus in the region of high shear strain will increase the amount of strain energy dissipated by the treatment. The variation of the viscoelastic material properties is limited in this

dissertation to variation in the in-plane direction. But, for the entire damping treatment including the constraining layer, the material properties vary also in the transverse direction.

Many investigations pertaining to the effects of material variation through the thickness direction have been performed. Reissner authored the classic paper “*On the Bending of Elastic Plates*” (1947) in which he presented his new plate theory and a system of equations for a sandwich plate. Such a topic was of great interest in the late 1940s and early 1950s as reported, for example, by Hoff and Mautner (1948). This work was extended by others to include multiple layer sandwich structures in the late 1960s (e.g. Kao (1966), Liaw and Little (1967)). The general approach in these studies was to generate a total energy expression for the multi-layered system that combined appropriate contributions for each layer. For example, it may be assumed that the constraining (facing) layers have no significant shearing energy while the energy summation in the core is dominated by shear energy. Typically these papers deal with materials suitable for an airframe structure, for example, aluminum facings and balsa cores. The dissipation of structural energy by the core was not the primary focus. Later, this analytical work was used as a basis for developing finite element models of multilayer structures (e.g., Khatua and Cheung (1970)).

Constrained layers are another special case of material nonhomogeneity in the thickness direction. Kerwin (1962), Lazan (1965), Plunkett and Lee (1970), and others studied configurations of multiple layers of constrained viscoelastic materials. Here, the studies worked with cores made of viscoelastic materials whose energy dissipation properties needed to be included in any modeling. The primary focus of these studies was

the generation of an accurate prediction of the energy dissipated by the multilayer plate system.

As the tools of finite element analysis became more powerful they were employed in the task of analyzing structures with viscoelastic and constrained layer damping. Johnson and Kienholz (1981) introduced various approaches including modeling the viscoelastic material as having a frequency dependent complex material modulus, calculating the response in the frequency domain, and calculating the undamped normal modes then applying a frequency dependent loss factor to the fraction of the strain energy for each mode from the viscoelastic core. Such approaches form the basis of the Modal Strain Energy (MSE) method. In the 1990s, methods that used internal degrees of freedom to capture the viscoelastic layer's dissipation of energy were developed (e.g. Yiu 1993, McTavish and Hughes 1993, Lesieutre and Bianchini 1989).

Eventually, Reissner's concept of summing the strain energy of the three layers was used in finite element modeling so that a single element could be used to model the three layers of a constrained viscoelastic layer. This technique was combined with the various approaches to viscoelastic modeling. In a 1995 paper, Baz and Ro used a three layer finite element model with the complex modulus approach to model the viscoelastic layer. A Kirchhoff model that included bending and extensional displacements was used for the base plate and constraining layer while the viscoelastic layer was modeled to include transverse shear displacement also. In 1996, Lesieutre and Lee used a similar approach on a beam configuration but modeled the viscoelastic layer with their "Anelastic Displacement Field (ADF)" technique, a method using internal degrees of freedom to model the viscoelastic dissipation.

As mentioned above, modeling the variation of material properties in the transverse (out-of-plane) direction has been studied by many, including those researchers interested in airframe structures and those interested in damping layers. Through the early 1990s, these studies usually handled the variation of material by treating the layers as discrete quantities and summing the contribution of each layer to the total system energy.

Starting in the late 1980s another engineering area of research developed which studied the variation of material properties within a material. These investigations examined materials that came to be called functionally graded materials. Since the impetus behind these investigations was the desire to develop materials that could perform well with very different boundary conditions on the inside and outside surfaces, a large majority of the papers that deal with functionally graded materials study configurations that vary in the transverse direction (e.g., Sutradhar *et al.* 2002, Venkataraman and Sankar 2001) although there has been some development of three dimensional modeling of material variation (e.g. Aboudi *et al.* 1999). These studies did not deal with coupling structural motion to an internal pressure field.

Less work has been presented regarding material variation in the in-plane direction. However, in 2002 Kim and Paulino presented a development of plate elements that have material properties that have in-plane gradation. The finite element model that was developed allowed both linear and exponential spatial variation of material properties. However, dissipation of structural energy by lossy materials is not included in the development.

In 2003, Bigili presented his three dimensional analysis of large deformations in an elastomeric material. However, he modeled the elastomeric material using

hyperelasticity concepts, so structural dissipation of energy by the elastomer is not modeled.

In 2003, Baz *et al.* studied the frequency response of beams treated with multi-material constrained layers. In their study, aluminum beams were treated with a full length layer of a relatively soft material (Dyad 601 from Soundcoat, Deer Park, New York, www.soundcoat.com), a partial treatment of Dyad 601 and a partial treatment of a combination of Dyad 601 and a somewhat stiffer material (Dyad 606).

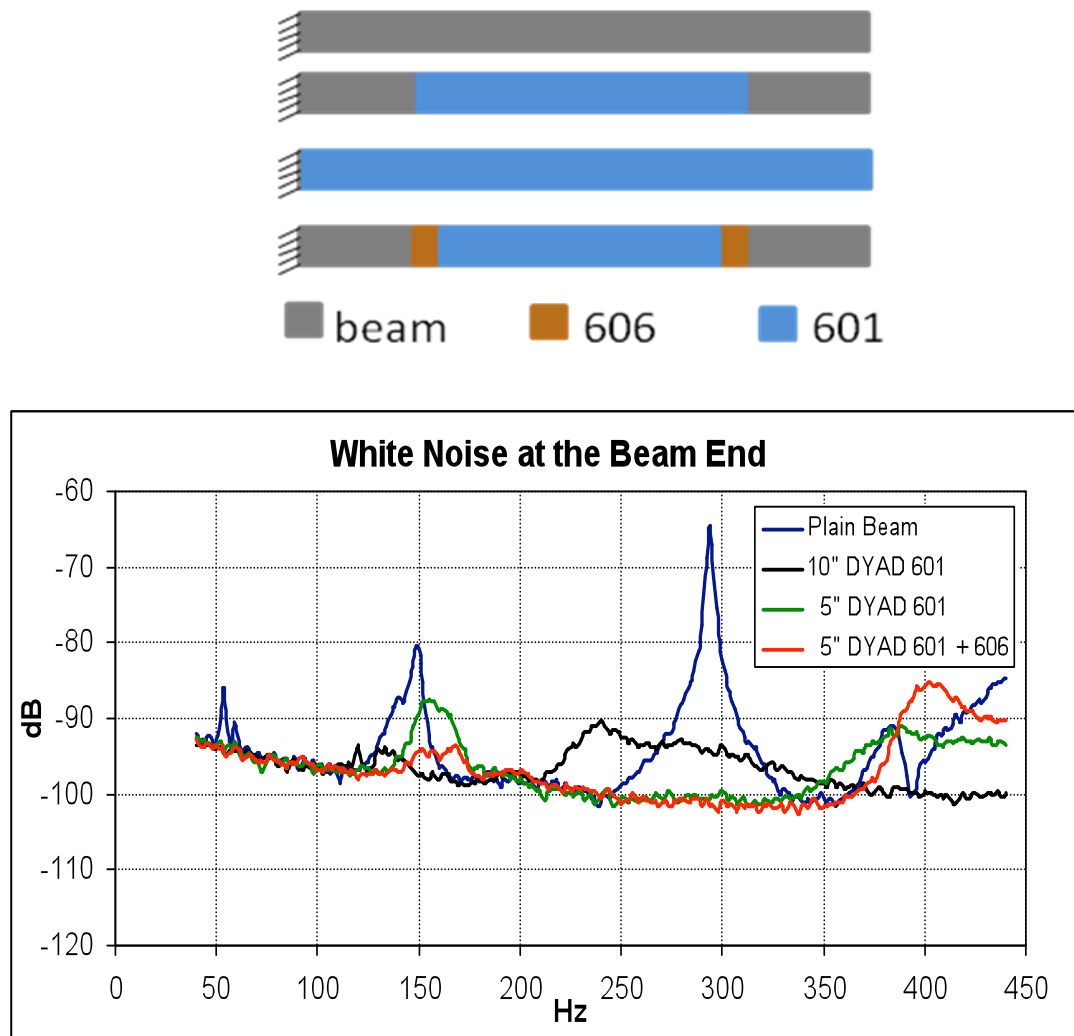


Figure 1.1: Frequency response of beam treated with multi-viscoelastic material (Baz *et al.*, 2003)

As illustrated in Figure 1.1, it is confirmed that the concept hold promise. It is observed that for frequencies up to 350 Hz, the mixed material partial treatment performed better than the partial single material treatment. This indicated benefit in further investigation of the concept.

1.2 Scope of Dissertation

This dissertation will explore experimentally the use of a constrained viscoelastic layer whose core has material properties that vary in-plane in a two-dimensional geometry to lower sound pressure levels inside a coupled acoustic cavity. After testing the concept experimentally, a finite element model is developed to allow parametric studies of different material combinations and geometric layouts. The finite element model simulates the vibration of plates treated with three-layer damping treatment. The viscoelastic layer has material properties that vary in the in-plane direction, and dissipation by the viscoelastic layer is modeled using the complex material modulus approach. Results from the parametric study are verified numerically and experimentally.

In this chapter, a review of pertinent literature was presented. Chapter 2 will explore the appropriateness of various plate theory formulations and determine how spatially varying moduli affect the formulation of the equations that are the basis of finite element formulation. In Chapter 3, the development of finite elements necessary to model the plate-cavity system is discussed. The information regarding the initial experiment performed for this work is introduced in Chapter 4, while Chapter 5 presents

details regarding numerical validation purposes. Chapter 6 discusses the validation process used in the development of the finite element model, and Chapter 7 presents the parametric study performed for this investigation. Finally, the experimental validation is presented in Chapter 8. Chapter 9 summarizes the conclusions and recommendations that are arrived at in this dissertation

Chapter 2

Variational Modeling Of Plates With Spatially Varying Moduli

2.1 Plate Theory

Plate theory is an approximation in structural mechanics that assumes that knowledge of motion at the mid-plane of the plate is adequate to describe the motion of the plate. In this dissertation, “*Reissner-Mindlin plate theory*” will be used to refer to plate theory that includes the effects of transverse shear deformation through the plate’s thickness while the term “*Kirchoff plate theory*” will refer to plate theory that does not. Typically, the assumptions in plate theory are stated to be:

- 1) Particles along a straight line perpendicular to the undeformed mid-plane remain in a straight line when the plate is deformed. In *Kirchoff plate theory*, it is further assumed that the straight line remains perpendicular to the mid-plane after deformation (rigid body rotation).
- 2) Strain in the z direction (perpendicular to the plane of the plate) is negligible.

The particulars of this study justify the further assumption that displacements are small and that Hooke’s Law:

$$\sigma_{ij} = C_{ijkl} \epsilon_{kl}$$

may be used to describe the constitutive relationship between stress and strain. We assume in this study that the material is isotropic (no preferred direction in material) but not homogeneous since the moduli are dependent on spatial location

2.2 Reissner-Mindlin Plate Theory Assuming $E=E(x,y)$

Taking the mid-plane of the plate to be $z = 0$ for a plate with a coordinate system as shown in Figure 2.1, we can write the following expressions for the displacement, strain and stress in Reissner-Mindlin theory.

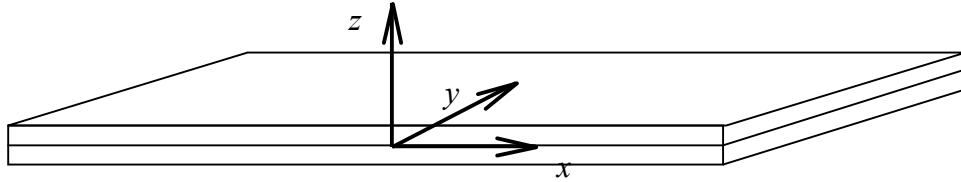


Figure 2. 1: Coordinate system of the plate

Displacements:

$$\tilde{u} \approx u(x,y,t) - z\theta_x(x,y,t) \quad \tilde{v} \approx v(x,y,t) - z\theta_y(x,y,t) \quad \tilde{w} \approx w(x,y,t) \quad (2.1)$$

Strains:

$$\begin{aligned} \varepsilon_{xx} &= \frac{\partial \tilde{u}}{\partial x} = \frac{\partial u}{\partial x} - z \frac{\partial \theta_x}{\partial x} & \varepsilon_{yy} &= \frac{\partial \tilde{v}}{\partial y} = \frac{\partial v}{\partial y} - z \frac{\partial \theta_y}{\partial y} \\ \varepsilon_{zz} &= \frac{\partial \tilde{w}}{\partial z} = 0 \\ \gamma_{xy} &= \frac{\partial \tilde{u}}{\partial y} + \frac{\partial \tilde{v}}{\partial x} = \frac{\partial u}{\partial y} + \frac{\partial v}{\partial x} - z \left(\frac{\partial \theta_x}{\partial y} + \frac{\partial \theta_y}{\partial x} \right) & \gamma_{xz} &= \frac{\partial \tilde{u}}{\partial z} + \frac{\partial \tilde{w}}{\partial x} = \frac{\partial w}{\partial x} - \theta_x \\ \gamma_{yz} &= \frac{\partial \tilde{v}}{\partial z} + \frac{\partial \tilde{w}}{\partial y} = \frac{\partial w}{\partial y} - \theta_y \end{aligned} \quad (2.2)$$

Stresses:

$$\begin{aligned}
\sigma_{xx} &= \frac{E}{1-\nu^2} (\varepsilon_{xx} + \nu \varepsilon_{yy}) = \frac{E}{1-\nu^2} \left(\left(\frac{\partial u}{\partial x} + \nu \frac{\partial v}{\partial y} \right) - z \left(\frac{\partial \theta_x}{\partial x} + \nu \frac{\partial \theta_y}{\partial y} \right) \right) \\
\sigma_{yy} &= \frac{E}{1-\nu^2} (\varepsilon_{yy} + \nu \varepsilon_{xx}) = \frac{E}{1-\nu^2} \left(\left(\frac{\partial v}{\partial y} + \nu \frac{\partial u}{\partial x} \right) - z \left(\frac{\partial \theta_y}{\partial y} + \nu \frac{\partial \theta_x}{\partial x} \right) \right) \\
\sigma_{zz} &= 0 \\
\sigma_{xy} &= G \gamma_{xy} = G \left(\left(\frac{\partial u}{\partial y} + \frac{\partial v}{\partial x} \right) - z \left(\frac{\partial \theta_x}{\partial y} + \frac{\partial \theta_y}{\partial x} \right) \right) \\
\sigma_{xz} &= G \gamma_{xz} = G \left(\frac{\partial w}{\partial x} - \theta_x \right) \\
\sigma_{yz} &= G \gamma_{yz} = G \left(\frac{\partial w}{\partial y} - \theta_y \right)
\end{aligned} \tag{2.3}$$

In these expressions \tilde{u} , \tilde{v} , and \tilde{w} are the x , y and z displacements and u, v, w, θ_x and θ_y are independent functions of x and y . The angle θ (which has specific instances as θ_x and θ_y) is the sum of a shear angle α and a bending angle β ($\theta = \alpha + \beta$). E is Young's modulus, ν is Poisson's ratio, and $G = E/2(1 + \nu)$ is the shear modulus. E and G are functions of x and y in this study.

To generate equations of motion for a *Reissner-Mindlin plate* with spatially variable material properties we will develop expressions for kinetic energy, strain energy and work. Then using Hamilton's Principle we will generate equilibrium equations.

Strain energy:

$$U = \frac{1}{2} \int_{\Omega} (\sigma_{xx} \varepsilon_{xx} + \sigma_{yy} \varepsilon_{yy} + \sigma_{xy} \varepsilon_{xy} + \sigma_{xz} \varepsilon_{xz} + \sigma_{yz} \varepsilon_{yz} +) d\Omega$$

Here Ω is the domain of interest. When expressions for stress and strain are substituted into the expression for strain energy, and z is integrated over the thickness of the plate, the result is

$$\begin{aligned}
 U &= U_B + U_S & U_B &= U_B(w, \theta_x, \theta_y) & U_S &= U_S(u, v) \\
 U_B &= \frac{1}{2} \int_{\Omega} \left\{ \begin{aligned} & D \left(\left(\frac{\partial \theta_x}{\partial x} \right)^2 + 2\nu \frac{\partial \theta_x}{\partial x} \frac{\partial \theta_y}{\partial y} + \left(\frac{\partial \theta_y}{\partial y} \right)^2 + \frac{1-\nu}{2} \left(\frac{\partial \theta_y}{\partial x} + \frac{\partial \theta_x}{\partial y} \right)^2 \right) \\ & + G h \left(\left(\frac{\partial w}{\partial x} - \theta_x \right)^2 + \left(\frac{\partial w}{\partial y} - \theta_y \right)^2 \right) \end{aligned} \right\} d\Omega & (2.4) \\
 U_S &= \frac{1}{2} \int_{\Omega} \left\{ \tilde{E} h \left(\left(\frac{\partial u}{\partial x} \right)^2 + 2\nu \frac{\partial u}{\partial x} \frac{\partial v}{\partial y} + \left(\frac{\partial v}{\partial y} \right)^2 + \frac{1-\nu}{2} \left(\frac{\partial u}{\partial y} + \frac{\partial v}{\partial x} \right)^2 \right) \right\} d\Omega
 \end{aligned}$$

where

$$D = \frac{E h^3}{12(1-\nu^2)} \quad G = \frac{E}{2(1+\nu)} \quad \tilde{E} = \frac{E}{1-\nu^2} \quad (2.5)$$

and h is the thickness of the plate.

To generate an expression for kinetic energy in terms of u , v , w , θ_x and θ_y , the expressions for displacement are substituted into the expression for kinetic energy:

Kinetic energy:

$$\begin{aligned}
 T &= \frac{1}{2} \int_{\Omega} \left(\dot{u}^2 + \dot{v}^2 + \dot{w}^2 \right) d\Omega \\
 T &= T_{B,TS} + T_{LS} \\
 T_{LS} &= T_{LS}(u, v) & T_{B,TS} &= T_{B,TS}(w, \theta_x, \theta_y) & (2.6) \\
 T_{LS} &= \frac{1}{2} \int_{\Omega} \rho h \left(\left(\frac{\partial u}{\partial t} \right)^2 + \left(\frac{\partial v}{\partial t} \right)^2 \right) d\Omega \\
 T_{B,TS} &= \frac{1}{2} \int_{\Omega} \left(\rho h \left(\frac{\partial w}{\partial t} \right)^2 + \frac{\rho h^3}{12} \left(\left(\frac{\partial \theta_x}{\partial t} \right)^2 + \left(\frac{\partial \theta_y}{\partial t} \right)^2 \right) \right) d\Omega
 \end{aligned}$$

The final expression contains terms due to both translation and rotation. We will consider first the energy terms associated with out-of-plane motion. Hamilton's Principle for these terms may be written as

$$\begin{aligned}
 H &= \int_{t_1}^{t_2} (T_B - U_B + W_B) dt \\
 \delta H &= \int_{t_1}^{t_2} (\delta T_B - \delta U_B + \delta W_B) dt = 0 \qquad \delta W_B = \delta(-qw) \\
 \int_{t_1}^{t_2} \frac{1}{2} \int_{\Omega} \delta \left\{ \begin{array}{l} \left[\rho h \left(\frac{\partial w}{\partial t} \right)^2 + \frac{\rho h^3}{12} \left(\left(\frac{\partial \theta_x}{\partial t} \right)^2 + \left(\frac{\partial \theta_y}{\partial t} \right)^2 \right) \right] \\ - Gh \left(\left(\frac{\partial w}{\partial x} - \theta_x \right) + \left(\frac{\partial w}{\partial y} - \theta_y \right) \right) \\ - \left[D \left(\left(\frac{\partial \theta_x}{\partial x} \right)^2 + 2\nu \frac{\partial \theta_x}{\partial x} \frac{\partial \theta_y}{\partial y} + \frac{1-\nu}{2} \left(\frac{\partial \theta_y}{\partial x} + \frac{\partial \theta_x}{\partial y} \right)^2 \right) \right] - qw \end{array} \right\} d\Omega dt = 0 \quad (2.7)
 \end{aligned}$$

where δW is the contribution of the energy in the system due to surface and body forces represented by q . Carrying out the variation of T_B and U_B according to the rule

$$\delta H = \frac{\partial H}{\partial \alpha} \delta \alpha$$

and performing integration by parts as necessary allows us to generate equilibrium equations. Note that since the moduli are functions of spatial variables, integration by parts now generates terms with odd order derivatives of the independent functions. To demonstrate this, look at the variation and integration by parts for one term

in U_B :

$$\begin{aligned}
\delta \left(\int_{t_1}^{t_2} \int_{\Omega} D \left(\frac{\partial \theta_x}{\partial x} \right)^2 d\Omega dt \right) &= \int_{t_1}^{t_2} \int_{\Omega} 2D \frac{\partial \theta_x}{\partial x} \frac{\partial \delta \theta_x}{\partial x} d\Omega dt \\
&= \int_{t_1}^{t_2} \left\{ \oint_{\Gamma} 2D \frac{\partial \theta_x}{\partial x} \delta \theta_x n_x d\Gamma - \int_{\Omega} 2D \frac{\partial^2 \theta_x}{\partial x^2} \delta \theta d\Omega - \int_{\Omega} 2 \frac{\partial D}{\partial x} \frac{\partial \theta_x}{\partial x} \delta \theta d\Omega \right\} dt
\end{aligned}$$

boundary term
even order derivative
odd order derivative

Here, n_x and n_y are the direction cosines between the normal to the boundary Γ and the x or y axis ($dx = n_x d\Gamma$). Carrying through the variation and integration by parts for all terms in T_B and U_B yields the following equilibrium equations for a plate with spatially variable material properties:

$$\delta \theta_x : \left[\begin{aligned} & D \left(\frac{\partial^2 \theta_x}{\partial x^2} + \nu \frac{\partial^2 \theta_y}{\partial x \partial y} + \frac{1-\nu}{2} \left(\frac{\partial^2 \theta_y}{\partial x \partial y} + \frac{\partial^2 \theta_x}{\partial y^2} \right) \right) \\ & + \frac{\partial D}{\partial x} \left(\frac{\partial \theta_x}{\partial x} + \nu \frac{\partial \theta_y}{\partial y} \right) + \frac{1-\nu}{2} \frac{\partial D}{\partial y} \left(\frac{\partial \theta_x}{\partial y} + \frac{\partial \theta_y}{\partial x} \right) \\ & - Gh \left(\frac{\partial w}{\partial x} - \theta_x \right) - \frac{\rho h^3}{12} \frac{\partial^2 \theta_x}{\partial t^2} \end{aligned} \right] = 0 \quad (2.8a)$$

$$\delta \theta_y : \left[\begin{aligned} & D \left(\frac{\partial^2 \theta_y}{\partial y^2} + \nu \frac{\partial^2 \theta_x}{\partial x \partial y} + \frac{1-\nu}{2} \left(\frac{\partial^2 \theta_x}{\partial x \partial y} + \frac{\partial^2 \theta_y}{\partial x^2} \right) \right) \\ & + \frac{\partial D}{\partial y} \left(\frac{\partial \theta_y}{\partial y} + \nu \frac{\partial \theta_x}{\partial x} \right) + \frac{1-\nu}{2} \frac{\partial D}{\partial x} \left(\frac{\partial \theta_x}{\partial y} + \frac{\partial \theta_y}{\partial x} \right) \\ & - Gh \left(\frac{\partial w}{\partial y} - \theta_y \right) - \frac{\rho h^3}{12} \frac{\partial^2 \theta_y}{\partial t^2} \end{aligned} \right] = 0 \quad (2.8b)$$

$$\delta w : \left[\begin{aligned} & Gh \left(\frac{\partial^2 w}{\partial x^2} + \frac{\partial^2 w}{\partial y^2} - \frac{\partial \theta_y}{\partial x} - \frac{\partial \theta_x}{\partial y} \right) + \\ & h \left(\frac{\partial G}{\partial x} \left(\frac{\partial w}{\partial x} - \theta_x \right) + \frac{\partial G}{\partial y} \left(\frac{\partial w}{\partial y} - \theta_y \right) \right) - \frac{\rho h^3}{12} \frac{\partial^2 w}{\partial t^2} \end{aligned} \right] = 0 \quad (2.8c)$$

with boundary conditions (one from each group):

$$\{\theta_x = 0 \quad \theta_y = 0 \quad w = 0\}$$

$$\left\{ \begin{array}{l} M_{xx} = D \left(\frac{\partial \theta_x}{\partial x} + \nu \frac{\partial \theta_y}{\partial y} \right) \quad M_{yy} = D \left(\frac{\partial \theta_y}{\partial y} + \nu \frac{\partial \theta_x}{\partial x} \right) \quad M_{xy} = D \frac{1-\nu}{2} \left(\frac{\partial \theta_x}{\partial y} + \frac{\partial \theta_y}{\partial x} \right) \\ V_{xz} = Gh \left(\frac{\partial w}{\partial x} - \theta_x \right) \quad V_{yz} = Gh \left(\frac{\partial w}{\partial y} - \theta_y \right) \end{array} \right\}$$

We can go back to a symmetric formulation that is useful for generating stiffness and mass matrices by applying the principle of virtual work to the equations. The equilibrium equations are multiplied by an appropriate virtual displacement and then integrated over the surface Ω . Integration by parts is performed and the variables in the resulting equation are discretized to generate the matrices used in finite element formulations. For example, virtual work for the θ_x equilibrium equation is:

$$\int_{\Omega} \delta \theta_x \left[D \left(\frac{\partial^2 \theta_x}{\partial x^2} + \nu \frac{\partial^2 \theta_y}{\partial x \partial y} + \frac{1-\nu}{2} \left(\frac{\partial^2 \theta_y}{\partial x \partial y} + \frac{\partial^2 \theta_x}{\partial y^2} \right) \right) + \frac{\partial D}{\partial x} \left(\frac{\partial \theta_x}{\partial x} + \nu \frac{\partial \theta_y}{\partial y} \right) \right. \\ \left. + \frac{1-\nu}{2} \frac{\partial D}{\partial y} \left(\frac{\partial \theta_x}{\partial y} + \frac{\partial \theta_y}{\partial x} \right) - Gh \left(\frac{\partial w}{\partial x} - \theta_x \right) - \frac{\rho h^3}{12} \frac{\partial^2 \theta_x}{\partial t^2} \right] d\Omega = 0$$

Performing integration by parts on the first term gives

$$\int_{\Omega} \delta \theta_x D \frac{\partial^2 \theta_x}{\partial x^2} d\Omega = \oint_{\Gamma} \delta \theta_x D \frac{\partial \theta_x}{\partial x} d\Gamma - \int_{\Omega} \frac{\partial \delta \theta_x}{\partial x} D \frac{\partial \theta_x}{\partial x} n_x d\Omega - \int_{\Omega} \delta \theta_x \frac{\partial D}{\partial x} \frac{\partial \theta_x}{\partial x} d\Omega$$

boundary term *symmetric term* *asymmetric term*

Notice that the asymmetric term (i.e. asymmetric in terms of derivatives of θ_x) generated by the integration by parts cancels the first asymmetric term in the θ_x strong equilibrium equation. This cancellation occurs for all the other asymmetric terms in the θ_x

equilibrium equation also, so the final “weak” form of the θ_x equilibrium equation becomes

$$\begin{aligned}
& \oint_{\Gamma} \delta\theta_x D \left(\frac{\partial\theta_x}{\partial x} + \nu \frac{\partial\theta_y}{\partial y} + \frac{1-\nu}{2} \left(\frac{\partial\theta_x}{\partial y} + \frac{\partial\theta_y}{\partial x} \right) \right) d\Gamma \\
& - \int_{\Omega} D \left(\frac{\partial\delta\theta_x}{\partial x} \left(\frac{\partial\theta_x}{\partial x} + \nu \frac{\partial\theta_y}{\partial y} \right) n_x + \frac{\partial\delta\theta_x}{\partial y} \frac{1-\nu}{2} \left(\frac{\partial\theta_x}{\partial y} + \frac{\partial\theta_y}{\partial x} \right) n_y \right) d\Omega \\
& - \int_{\Omega} \delta\theta_x \left(Gh \left(\frac{\partial w}{\partial x} - \theta_x \right) - \frac{\rho h^3}{12} \frac{\partial\delta\theta_x}{\partial t} \frac{\partial\theta_x}{\partial t} \right) d\Omega = 0
\end{aligned}$$

which is the same as the weak θ_x equilibrium equation for a *Reissner-Mindlin plate* with constant material properties. This is also true for the weak form of the θ_y and w equilibrium equations. The final set of weak equilibrium equations for out of plane motion that can be discretized for finite element formulation is:

$$\begin{aligned}
\theta_x : \quad & \oint_{\Gamma} \delta\theta_x D \left(\left(\frac{\partial\theta_x}{\partial x} + \nu \frac{\partial\theta_y}{\partial y} \right) n_x + \frac{1-\nu}{2} \left(\frac{\partial\theta_x}{\partial y} + \frac{\partial\theta_y}{\partial x} \right) n_y \right) d\Gamma \\
& - \int_{\Omega} D \left(\frac{\partial\delta\theta_x}{\partial x} \left(\frac{\partial\theta_x}{\partial x} + \nu \frac{\partial\theta_y}{\partial y} \right) + \frac{\partial\delta\theta_x}{\partial y} \frac{1-\nu}{2} \left(\frac{\partial\theta_x}{\partial y} + \frac{\partial\theta_y}{\partial x} \right) \right) d\Omega \\
& - \int_{\Omega} \delta\theta_x \left(Gh \left(\frac{\partial w}{\partial x} - \theta_x \right) + \frac{\rho h^3}{12} \frac{\partial^2 \theta_x}{\partial t^2} \right) d\Omega = 0
\end{aligned} \tag{2.9a}$$

$$\begin{aligned}
\theta_y : \quad & \oint_{\Gamma} \delta\theta_y D \left(\left(\frac{\partial\theta_y}{\partial y} + \nu \frac{\partial\theta_x}{\partial x} \right) n_x + \frac{1-\nu}{2} \left(\frac{\partial\theta_x}{\partial y} + \frac{\partial\theta_y}{\partial x} \right) n_y \right) d\Gamma \\
& - \int_{\Omega} D \left(\frac{\partial\delta\theta_y}{\partial y} \left(\frac{\partial\theta_y}{\partial y} + \nu \frac{\partial\theta_x}{\partial x} \right) + \frac{\partial\delta\theta_y}{\partial x} \frac{1-\nu}{2} \left(\frac{\partial\theta_x}{\partial y} + \frac{\partial\theta_y}{\partial x} \right) \right) d\Omega \\
& - \int_{\Omega} \delta\theta_y \left(Gh \left(\frac{\partial w}{\partial y} - \theta_y \right) + \frac{\rho h^3}{12} \frac{\partial^2 \theta_y}{\partial t^2} \right) d\Omega = 0
\end{aligned} \tag{2.9b}$$

$$\begin{aligned}
w : \quad & \oint_{\Gamma} \delta w_y Gh \left(\left(\frac{\partial w}{\partial x} - \theta_x \right) n_x + \left(\frac{\partial w}{\partial y} - \theta_y \right) n_y \right) d\Gamma \\
& - \int_{\Omega} Gh \left(\frac{\partial\delta w}{\partial x} \left(\frac{\partial w}{\partial x} - \theta_x \right) + \frac{\partial\delta w}{\partial y} \left(\frac{\partial w}{\partial y} - \theta_y \right) \right) d\Omega \\
& - \int_{\Omega} \delta w \rho h \frac{\partial^2 w}{\partial t^2} d\Omega = 0
\end{aligned} \tag{2.9c}$$

Now consider the energy terms associated with in-plane motion which model shear deformation in the *Reissner-Mindlin plate*. Hamilton's Principle for these terms may be written as

$$\begin{aligned}
H_{LS} &= \int_{t_1}^{t_2} (T_{LS} - U_{LS} + W_{LS}) dt \\
\delta H_S &= \int_{t_1}^{t_2} (\delta T_{LS} - \delta U_{LS} + \delta W_{LS}) dt = 0 \quad \delta W_S = \delta(-q_u u - q_v v) \\
\int_{t_1}^{t_2} \frac{1}{2} \int_{\Omega} \delta & \left\{ \begin{aligned} & \left[\rho h \left(\frac{\partial u}{\partial t} \right)^2 + \rho h \left(\frac{\partial v}{\partial t} \right)^2 \right] - \tilde{E} h \left[\left(\frac{\partial u}{\partial x} \right)^2 + 2\nu \frac{\partial u}{\partial x} \frac{\partial v}{\partial y} + \left(\frac{\partial v}{\partial y} \right)^2 \right] \\ & - \left[Gh \left(\frac{\partial u}{\partial y} + \frac{\partial v}{\partial x} \right)^2 \right] - q_u u - q_v v \end{aligned} \right\} d\Omega dt = 0
\end{aligned} \tag{2.10}$$

After taking the variation and using integration by parts as before, we generate the following equilibrium equations for u and v :

$$\delta u : \quad h \left[\begin{aligned} & \tilde{E} \left(\frac{\partial^2 u}{\partial x^2} + \nu \frac{\partial^2 v}{\partial x \partial y} \right) + G \left(\frac{\partial^2 v}{\partial x \partial y} + \frac{\partial^2 u}{\partial y^2} \right) + \frac{\partial \tilde{E}}{\partial x} \left(\frac{\partial u}{\partial x} + \nu \frac{\partial v}{\partial y} \right) \\ & + \frac{\partial G}{\partial y} \left(\frac{\partial u}{\partial y} + \frac{\partial v}{\partial x} \right) - \rho h \frac{\partial^2 u}{\partial t^2} \end{aligned} \right] = 0 \quad (2.11a)$$

$$\delta v : \quad h \left[\begin{aligned} & \tilde{E} \left(\frac{\partial^2 v}{\partial y^2} + \nu \frac{\partial^2 u}{\partial x \partial y} \right) + G \left(\frac{\partial^2 u}{\partial x \partial y} + \frac{\partial^2 v}{\partial x^2} \right) + \frac{\partial \tilde{E}}{\partial y} \left(\frac{\partial v}{\partial y} + \nu \frac{\partial u}{\partial x} \right) \\ & + \frac{\partial G}{\partial x} \left(\frac{\partial u}{\partial y} + \frac{\partial v}{\partial x} \right) - \rho h \frac{\partial^2 v}{\partial t^2} \end{aligned} \right] = 0 \quad (2.11b)$$

with boundary conditions (one from each group):

$$\{u = 0 \quad v = 0\}$$

$$\left\{ F_{xx} = \tilde{E}h \left(\frac{\partial u}{\partial x} + \nu \frac{\partial v}{\partial y} \right) \quad F_{yy} = \tilde{E}h \left(\frac{\partial v}{\partial y} + \nu \frac{\partial u}{\partial x} \right) \quad V_{xy} = Gh \left(\frac{\partial u}{\partial y} + \frac{\partial v}{\partial x} \right) \right\}$$

Again, these equations can be put into a form useful to finite element development by multiplying them by an arbitrary displacement function, integrating over the surface, and then performing integration by parts as necessary. For the in plane displacements u and v , the asymmetric terms cancel out as they did for the weak forms of the θ_x and θ_y equilibrium equations. Thus, the following weak forms of the equilibrium (virtual work) equations for u and v result.

u :

$$\begin{aligned}
 & -\int_{\Omega} \left(\tilde{E}h \frac{\partial \delta u}{\partial x} \left(\frac{\partial u}{\partial x} + \nu \frac{\partial v}{\partial y} \right) + Gh \frac{\partial \delta u}{\partial y} \left(\frac{\partial u}{\partial y} + \frac{\partial v}{\partial x} \right) + \rho h \delta u \frac{\partial^2 u}{\partial t^2} \right) d\Omega \\
 & + \oint_{\Gamma} \delta u \left[\tilde{E}h \left(\frac{\partial u}{\partial x} + \nu \frac{\partial v}{\partial y} \right) n_x + Gh \left(\frac{\partial u}{\partial y} + \frac{\partial v}{\partial x} \right) n_y \right] d\Gamma = 0
 \end{aligned} \tag{2.12a}$$

v :

$$\begin{aligned}
 & -\int_{\Omega} \left(\tilde{E}h \frac{\partial \delta v}{\partial y} \left(\frac{\partial v}{\partial y} + \nu \frac{\partial u}{\partial x} \right) + Gh \frac{\partial \delta v}{\partial x} \left(\frac{\partial u}{\partial y} + \frac{\partial v}{\partial x} \right) + \rho h \delta v \frac{\partial^2 v}{\partial t^2} \right) d\Omega \\
 & + \oint_{\Gamma} \delta v \left[\tilde{E}h \left(\frac{\partial v}{\partial y} + \nu \frac{\partial u}{\partial x} \right) n_y + Gh \left(\frac{\partial u}{\partial y} + \frac{\partial v}{\partial x} \right) n_x \right] d\Gamma = 0
 \end{aligned} \tag{2.12b}$$

2.3 Kirchoff (Thin) Plate Theory Assuming $E=E(x,y)$

When we make the further assumption that a transverse cross section that is normal to the undeformed mid plane of the plate configuration remains normal to the mid plane surface after the plate is deformed, then $\theta = dw/dx$ for small deformations and the following expressions describe classic (Kirchoff) plate theory. Taking the mid-plane of the plate to be $z=0$ for a plate with a coordinate system as shown in Figure 2.1, we can write the following expressions for the displacement, strain and stress in Kirchoff theory.

Displacements:

$$\begin{aligned}
 \tilde{u} & \approx u(x, y) - z\theta_x(x, y) & \tilde{v} & \approx v(x, y) - z\theta_y(x, y) & \tilde{w} & \approx w(x, y) \\
 \tilde{u} & \approx u(x, y) - z \frac{dw(x, y)}{dx} & \tilde{v} & \approx v(x, y) - z \frac{dw(x, y)}{dy} & \tilde{w} & \approx w(x, y)
 \end{aligned} \tag{2.13}$$

Strains:

$$\begin{aligned}\varepsilon_{xx} &= \frac{\partial \tilde{u}}{\partial x} = -z \frac{\partial^2 w}{\partial x^2} & \varepsilon_{yy} &= \frac{\partial \tilde{v}}{\partial y} = -z \frac{\partial^2 w}{\partial x^2} \\ \gamma_{xy} &= \frac{\partial \tilde{u}}{\partial y} + \frac{\partial \tilde{v}}{\partial x} = -2z \left(\frac{\partial^2 w}{\partial x \partial y} \right) & \varepsilon_{xz} &= \gamma_{xz} = \gamma_{zx} = 0\end{aligned}\quad (2.14)$$

Stresses:

$$\begin{aligned}\sigma_{xx} &= \frac{E}{1-\nu^2} (\varepsilon_{xx} + \nu \varepsilon_{yy}) = -\frac{E}{1-\nu^2} z \left(\frac{\partial^2 w}{\partial x^2} + \nu \frac{\partial^2 w}{\partial y^2} \right) \\ \sigma_{yy} &= \frac{E}{1-\nu^2} (\varepsilon_{yy} + \nu \varepsilon_{xx}) = -\frac{E}{1-\nu^2} z \left(\frac{\partial^2 w}{\partial y^2} + \nu \frac{\partial^2 w}{\partial x^2} \right) \\ \sigma_{xy} &= G \gamma_{xy} = -2Gz \left(\frac{\partial^2 w}{\partial x \partial y} \right) & \sigma_{zz} &= \sigma_{xz} = \sigma_{yz} = 0\end{aligned}\quad (2.15)$$

In these expressions \tilde{u} , \tilde{v} , and \tilde{w} are the x , y and z displacements and w is the independent function of x and y .

To generate equations of motion in Kirchoff plate theory with spatially variable material properties we will develop expressions for kinetic energy, strain energy and work. We will not write out the terms involving extensional displacement here as these are the same as in the *Reissner-Mindlin* formulation. Then, using Hamilton's Principle, we will generate equilibrium equations.

Strain energy:

$$U = \frac{1}{2} \int_{\Omega} (\sigma_{xx} \varepsilon_{xx} + \sigma_{yy} \varepsilon_{yy} + \sigma_{xy} \varepsilon_{xy}) d\Omega$$

When expressions for stress and strain are substituted into the expression for U , and z is integrated over the thickness of the plate, the result is

$$U = U(w)$$

$$U = \frac{1}{2} \int_{\Omega} \left\{ D \left(\left(\frac{\partial^2 w}{\partial x^2} \right)^2 + 2\nu \frac{\partial^2 w}{\partial x^2} \frac{\partial^2 w}{\partial y^2} + \left(\frac{\partial^2 w}{\partial y^2} \right)^2 \right) + G 2(1-\nu) \left(\frac{\partial^2 w}{\partial x \partial y} \right)^2 \right\} d\Omega \quad (2.16)$$

where

$$D = \frac{E h^3}{12(1-\nu^2)} \quad G = \frac{E}{2(1+\nu)}$$

and h is the thickness of the plate.

Kinetic energy:

$$T = \frac{1}{2} \int_{\Omega} (\dot{u}^2 + \dot{v}^2 + \dot{w}^2) d\Omega \quad T = T(w)$$

$$T = \frac{1}{2} \int_{\Omega} \left(\rho h (\dot{w})^2 + \frac{\rho h^3}{12} \left(\left(\frac{\partial \dot{w}}{\partial x} \right)^2 + \left(\frac{\partial \dot{w}}{\partial y} \right)^2 \right) \right) d\Omega \quad (2.17)$$

We will look at energy terms associated with out of plane motion. Hamilton's Principle for these terms may be written

$$H = \int_{t_1}^{t_2} (T - U + W) dt$$

$$\delta H = \int_{t_1}^{t_2} (\delta T - \delta U + \delta W) dt = 0 \quad \delta W = \delta(-qw)$$

$$\int_{t_1}^{t_2} \frac{1}{2} \int_{\Omega} \delta \left\{ \begin{aligned} & \rho h (\dot{w})^2 + \frac{\rho h^3}{12} \left(\left(\frac{\partial \dot{w}}{\partial x} \right)^2 + \left(\frac{\partial \dot{w}}{\partial y} \right)^2 \right) \\ & - D \left(\left(\frac{\partial^2 w}{\partial x^2} \right)^2 + 2\nu \frac{\partial^2 w}{\partial x^2} \frac{\partial^2 w}{\partial y^2} + \left(\frac{\partial^2 w}{\partial y^2} \right)^2 \right) \\ & + \frac{1-\nu}{2} \left(\frac{\partial \theta_y}{\partial x} + \frac{\partial \theta_x}{\partial y} \right)^2 \\ & + G 2(1-\nu) \left(\frac{\partial^2 w}{\partial x \partial y} \right)^2 - qw \end{aligned} \right\} d\Omega dt = 0 \quad (2.18)$$

where δW is the contribution of the energy in the system due to surface and body forces represented by q . Carrying out the variation of T and U according to the rule $\delta H = \frac{\partial H}{\partial \alpha} \delta \alpha$ and performing integration by parts as necessary allows us to generate

equilibrium equations. As before, since the moduli are functions of spatial variables, integration by parts generates terms with derivatives of the independent functions. Below is the variation and integration by parts for one term in U for the Kirchoff formulation:

$$\begin{aligned} \delta \left(\int_{t_1}^{t_2} \int_{\Omega} D \left(\frac{\partial^2 w}{\partial x^2} \right)^2 d\Omega dt \right) &= \int_{t_1}^{t_2} \int_{\Omega} 2D \frac{\partial^2 w}{\partial x^2} \frac{\partial^2 \delta w}{\partial x^2} d\Omega dt \\ &= \int_{t_1}^{t_2} \left\{ \begin{aligned} & \oint_{\Gamma} 2 \left[\left(D \frac{\partial^3 w}{\partial x^3} + \frac{\partial D}{\partial x} \frac{\partial^2 w}{\partial x^2} \right) \delta w - D \frac{\partial \delta w}{\partial x} \frac{\partial^2 w}{\partial x^2} \right] n_x d\Gamma \\ & - \int_{\Omega} 2D \frac{\partial^4 w}{\partial x^4} \delta w d\Omega - \int_{\Omega} 2 \left(\frac{\partial D^3}{\partial x^3} \frac{\partial w}{\partial x} + \frac{\partial^2 D}{\partial x^2} \frac{\partial^2 w}{\partial x^2} \right) \delta w d\Omega \end{aligned} \right\} dt \end{aligned}$$

Carrying through the variation and integration by parts for all terms in T and U yields the following equilibrium equation for the bending motion of a plate with spatially variable material properties:

$$\begin{aligned}
\delta w : \quad & D \left\{ \frac{\partial^4 w}{\partial x^4} + \frac{\partial^4 w}{\partial y^4} + 2\nu \frac{\partial^4 w}{\partial x^2 \partial y^2} + 2(1-\nu) \frac{\partial^4 w}{\partial x^2 \partial y^2} \right\} \\
& + \frac{\partial E}{\partial x} \left(\frac{\partial^3 w}{\partial x^3} + 2\nu \frac{\partial^3 w}{\partial x \partial y^2} + 2(1-\nu) \frac{\partial^3 w}{\partial x \partial y^2} \right) \\
& + \frac{\partial E}{\partial y} \left(\frac{\partial^3 w}{\partial y^3} + 2\nu \frac{\partial^3 w}{\partial x^2 \partial y} + 2(1-\nu) \frac{\partial^3 w}{\partial x^2 \partial y} \right) \\
& + \frac{\partial^2 E}{\partial x^2} \left(\frac{\partial^2 w}{\partial x^2} + \nu \frac{\partial^2 w}{\partial y^2} \right) + \frac{\partial^2 E}{\partial y^2} \left(\frac{\partial^2 w}{\partial y^2} + \nu \frac{\partial^2 w}{\partial x^2} \right) \\
& + 2(1-\nu) \frac{\partial^2 E}{\partial x \partial y} \frac{\partial^2 w}{\partial x \partial y} + \frac{\rho h^3}{12} \left(\frac{\partial^2 \dot{w}}{\partial x^2} + \frac{\partial^2 \dot{w}}{\partial y^2} \right) - \rho h \dot{w} = 0
\end{aligned} \tag{2.19}$$

with boundary conditions

$$\left\{ \delta w = 0 \quad \frac{\partial \delta w}{\partial x} = 0 \quad \frac{\partial \delta w}{\partial y} = 0 \right\}$$

$$\left[\begin{aligned}
V &= D \left[\frac{\partial^3 w}{\partial x^3} + \frac{\partial^3 w}{\partial y^3} + \nu \frac{\partial^3 w}{\partial x \partial y^2} + \nu \frac{\partial^3 w}{\partial x^2 \partial y} + 2(1-\nu) \frac{\partial^3 w}{\partial x \partial y^2} \right] + \frac{\partial D}{\partial x} \left(\frac{\partial^2 w}{\partial x^2} + \nu \frac{\partial^2 w}{\partial y^2} \right) \\
& \quad + \frac{\partial D}{\partial y} \left(\frac{\partial^2 w}{\partial y^2} + \nu \frac{\partial^2 w}{\partial x^2} + 2(1-\nu) \frac{\partial^2 w}{\partial x \partial y} \right) \\
M_{xx} &= D \left(\frac{\partial^2 w}{\partial x^2} + \nu \frac{\partial^2 w}{\partial y^2} + 2(1-\nu) \frac{\partial^2 w}{\partial x \partial y} \right) \\
M_{yy} &= D \left(\frac{\partial^2 w}{\partial y^2} + \nu \frac{\partial^2 w}{\partial x^2} \right)
\end{aligned} \right]$$

We can go back to the symmetric formulation that is useful for generating stiffness and mass matrices by applying the principle of virtual work to the equations. The equilibrium

equation is multiplied by a virtual displacement and then is integrated over the surface Ω . Integration by parts is performed and the variables in the resulting equation are discretized to generate the matrices used in finite element formulations. Virtual work for the w equilibrium equation is:

$$\int_{\Omega} \delta w \left[\begin{aligned} & D \left\{ \frac{\partial^4 w}{\partial x^4} + \frac{\partial^4 w}{\partial y^4} + 2\nu \frac{\partial^4 w}{\partial x^2 \partial y^2} + 2(1-\nu) \frac{\partial^4 w}{\partial x^2 \partial y^2} \right\} \\ & + \frac{\partial E}{\partial x} \left(\frac{\partial^3 w}{\partial x^3} + 2\nu \frac{\partial^3 w}{\partial x \partial y^2} + 2(1-\nu) \frac{\partial^3 w}{\partial x \partial y^2} \right) \\ & + \frac{\partial E}{\partial y} \left(\frac{\partial^3 w}{\partial y^3} + 2\nu \frac{\partial^3 w}{\partial x^2 \partial y} + 2(1-\nu) \frac{\partial^3 w}{\partial x^2 \partial y} \right) \\ & + \frac{\partial^2 E}{\partial x^2} \left(\frac{\partial^2 w}{\partial x^2} + \nu \frac{\partial^2 w}{\partial y^2} \right) + \frac{\partial^2 E}{\partial y^2} \left(\frac{\partial^2 w}{\partial y^2} + \nu \frac{\partial^2 w}{\partial x^2} \right) \\ & + 2(1-\nu) \frac{\partial^2 E}{\partial x \partial y} \frac{\partial^2 w}{\partial x \partial y} + \frac{\rho h^3}{12} \left(\frac{\partial^2 \dot{w}}{\partial x^2} + \frac{\partial^2 \dot{w}}{\partial y^2} \right) - \rho h \dot{w} \end{aligned} \right] d\Omega = 0$$

After appropriate integration by parts, the weak form of the equilibrium equation takes the form:

$$\int_{\Omega} \left[\begin{aligned} & \frac{\partial^2 \delta w}{\partial x^2} D \frac{\partial^2 w}{\partial x^2} + \frac{\partial^2 \delta w}{\partial y^2} D \frac{\partial^2 w}{\partial y^2} + D \nu \left(\frac{\partial^2 \delta w}{\partial x^2} \frac{\partial^2 w}{\partial y^2} + \frac{\partial^2 \delta w}{\partial y^2} \frac{\partial^2 w}{\partial x^2} \right) + 2(1-\nu) \frac{\partial^2 \delta w}{\partial x \partial y} \frac{\partial^2 w}{\partial x \partial y} \\ & - \frac{\rho h^3}{12} \left(\frac{\partial \delta w}{\partial x} \frac{\partial \dot{w}}{\partial x} + \frac{\partial \delta w}{\partial y} \frac{\partial \dot{w}}{\partial y} \right) - \rho h \dot{w} \delta w \end{aligned} \right] d\Omega$$

$$+ \oint_{\Gamma} \left\{ \begin{aligned} & \delta w \left[\begin{aligned} & D \left[\left(\frac{\partial^3 w}{\partial x^3} + \nu \frac{\partial^3 w}{\partial x \partial y^2} \right) n_x + \left(\frac{\partial^3 w}{\partial y^3} + \nu \frac{\partial^3 w}{\partial x^2 \partial y} + 2(1-\nu) \frac{\partial^3 w}{\partial x \partial y^2} \right) n_y \right] \\ & + \frac{\partial D}{\partial x} \left[\left(\frac{\partial^2 w}{\partial x^2} + \nu \frac{\partial^2 w}{\partial y^2} \right) n_x + \left(2(1-\nu) \frac{\partial^2 w}{\partial x \partial y} \right) n_y \right] + \frac{\partial D}{\partial y} \left[\left(\frac{\partial^2 w}{\partial y^2} + \nu \frac{\partial^2 w}{\partial x^2} \right) n_y \right] \end{aligned} \right] \\ & - \frac{\partial \delta w}{\partial x} D \left[\left(\frac{\partial^2 w}{\partial x^2} + \nu \frac{\partial^2 w}{\partial y^2} \right) n_x - \frac{\partial \delta w}{\partial y} \left[\left(\frac{\partial^2 w}{\partial y^2} + \nu \frac{\partial^2 w}{\partial x^2} \right) n_x + \left(2(1-\nu) \frac{\partial^2 w}{\partial x \partial y} \right) n_y \right] \end{aligned} \right\} d\Gamma = 0$$

2.4 Summary

In this chapter, we have developed strong (Eqs. 2.8 and 2.11) and weak forms (Eqs. 2.9 and 2.12) of the equilibrium equations for plates that have material properties varying in-plane using both the *Reissner-Mindlin* assumptions and *Kirchoff* assumptions. The following observations and comments may be made regarding the results. The weak form of the equilibrium equations is the same for a plate with material properties that vary in-plane as a plate with constant variable properties. Derivatives of the material properties arise in the variation of the strain energy expression only after integration by parts. This is a result of mathematical manipulation rather than of modeling some physical phenomenon. Thus, the differences in the stiffness matrices of homogeneous plates and spatially varying plates will occur only because the bending stiffness D is now function of x and y , i.e. $D(x,y)$, and therefore must be included inside the integration of the energy functional.

In this investigation, the transverse shear is an important mechanism through which kinetic energy is transformed to heat and dissipated. Since the *Kirchoff* plate formulation does not explicitly model the effect of transverse shear and the *Reissner-Mindlin* formulation does, the *Reissner-Mindlin* plate theory will be used in developing a finite element model that can model a spatially varying viscoelastic layer.

Chapter 3

Preliminary Experimental Work

To test the hypothesis that a viscoelastic layer with non-homogeneous material properties in-plane would more effectively reduce pressures within a cavity than its homogeneous counterpart, a preliminary experiment was performed. This experiment was principally undertaken for the purposes of looking at the validity of the concept.

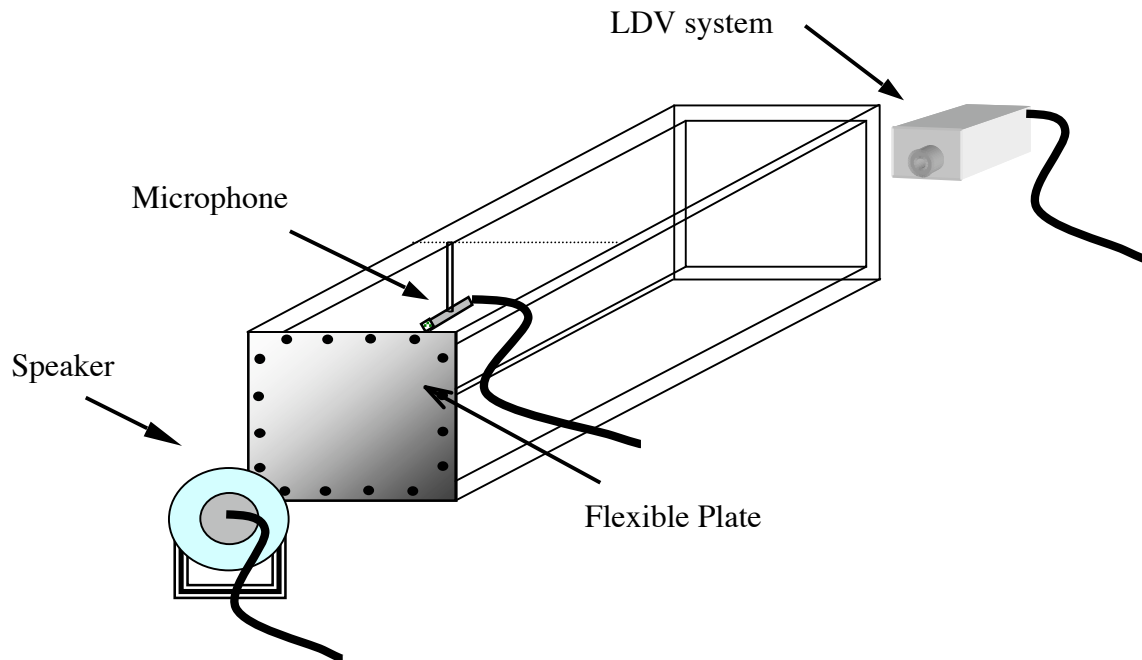


Figure 3. 1: Sketch of experimental setup for preliminary experiment

3.1 Experimental Setup

Figure 3.1 shows a sketch of the experimental setup and Figure 3.2 a connections diagram.

The experiment was conducted in an acoustic cavity that had 5 walls made of 0.5 inch Plexiglas. The interior dimensions of the box were 12" x 12" x 30." The sixth wall of the enclosure was formed of an aluminum plate that was 0.016" thick. This flexible plate was bolted onto the Plexiglas enclosure with 16 bolts.

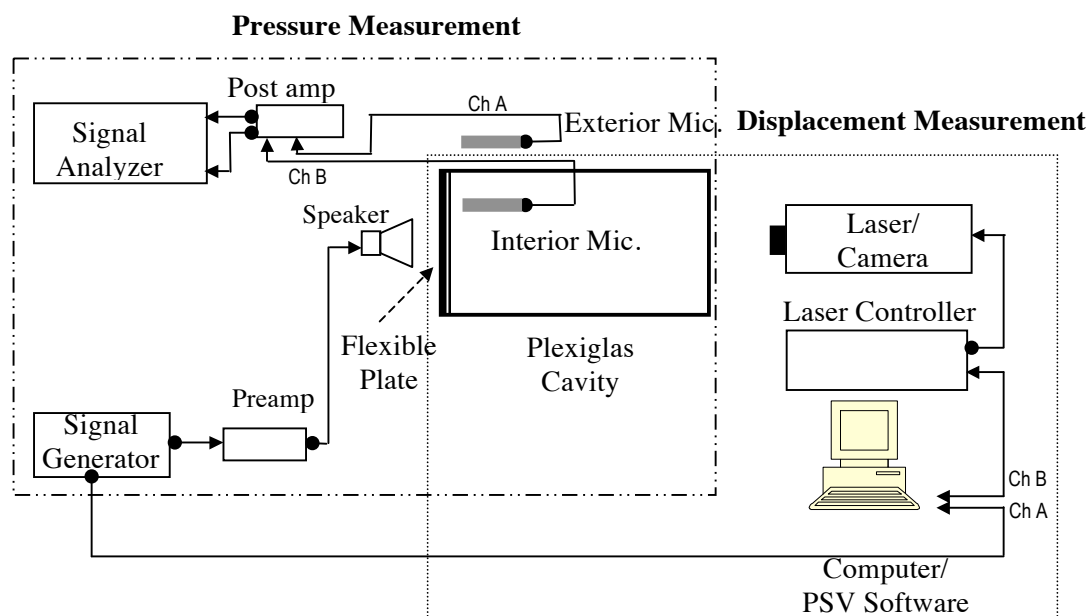


Figure 3. 2: Connections diagram for preliminary experiment

The plate was excited with an external speaker (Techni Coustic Model 616RS; 6.5" woofer, 35 W rms) placed 1 3/8 inches away from the flexible plate. The speaker was driven with low pass filtered white noise (0-200 Hz, 1V p-p) for pressure measurements.

The interior pressure field was monitored at a single point using a Larson-Davis microphone (PRM902). A threaded rod suspended the microphone 6 inches down from the top of the Plexiglas cavity, 5 inches behind the flexible plate, and 3 inches from the side wall. A second microphone was positioned outside the cavity to measure the

ambient noise. The outputs of the inside and outside microphones were monitored using an Ono Sokki CF350 signal analyzer. Spectra were generated using 128 averages and a frequency resolution bandwidth of 0.5 Hz.

A sketch of the four viscoelastic layer configurations is shown in Figure 3.3

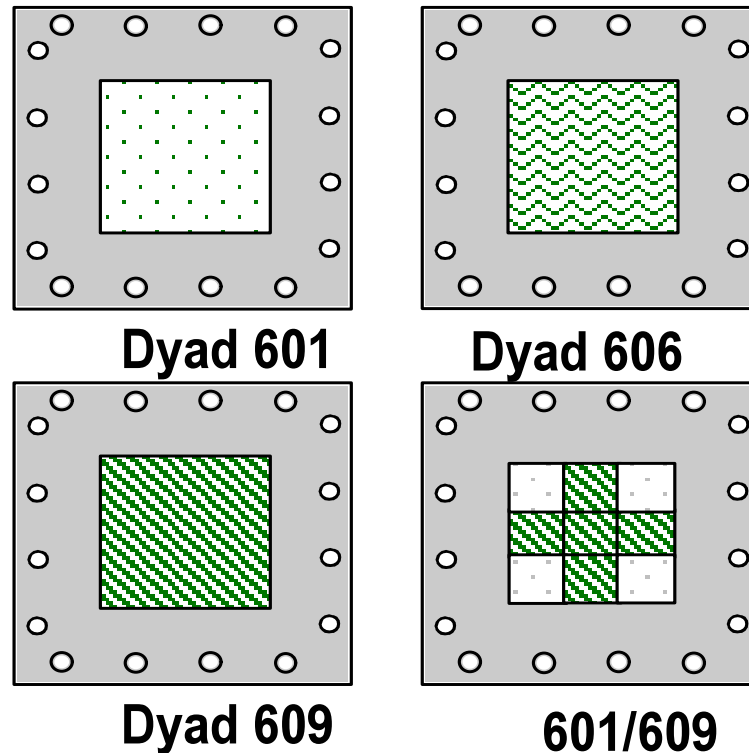
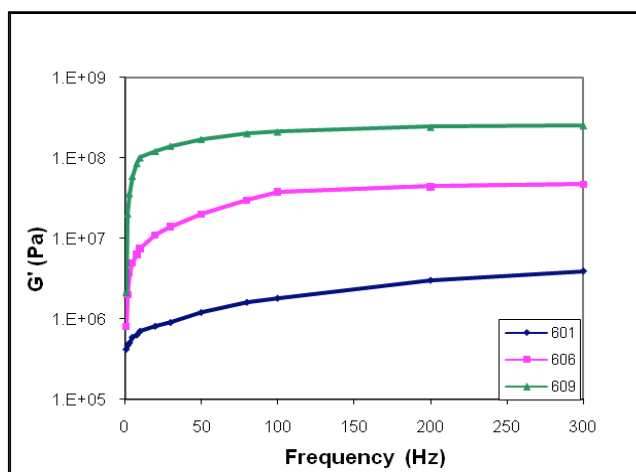
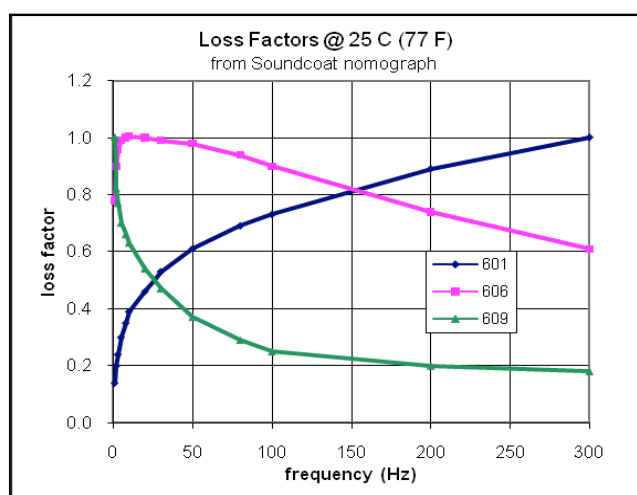


Figure 3.3: Sketch of the four viscoelastic layer configurations White circles indicate approximate bolt locations

The regular viscoelastic layers were fabricated from 6" x 6" x 0.05" squares of the Soundcoat Company's Dyad damping material. Layers of Dyad 601, Dyad 606 and Dyad 609 were bonded to aluminum plates with epoxy. At 77 degrees F , the three materials have the loss factor η and shear modulus G presented in Figure 3.4. These curves of the shear modulus and loss factor were derived from the Soundcoat nomographs .



(a)



(b)

Figure 3.4: Shear modulus G' (a) and loss factor η (b) for viscoelastic materials

The spatially varying layer was fabricated using patches of the 601 and 609 materials as shown in Figure 3.3. Dyad 601 and Dyad 609 were chosen for the spatially varying configuration in this initial experiment as they had the most dissimilar loss factors and shear moduli.

For the constrained layer configurations of the four viscoelastic layers, a sheet of 0.005 in aluminum was bonded on top of the viscoelastic layer

Measurements were also made of the plate's displacement at resonant frequencies using a PSV200 laser vibrometer system. During the vibrometer measurements, the flexible plate was excited with a tone at a resonance frequency of the plate. The signal fed to speaker was used as an outside reference signal to vibrometer software to determine phase information in the measurement. PSV's Fast Scan option was used to generate the plate's mode shapes, and the measurement was made using 25x25 point grid with a 5 Hz bandwidth around the center frequency (the excitation frequency).

3.2 Configurations for preliminary experiment

Measurements were made for the following configurations:

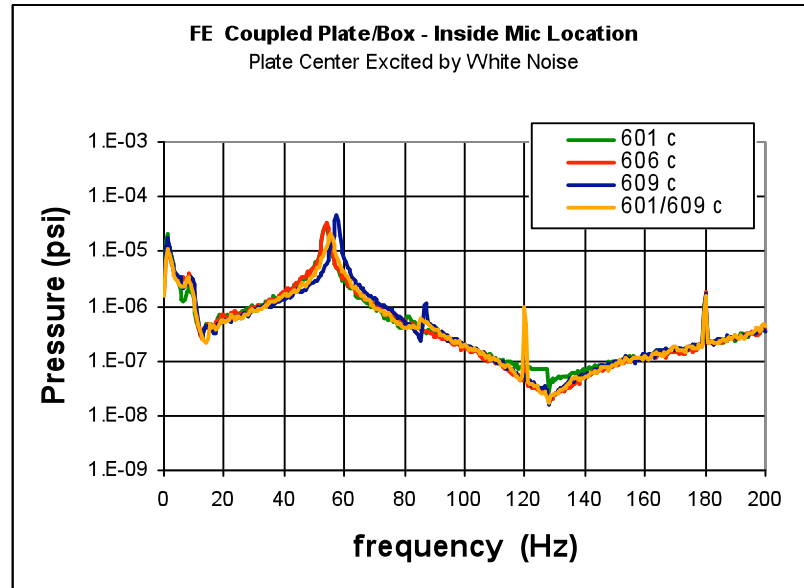
1. Plain Plate: An aluminum plate with no viscoelastic layer was bolted on the Plexiglas box. One run made for each plate used for before the viscoelastic layer was attached.
2. 601 uc: Aluminum plate with a layer of Dyad 601 was bolted on the Plexiglas box.
3. 606 uc: Aluminum plate with a layer of Dyad 606 was bolted on the Plexiglas box.
4. 609 uc: Aluminum plate with a layer of Dyad 609 was bolted on the Plexiglas box.

5. 601/609 uc: Aluminum plate with an spatially varying layer made of Dyad 601 and Dyad 609 was bolted on the Plexiglas box. Two runs made with two different plates.
6. 601c: An aluminum plate with a constrained layer of Dyad 601 was bolted on the Plexiglas box.
7. 606c: An aluminum plate with a constrained layer of Dyad 606 was bolted on the Plexiglas box.
8. 6091c: An aluminum plate with a constrained layer of Dyad 609 was bolted on the Plexiglas box.
9. 601/609c: Aluminum plate with a constrained spatially varying layer made of Dyad 601 and Dyad 609 was bolted on the Plexiglas box. Two runs made.

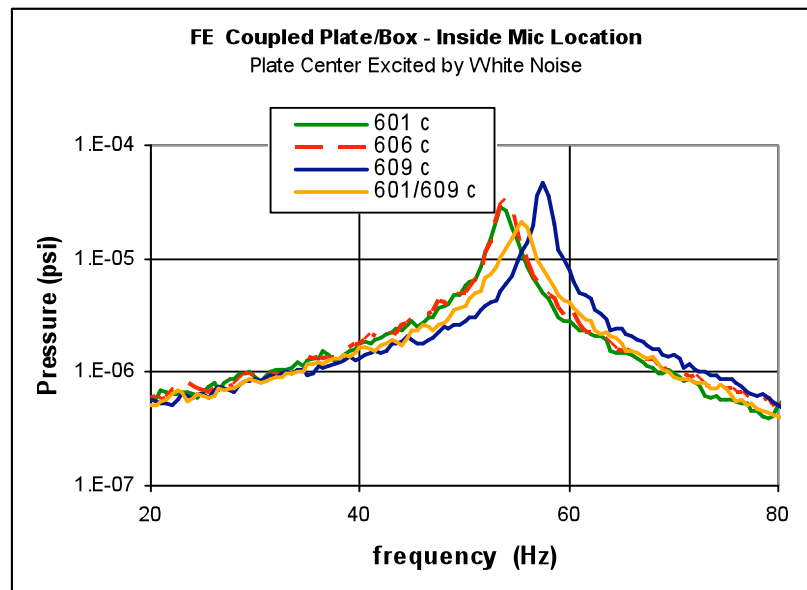
3.3 Results

The configurations of interest to this investigation from the preliminary experiment were the constrained layer runs and the untreated plate runs. The data pertaining to these runs will be discussed in this section.

Figure 3.5 presents the pressure levels inside the enclosure for the four plates with a constrained viscoelastic layer. On the left hand side are the pressure levels for the entire frequency range of interest to this investigation (0-200Hz), and on the right hand side the same data is but is focused on the frequency range close to the first resonance peak (20-80 Hz).



(a) – Full range



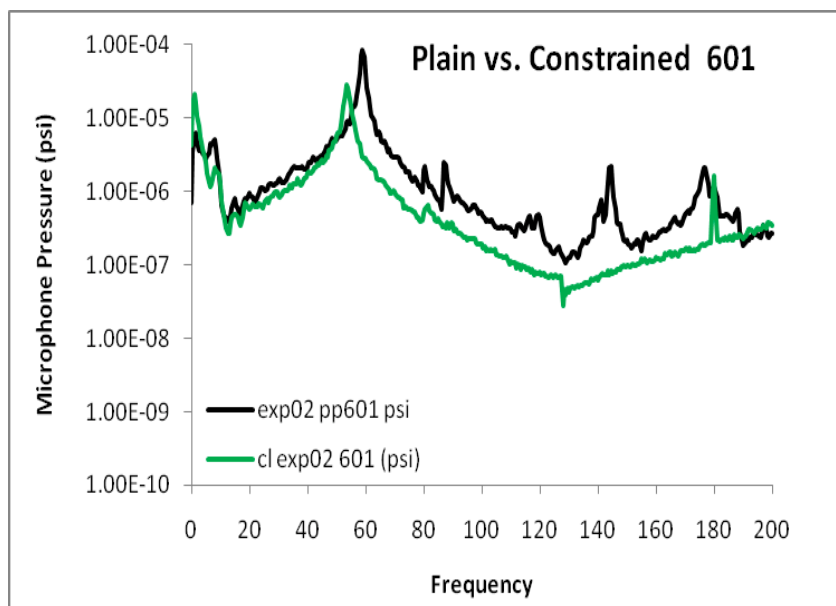
(b) –zoom on range between 20-80 Hz

Figure 3.5: Comparison of pressure levels for the four constrained viscoelastic layers.

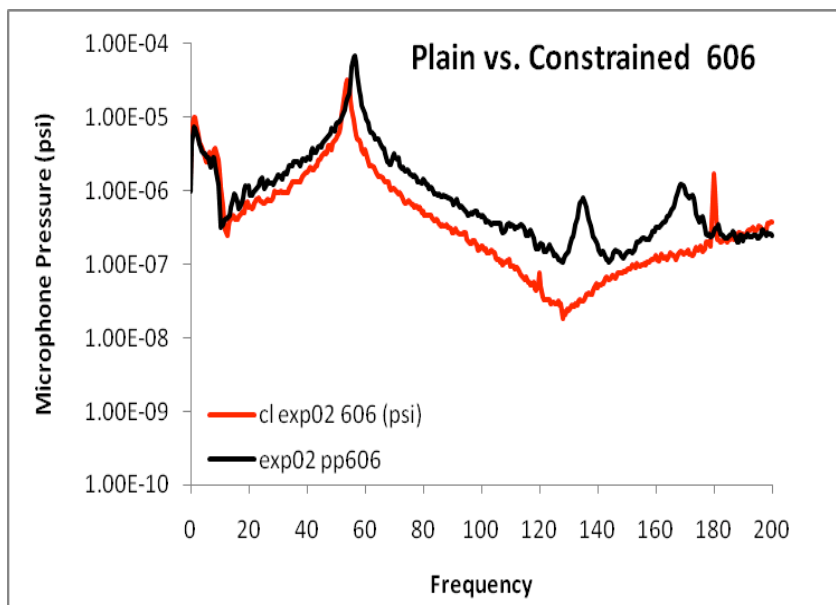
It can be seen that when the plate with the constrained spatially varying viscoelastic layer is excited by white noise from the speaker, the levels in the enclosure are lower than the levels that occur inside the enclosure when any of the other three treated plates, which have homogeneous constrained layers, are insonified. At the first resonance the pressure levels for the plate with a spatially varying layer are 36% lower than the level for the plate with a Dyad 601 layer, are 44% lower than the levels for the Dyad 606 plate and 60% less than the levels for the plate with a Dyad 609 layer. Note that 60 cycle harmonics at 120 Hz and 180 Hz appear in some of the runs.

In Figure 3.6, the pressure levels in the enclosure when white noise is broadcast towards a plate with a constrained viscoelastic layer is compared to the pressure levels that occur within the enclosure when the plate is untreated i.e. has no constrained viscoelastic layer

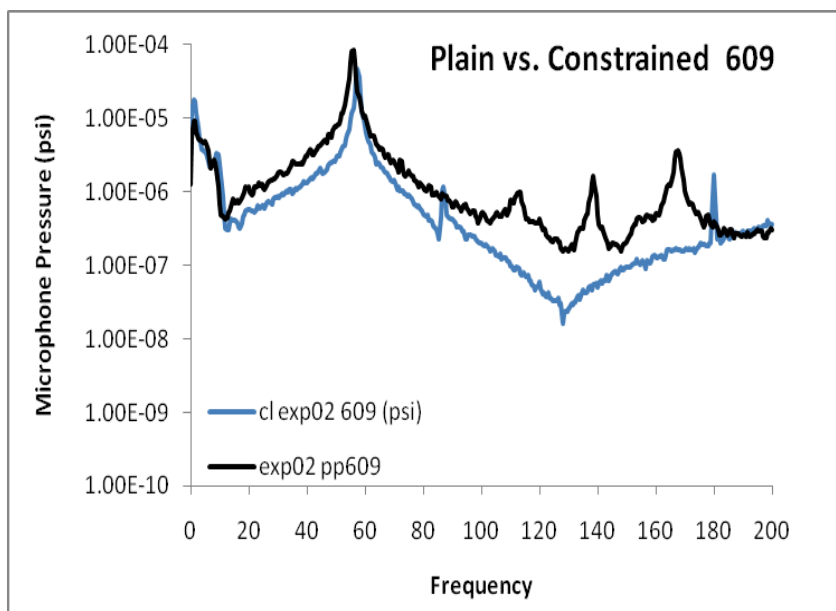
In Figure 3.6, the pressure levels in the enclosure when white noise is broadcast towards a plate with a constrained viscoelastic layer is compared to the pressure levels that occur within the enclosure when the plate is untreated, i.e. has no constrained viscoelastic layer.



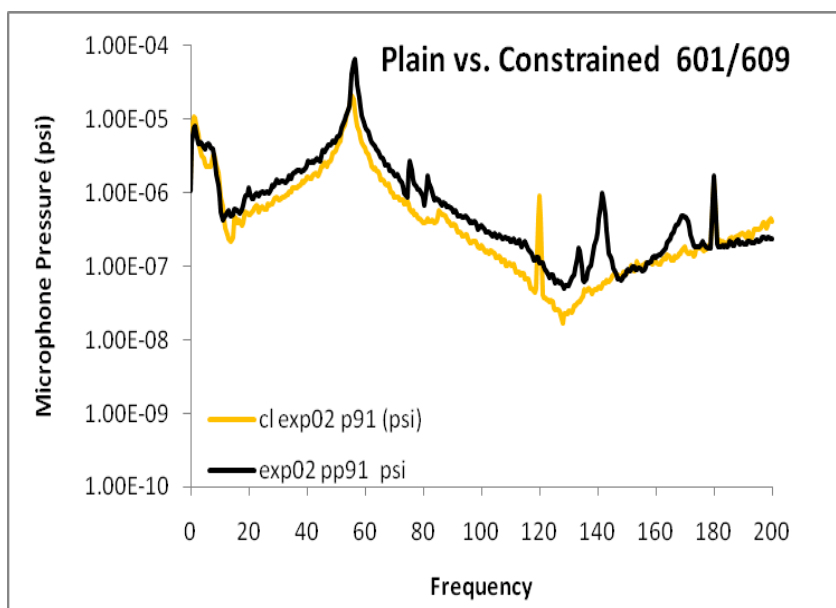
(a)



(b)



(c)



(d)

Figure 3. 6: Comparison of constrained layer pressure levels with those of the untreated plate.

In each of these plots, the black line represents the data for the inside pressure levels with an untreated plate, and the colored line depicts the pressure levels for the same plate treated with a viscoelastic layer. The plot for the spatially varying plate has data

averaged over the two runs performed for this configuration. It can be seen that all the viscoelastic layers produce pressure level reductions that are broadband in frequency, but the spatially varying layer produces the greatest reduction in the lowest resonance peak for the plate/cavity system. The spatially varying constrained layer resulted in a 10 dB decrease from the plain plate configuration.

Above a frequency of about 20 Hz there is a broadband decrease in the measured pressure levels of about 6 – 10 dB (except at resonances) for all the viscoelastic layers applied to the plates. Also, it appears that all four viscoelastic layers change the system impedance from that of the plain plate (see Figure 3.6) so that the quality factor increases and the higher modes of the plate are no longer apparent.

For completeness Figure 3.7 presents data from measurements of the ambient pressure levels inside and outside of the enclosure. Also included in this plot are pressure data from the inside and outside microphone spectra for a typical white noise run. The following observations may be made with respect to the data: 1) There are 60 cycle harmonics present in many of the spectra at 120 Hz and 180 Hz. This occasionally is strong enough to be present in data runs. 2) From 0 to about 12 Hz there is a strong band of energy present in all the spectra.

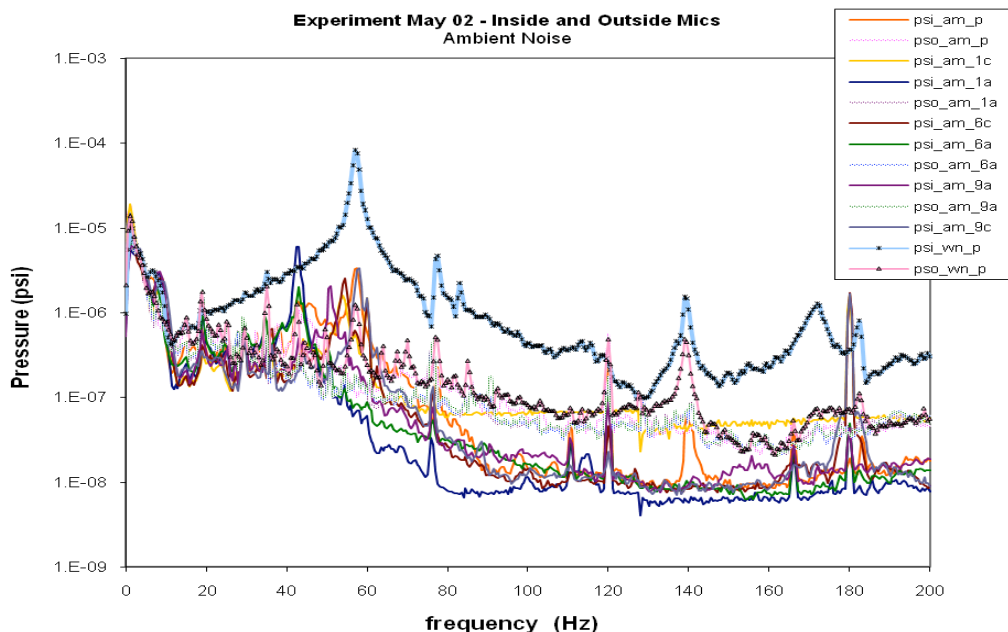


Figure 3.7 Ambient data for inside and outside microphones. Curves with black symbols are data from a typical white noise run. Star- inside microphone Triangle - outside microphone.

Since this energy is present in the ambient data both inside the cavity and outside the cavity, it is not related to the system dynamics. Its cause was not investigated in this preliminary experiment. 3) The pressure levels measured in the data runs are well above the ambient levels indicating good signal to noise levels.

The twelve spectra of this initial experiment (four plain plate, four unconstrained layers and four constrained layers) were integrated across frequency range and the results may be seen in Table 3.1. Since the area under the spectra is proportional to the power measured by the microphone, integration of the curve gives a broadband indication of the relative effectiveness of the four layers in decreasing the amount of vibratory energy converted to acoustic energy.

Layer material	601	606	609	601/609
plain	0.0932	0.0914	0.1007	0.0772
constrained	0.0491	0.0498	0.0547	0.0385
% constrained	47.3%	45.5%	45.7%	50.1%

Table 3. 1 Area under pressure spectra for each configuration

To account for differences in the four untreated base plates, a percent decrease in area of the curve is calculated (i.e. $100 * (p_{\text{plain}}^2 - p_{\text{treated}}^2)/p_{\text{plain}}^2$). As can be seen in the table, for this experiment the constrained spatially varying configuration showed the greatest decrease in measured acoustic power.

Measurements were also made of the plate's displacement at resonant frequencies using a PSV200 laser vibrometer system. These measurements were performed asynchronously from the pressure measurements. During the vibrometer measurements, the flexible plate was excited with a tone at a resonance frequency of the plate. The signal fed to speaker was used as an outside reference signal to PSV software to determine phase information in the measurement. PSV's "*Fast Scan*" option was used to perform the measurements.

Figure 3.8 displays the frequency response of the untreated plate as measured by the scanning vibrometer indicating the resonant frequencies.

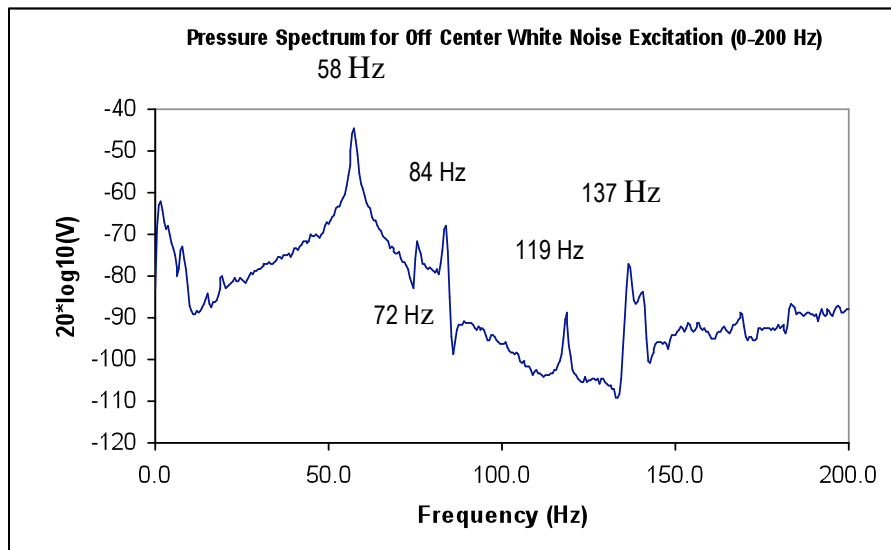
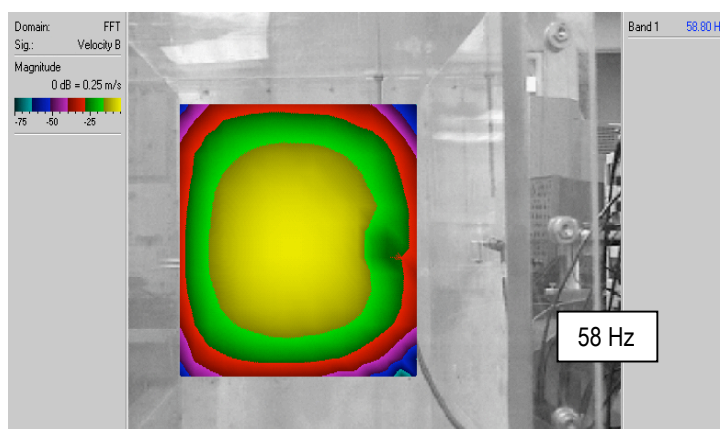


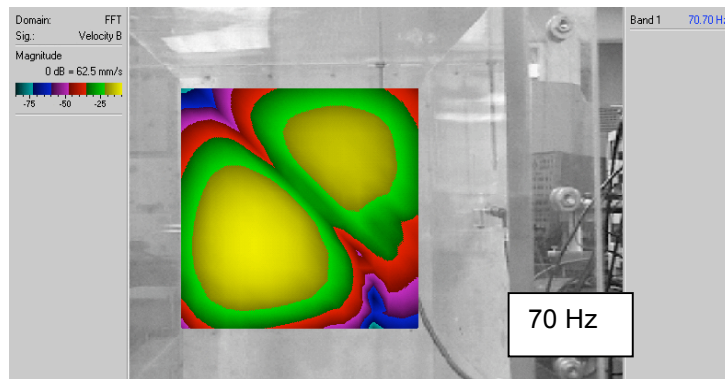
Figure 3.8: The frequency response of the untreated plate

In Figure 3.9 contour plots of the displacements of the plate at the first 5 resonances are presented. The resemblance to the first 5 mode shapes is clearly seen.

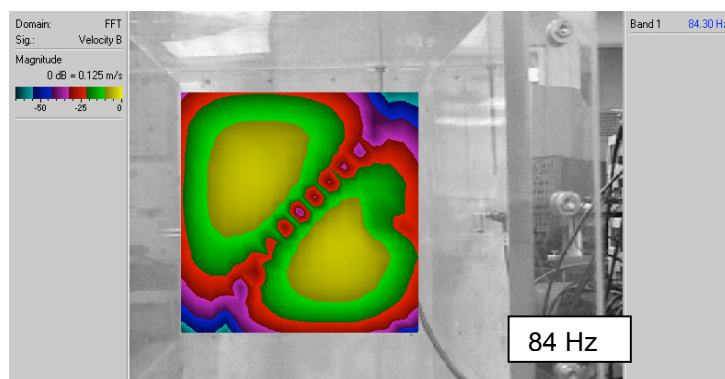
Figure 3.9: LDV displacement of untreated plate at first five resonant peaks.



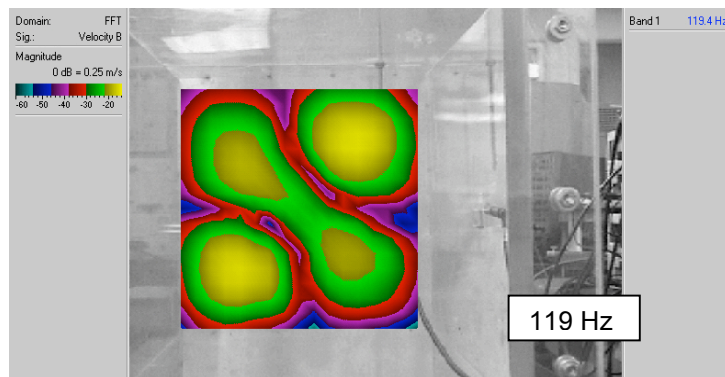
(a)



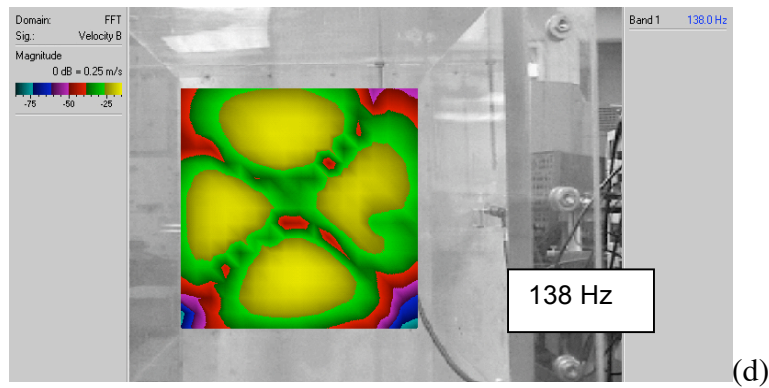
(b)



(c)



(d)

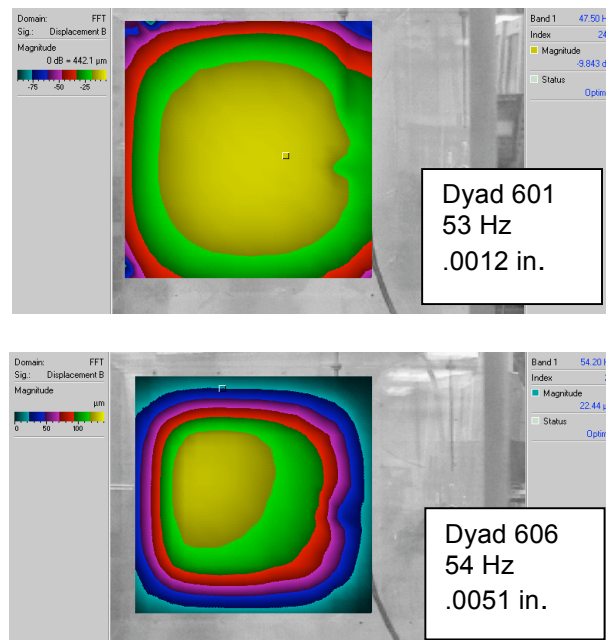


(e)

Figure 3.9: LDV displacement of untreated plate at first five resonant peaks.

Figure 3.10 displays the displacement pattern for the first resonances of the four plates with constrained viscoelastic layers as measured by the LDV system. On each of the contour plots for the plates with constrained viscoelastic layers, the name of the viscoelastic layer, the frequency of the first resonance and the maximum displacement of the measurement are labeled.

Figure 3.10 Displacement pattern at the first resonance for the four constrained viscoelastic layers. Material, resonance frequency and maximum displacement is labeled



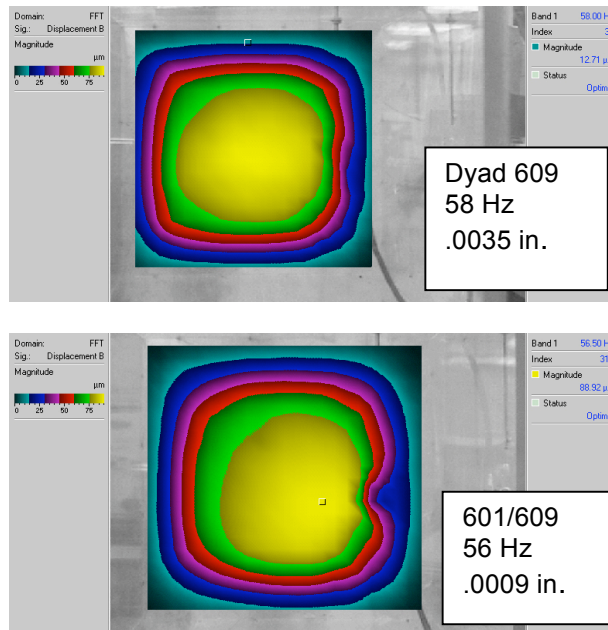


Figure 3.10 Displacement pattern at the first resonance for the four constrained viscoelastic layers. Material, resonance frequency and maximum displacement is labeled

Here as expected given the pressure level results, the plate with the spatially varying viscoelastic layer has the smallest displacement

3.4 Summary

The overall conclusion from this brief preliminary experiment is that it is worth investigating parametrically the use of a spatially varying viscoelastic layer for reducing the pressure field within and enclosed cavity. After guidelines have been numerically developed to steer choices of material and geometry of the constrained spatially varying viscoelastic layer, further experiments will be performed to verify the conclusions drawn.

Chapter 4

Generation of Dataset for Validation of Finite Element Model

The commercially available finite element (FE) computer code NASTRAN was used to create an initial model of the plate/cavity system that is under study. This was done to gain some experience in modeling the system before creating the new finite element code with the capability of modeling a spatially varying viscoelastic layer. The plate/cavity system will be described in detail in upcoming chapters.

4.1 Plate Model

The aluminum base plate was modeled in NASTRAN using plate elements. Contributions from bending and extension displacements (uncoupled) were included in the stiffness matrix. The base plate was modeled with a thickness of 0.016 inches, and an overall length of 12 inches. The material properties of aluminum used in the model were Young's modulus of 10.3×10^6 psi, mass density of 2.5244×10^{-4} lb-sec²/in⁴, and Poisson's Ratio of 0.33.

As discussed in Cramer *et al.* (1988), in the plate, the highest frequency bending waves will have the shortest wavelength. This point is illustrated in Figure 3.1.

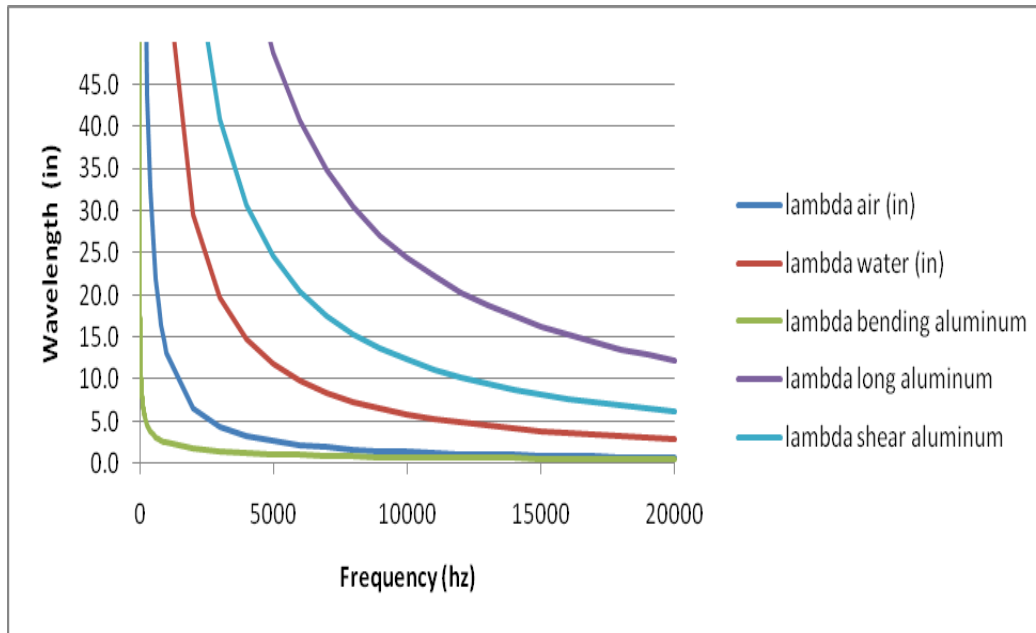


Figure 4. 1: A comparison of wavelengths for different wave types.

Here the wavelengths of different types of waves have been plotted against frequency for a 0.016 inch thick aluminum plate using the analytical expressions discussed in Cramer *et al.* (1988). It can be seen that especially at low frequency, the bending wavelength is much shorter than the wavelengths of the other wave types in the system. Thus a controlling factor in determining a grid resolution that will lead to a converged finite element solution is the bending wavelength of the highest frequency of interest. For a maximum frequency range of 200 Hz, the bending wavelength of the plate modeled is $\lambda = 5.57$ inches, for a maximum frequency range of 500 Hz the bending wavelength is 3.52 inches. NASTRAN recommends having between 5 and 10 grid points per half wavelength to achieve a resolved FE solution. With these guidelines and the overall length of the plate an appropriately sized element can be chosen.

From Flugge (1962), the frequencies for bending modes in a thin square plate may be calculated from the equation

$$f = \frac{\chi_i}{2\pi L^2} \sqrt{\frac{K}{\mu}} \quad (4.1)$$

$$K = \frac{E h^3}{12(1-\nu^2)} \quad \mu = \rho h$$

where L is the length of the plate's side and χ_i is a parameter for mode i which depends on the boundary conditions and is tabulated in Flugge. Clamped boundary conditions were used on all four sides. Using Equation 4.1, the first four eigen-frequencies of the plate were calculated to be 39.3 Hz, 79.40 Hz, 79.4 Hz, and 117.15 Hz. The eigen-frequencies output from the finite element program will be compared to these values. Note that since Flugge's expression was developed from Kirchoff theory without extensional displacements, while the NASTRAN elements do include extension, the converged numerical results may not exactly match the results from the analytical expression above.

Two plate elements developed for NASTRAN are the QUAD4 element, a four-node element, and the QUAD8 element that has an additional mid node on each side. Models of the plate were created using these two elements in meshes of varying resolution. Table 4.1 shows typical results.

Number of elements	Element Type	Number of Grid Points	First Eigen-frequency	Second/Third Eigen-frequency	Fourth Eigen-frequency
6 x 6	QUAD4	7 x 7	38.39	78.75	112.46
3 x 3	QUAD8	7 x 7	41.25	83.33	145.30
24 x 24	QUAD4	25 x 25	39.22	79.90	117.00
12 x 12	QUAD8	25 x 25	39.38	80.03	118.47
12 x 12	QUAD4	13 x 13	38.87	79.16	114.96
6 x 6	QUAD8	13 x 13	39.47	80.69	120.56
24 x 24	QUAD8	49 x 49	39.38	80.31	118.42
Thin plate (Kirchoff) theory			38.94	79.82	117.77

Table 4. 1: A comparison of the eigenvalues calculated for some different mesh sizes and element types of the C-C-C-C plate

Using the results of these and other trials it was decide to use a 12 x 12 element grid of QUAD8 elements for the base plate.

4.2 Cavity Model

Kinsler *et al.* (1999) give the following analytical expression for the eigen-frequencies a fluid-filled rectangular box with rigid walls:

$$f = \frac{c}{2\pi} \left[\left(\frac{l\pi}{L_x} \right)^2 + \left(\frac{m\pi}{L_y} \right)^2 + \left(\frac{n\pi}{L_z} \right)^2 \right]^{\frac{1}{2}} \quad (4.2)$$

For a 12 x 12 x 30 inch box filled with air, the first 4 frequencies are calculated to be 0 Hz, 225.06 Hz, 450.12 Hz, and 562.65 Hz.

The mesh of a fluid cavity can be coarser than that used for a structural analysis since the wavelength of the fluid's longitudinal wave will generally be longer than the wavelength of the structural element's bending wave. NASTRAN recommends 3 to 6 elements per wavelength. NASTRAN has an eight-node solid-fluid element and a 20-node solid-fluid element. After performing convergence studies like those mentioned above, it was decided to use 20-node solid elements in a 12 x 12 x 12 element mesh. The 8 node element was less accurate and although a coarser mesh of 20-node elements gave reasonable results, it was decided that since there was little computational time increase for a 12 x 12 x 12 mesh compared to a 6 x 6 x 6 mesh, the simplification of joining the air model to the plate model warranted the extra elements in the air model. The finer grid also would allow the location of the microphone in the experimental apparatus to be modeled more directly. The eigenvalues calculated by NASTRAN for the 12 x 12 x 12 mesh of 20 node elements were 8.96×10^{-6} Hz, 225.07 Hz, 450.16 Hz, and 562.67 Hz. The eigenvalues calculated by NASTRAN for the 12 x 12 x 12 mesh of 8 node elements were 4.06×10^{-5} Hz, 225.70 Hz, 455.29 Hz, and 564.27 Hz.

Once the models for the plate and cavity gave good eigenvalues, NASTRAN's coupled fluid/structure analysis was used to calculate eigenvalues for the coupled system. This analysis gave the following eigenvalues below 200 Hz for the coupled system: 0 Hz, 55.67 Hz, 77.8 Hz, 77.8 Hz, 115.8 Hz, 140.7 Hz, 141.2 Hz, and 177.5 Hz.

4.3 Loading

To model the loading of the speaker broadcasting white noise towards the plate, the spectra from a microphone monitoring the pressures outside the enclosure during the experiment was used. The magnitude only was used in the loading for the NASTRAN model. Using no phase information in the loading assumes constant phase across frequency. This is a reasonable assumption since the wavelength in air at the highest frequency of interest (200 Hz) is 67 inches and the speaker is 1 to 4 inches away from the plate.

A table of pressure *vs.* frequency was entered using values of pressure taken from the external microphone. For frequencies between entries on the table, the pressure was interpolated using a log scale. These values of pressure are then used to define a dynamic excitation for each loaded grid point

$$\{F_p\} = \{B(f)e^{i\phi(f)}\} \quad (4.3)$$

Here $B(f)$ is the table of pressure magnitudes mentioned above. $\phi(f)$ is the table of phase values, which is in this case not used. The frequency range for this analysis extended from 0.5 Hz to 200 Hz in increments of 0.5 Hz. The structural response is calculated using a direct frequency response scheme that solves the system of equations

$$[-\omega^2 M + i\omega B + K]\{a(\omega)\} = \{F_p(\omega)\}$$

for each frequency ω .

Figure 4.2 presents the result of the NASTRAN model of the plain plate/cavity in comparison with the experimental data.

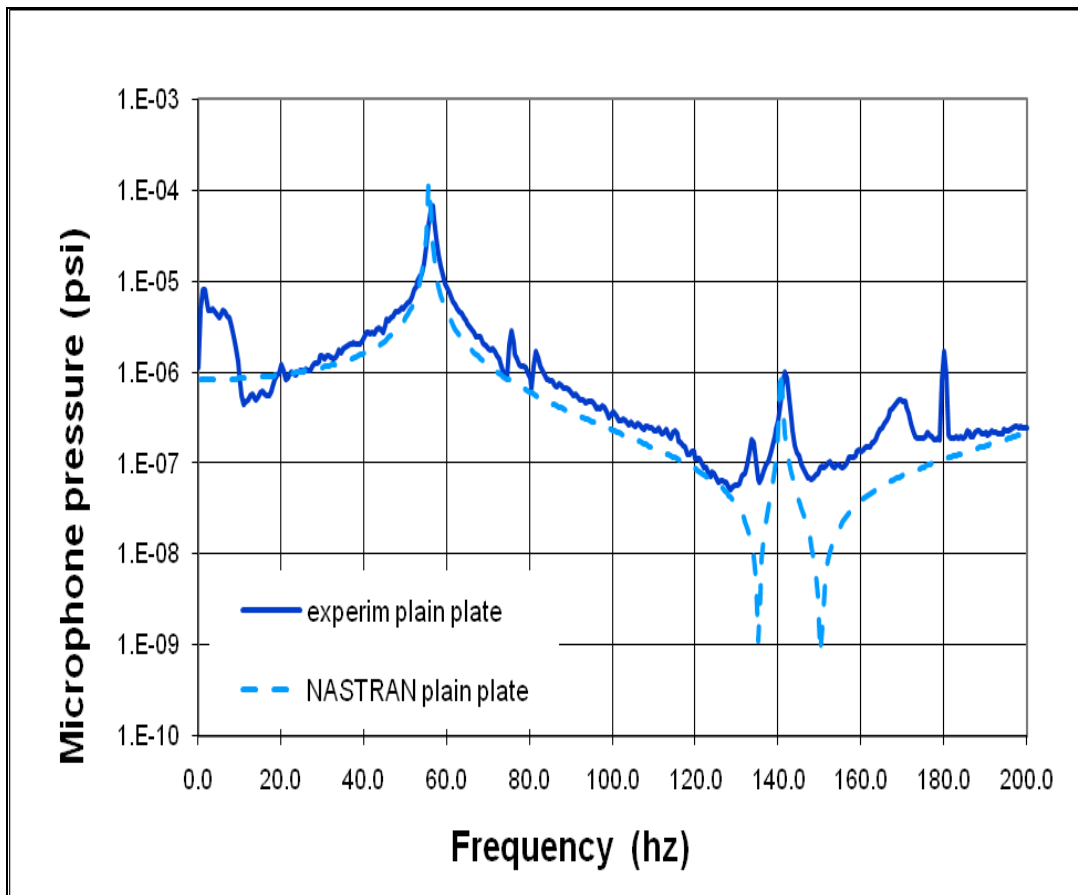


Figure 4.2: Comparison of NASTRAN results with experimental data for the untreated plate/cavity system

Overall the results are good. As discussed in the chapter pertaining to the preliminary experiment, there is a band of very low frequency energy that is not related to the plate cavity system (it is apparent in the ambient data when there is no excitation) that does not appear in the NASTRAN model but the frequencies and magnitudes of the resonances at 55 Hz and 150 Hz show good agreement.

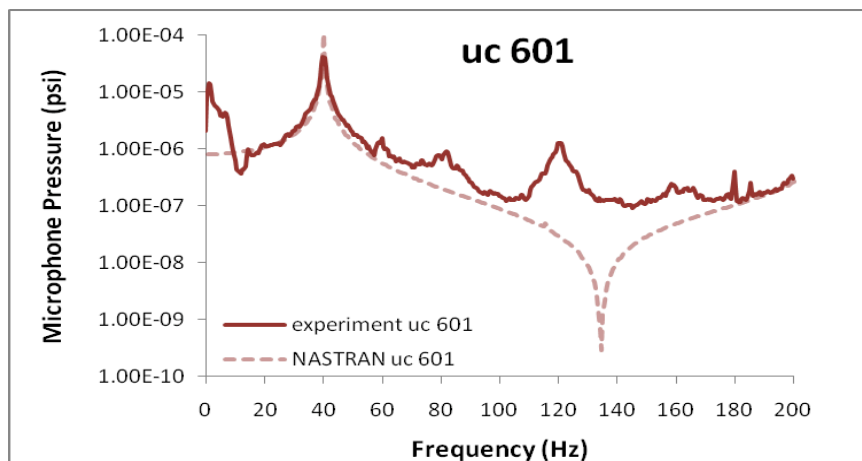
4.4 Viscoelastic and Constraining Layer Models

A single layer of 20-node solid elements was used to model the viscoelastic layer in NASTRAN. NASTRAN has the capability to represent one frequency dependent complex modulus in a model of the form

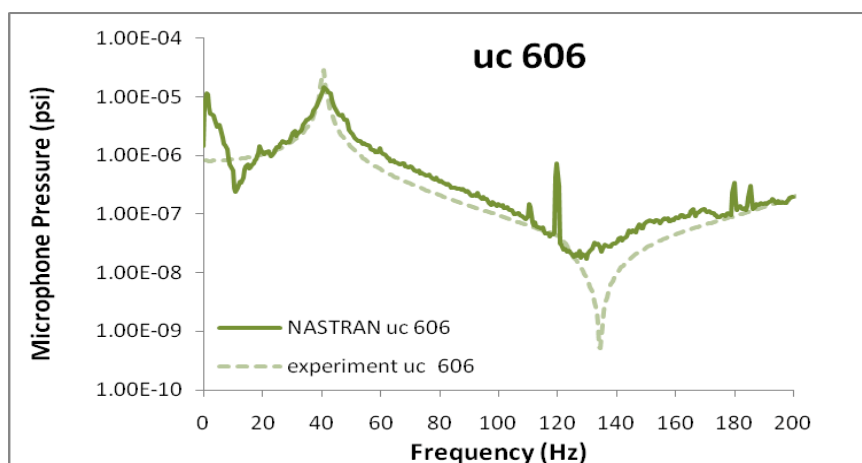
$$G(f) = G'(f) + iG''(f)$$

where $G'(f)$ is the storage modulus and $G''(f)$ is the loss modulus. Using the material properties plotted in Figure 4.4, suitable tables of modulus vs. frequency were created and used in the NASTRAN model. Figure 3.3 presents the comparison of NASTRAN results with experimental data for an unconstrained viscoelastic layer. A NASTRAN run was made for each of the three viscoelastic materials used in the preliminary experiment.

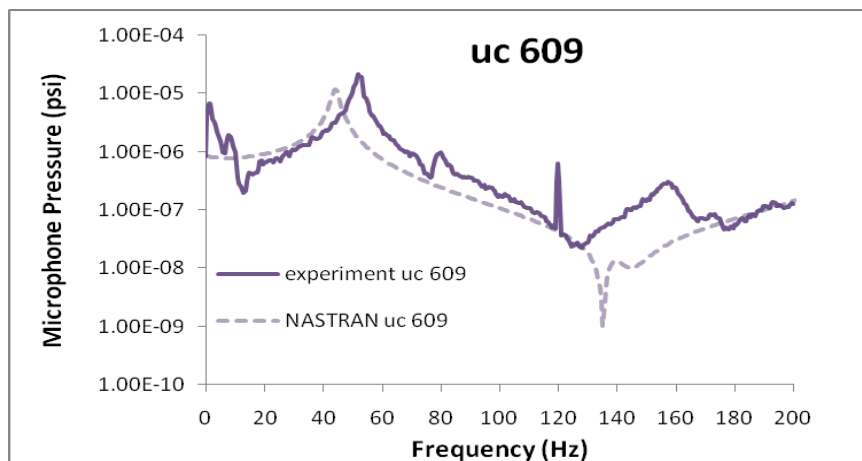
Once the NASTRAN models of the unconstrained configurations ran successfully, an additional layer of thin 8-node plate elements was added on top of the viscoelastic layer to model the constraining layer in the experiment. The results are presented in Figure 4.3



(a) – Dyad 601

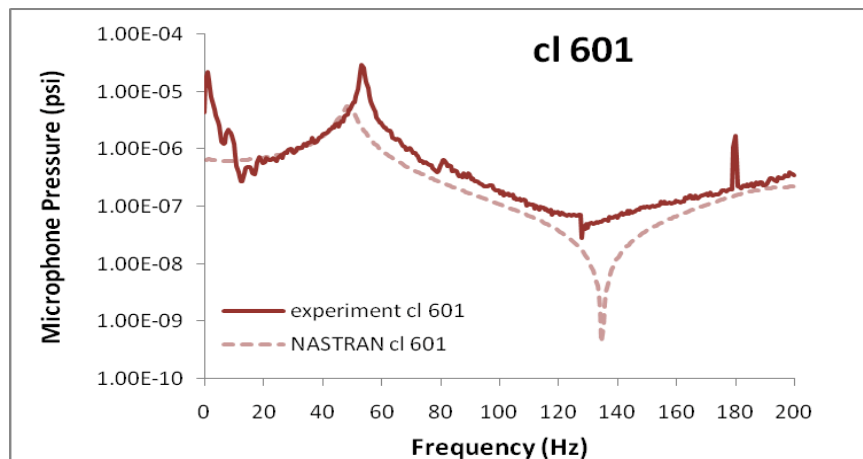


(b) – Dyad 606

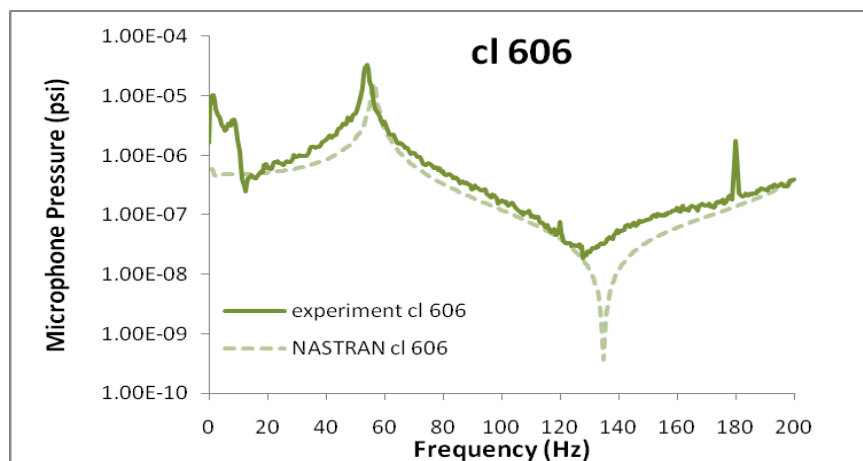


(c) - Dyad 609

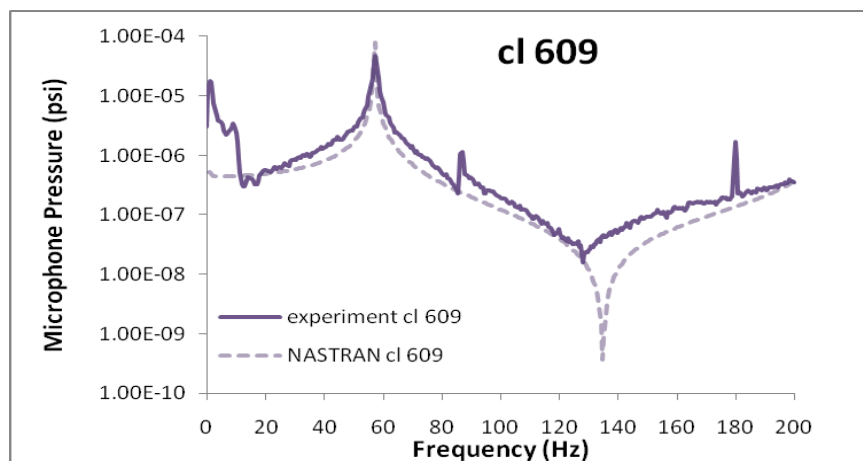
Figure 4.3: Comparison of NASTRAN model and experimental pressure data for unconstrained viscoelastic configurations



(a) Dyad 601



(b) Dyad 606



(c) Dyad 609

Figure 4.4: Comparison of experimental pressure data and NASTRAN model for constrained configurations

4.5 Summary

For the most part, the agreement of the NASTRAN model and the experimental data was very good especially at the first resonance in the system. However, for the stiffest (DYAD 609) unconstrained configuration and the softest (DYAD 601) constrained configuration NASTRAN's performance degraded to some extent. Since NASTRAN was primarily being used to bound modeling parameters and to gain modeling experience for the system, this phenomenon was noted but not further investigated. The version of NASTRAN used for this study was not able to model multi material configurations because the complex modulus feature allows only one frequency dependent material. As mentioned above, the constrained layer configuration could only be modeled in NASTRAN using a combination of shell elements for the base plate, solid elements for the viscoelastic layer and shell elements for the constraining layer.

Chapter 5

Finite Element Model of Viscoelastically Damped Plates Coupled with an Acoustic Cavity

5.1 Finite Element Model for Untreated Plate – Strain Energy

Having developed weak forms of the equilibrium model for a *Reissner-Mindlin plate* in Chapter 2, this chapter traces the development of the finite element model to be used for this study.

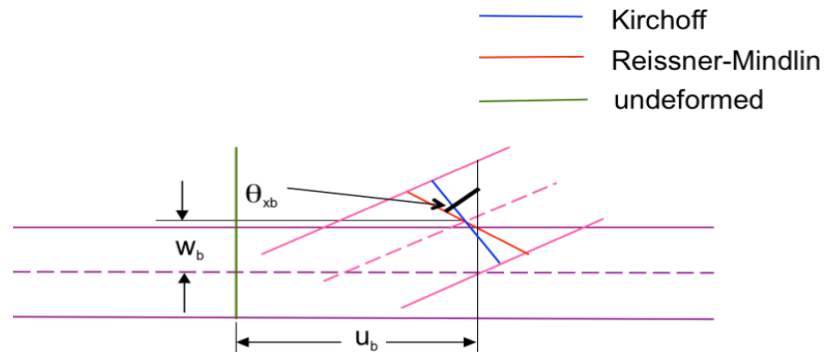


Figure 5. 1: Geometry for plain plate kinematics

The displacements strains and stresses to be used are expressed in Eqs. 2.1-3 of Chapter 2. Note that because of the 3-D to 2-D simplifications resulting from plate theory, the out-of-plane strains each can be thought of as having two parts:

$$\begin{aligned}\epsilon_{xx} &= \epsilon_{xx}^{LS} + \epsilon_{xx}^B \\ \epsilon_{yy} &= \epsilon_{yy}^{LS} + \epsilon_{yy}^B \\ \gamma_{xy} &= \gamma_{xy}^{LS} + \gamma_{xy}^B\end{aligned}$$

where the superscript *LS* refers to longitudinal shear and the superscript *B* refers to bending. The strain energy is

$$\begin{aligned}U &= U_B + U_{LS} + U_{TS} \\ &= \frac{1}{2} \int_{\Omega} \left(\begin{aligned} &\sigma_{xxB} \epsilon_{xxB} + \sigma_{yyB} \epsilon_{yyB} + \sigma_{xyB} \gamma_{xyB} \\ &+ \sigma_{xxLS} \epsilon_{xxLS} + \sigma_{yyLS} \epsilon_{yyLS} + \sigma_{xyLS} \gamma_{xyLS} \\ &+ \sigma_{xzTS} \gamma_{xzTS} + \sigma_{yzTS} \gamma_{yzTS} \end{aligned} \right) d\Omega\end{aligned}$$

Here and elsewhere in this document, *LS* denotes longitudinal shear, *B* denotes bending and *TS* denotes transverse shear. Note that in the above equation, cross terms like σ_{xxLS} , and ϵ_{xxB} are not present. This is because these terms when expanded, are multiplied by z and so when they are integrated through the thickness of the plate ($-t/2$ to $t/2$) tend to zero. Thus, for an untreated plate, the longitudinal and bending components can be calculated independently, *i.e.* the longitudinal and bending strain energy are uncoupled. This can be advantageous computationally since the smaller matrices are easier to invert. However, the kinematic model developed for the treated plate causes the longitudinal strain and stress (ϵ_{xxLS} and σ_{xxLS}) to be functions of both the extensions and the rotations, so the final FE model developed calculates strain and kinetic energy with all degrees of freedom coupled for both a plain plate element and a treated plate element.

As described earlier, the virtual work equations (Eqs. 2.9a-c and Eqs. 2.12a-b) can be developed using expressions for strain and stress in the strain and potential energy

equations. Looking at the terms in the virtual work equations, one can see that for the untreated plate, terms involving strains that occur because of plate bending ($\varepsilon_{xxB}, \varepsilon_{yyB}, \gamma_{xyB}$) are only functions of the rotations θ_x and θ_y , terms involving strains that occur because of plate longitudinal shear ($\varepsilon_{xxLS}, \varepsilon_{yyLS}, \gamma_{xyLS}$) are only functions of u and v , and terms involving strains that occur because of plate transverse shear ($\varepsilon_{xzTS}, \varepsilon_{yzTS}, \gamma_{xyTS}$) are functions of w , θ_x and θ_y . Thus, the five virtual work equations can be separated into parts that contribute to bending, longitudinal shear and transverse shear and then organized in matrix form. The matrix form of the virtual work equations can then be written:

$$\begin{aligned}
& \int_A \int_{-h/2}^{h/2} \left[\delta \varepsilon_{xxB} \delta \varepsilon_{yyB} \delta \gamma_{xyB} \right] \begin{Bmatrix} \sigma_{xxB} \\ \sigma_{yyB} \\ \tau_{xyB} \end{Bmatrix} dz dA + \int_A \int_{-h/2}^{h/2} \left[\delta \varepsilon_{xxLS} \delta \varepsilon_{yyLS} \delta \gamma_{xyLS} \right] \begin{Bmatrix} \sigma_{xxLS} \\ \sigma_{yyLS} \\ \tau_{xyLS} \end{Bmatrix} dz dA \\
& \quad \text{bending} \rightarrow F(\theta_x, \theta_y) \qquad \qquad \qquad \text{longitudinal shear} \rightarrow F(u, v) \\
& + \int_A \int_{-h/2}^{h/2} \left[\delta \gamma_{xzTS} \delta \gamma_{yzTS} \right] \begin{Bmatrix} \tau_{xzTS} \\ \tau_{yzTS} \end{Bmatrix} dz dA \qquad \qquad \qquad (5.1) \\
& \quad \text{transverse shear} \rightarrow F(w, \theta_x, \theta_y)
\end{aligned}$$

$$\begin{aligned}
& + \text{KineticEnergy} + \text{BoundaryTerms} + \text{Work} = 0 \\
& F(w, \theta_x, \theta_y, u, v)
\end{aligned}$$

5.2 Discretization

Now that we have an expression for virtual work in matrix form, the next step is to discretize the independent variables. Following the ideas presented by Hughes and Tezduyar (1981) and also by Bathe and Dvorkin (1985), a four-node quadrilateral plate element is used in this study. Four-noded elements with the associated simple shape functions are used to compensate for the additional algebraic complexity introduced by

the kinematic model of the three layer viscoelastic element that was created for this work. Also, it was decided to use direct rather than numerical integration for the calculation of strain energy in the finite element program and this was facilitated by the use of the simple shape functions. Future work could increase the order of the shape functions if accuracy appears to be adversely affected by the bilinear shape functions employed currently.

For a plain plate element, each node is assumed to have seven degrees of freedom, w , α_x , α_y , β_x , β_y , u , and v . Here, the rotational angle θ has been broken into two parts, a shear angle α and a bending angle β (which for small displacements can be taken to be the spatial derivative dw/dx as is done in *Kirchoff plate theory*). The sum of α and β is θ ($\theta=\alpha+\beta$). The reasons for why this expression of the rotational angle was chosen will be discussed in the section on the development of the three layer element later in this chapter. The element coordinate system whose origin is taken to be the center of the element is shown in Figure 5.2

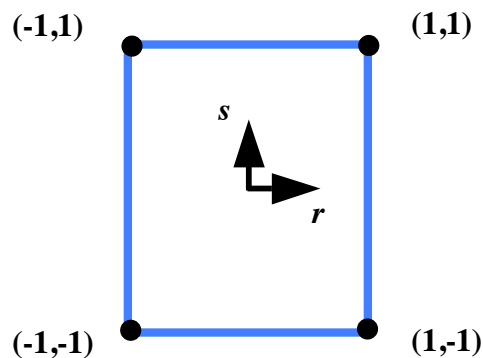


Figure 5. 2: Four-node quadrilateral element

Given the shape functions and their derivatives with respect to r and s as follows:

$$\begin{aligned}
N_1 &= \frac{1}{4} (1+r)(1+s) & N_{1,r} &= \frac{1}{4}(1+s) & N_{1,s} &= \frac{1}{4}(1+r) \\
N_2 &= \frac{1}{4} (1-r)(1+s) & N_{2,r} &= -\frac{1}{4}(1+s) & N_{2,s} &= \frac{1}{4}(1-r) \\
N_3 &= \frac{1}{4} (1-r)(1-s) & N_{3,r} &= -\frac{1}{4}(1+s) & N_{3,s} &= -\frac{1}{4}(1+r) \\
N_4 &= \frac{1}{4} (1+r)(1-s) & N_{4,r} &= \frac{1}{4}(1-s) & N_{4,s} &= -\frac{1}{4}(1+r)
\end{aligned} \tag{5.2}$$

We will express the displacements and, since the formulation is isoparametric, global coordinates as

$$\begin{aligned}
u(r,s) &= \sum_{i=1}^4 N_i u_i & v(r,s) &= \sum_{i=1}^4 N_i v_i & w(r,s) &= \sum_{i=1}^4 N_i w_i \\
\alpha_x(r,s) &= \sum_{i=1}^4 N_i \alpha_{xi} & \alpha_y(r,s) &= \sum_{i=1}^4 N_i \alpha_{yi} \\
\beta_x(r,s) &= \sum_{i=1}^4 N_i \beta_{xi} & \beta_y(r,s) &= \sum_{i=1}^4 N_i \beta_{yi} \\
x(r,s) &= \sum_{i=1}^4 N_i x_i & y(r,s) &= \sum_{i=1}^4 N_i y_i
\end{aligned} \tag{5.3}$$

where i is the index on the node numbers. Since the displacements at the nodes are constants, the derivatives for u are expressed as

$$\frac{\partial u}{\partial r} = \sum_{i=1}^n N_{i,r} u \qquad \frac{\partial u}{\partial s} = \sum_{i=1}^n N_{i,s} u \tag{5.4}$$

and derivatives with respect to r and s for the other independent variables and global coordinates may be written similarly. The local derivatives are related to the global coordinate system via the Jacobian matrix:

$$\begin{Bmatrix} \frac{\partial}{\partial x} \\ \frac{\partial}{\partial y} \end{Bmatrix} = [J] \begin{Bmatrix} \frac{\partial}{\partial r} \\ \frac{\partial}{\partial s} \end{Bmatrix} = \begin{bmatrix} \frac{\partial r}{\partial x} & \frac{\partial s}{\partial x} \\ \frac{\partial r}{\partial y} & \frac{\partial s}{\partial y} \end{bmatrix} \begin{Bmatrix} \frac{\partial}{\partial r} \\ \frac{\partial}{\partial s} \end{Bmatrix}$$

When equations 5.2 through 5.4 are substituted into equation 2.3, discretized forms of the strain are generated. For convenience in computing, the strains are broken into contributions from bending, longitudinal shear (extension) and transverse shear. These are defined as

$$\begin{aligned} \text{longitudinal shear strain } \varepsilon_{LS} &= \begin{Bmatrix} \frac{\partial u}{\partial x} \\ \frac{\partial v}{\partial y} \\ \frac{\partial u}{\partial y} + \frac{\partial v}{\partial x} \end{Bmatrix} = \begin{Bmatrix} \frac{\partial u}{\partial r} \frac{\partial r}{\partial x} \\ \frac{\partial v}{\partial s} \frac{\partial s}{\partial y} \\ \frac{\partial u}{\partial s} \frac{\partial s}{\partial y} + \frac{\partial v}{\partial r} \frac{\partial r}{\partial x} \end{Bmatrix} \quad (5.5) \\ \text{bending strain } \varepsilon_B &= -z \begin{Bmatrix} \frac{\partial \alpha_x}{\partial x} + \frac{\partial \beta_x}{\partial x} \\ \frac{\partial \alpha_y}{\partial y} + \frac{\partial \beta_y}{\partial y} \\ \frac{\partial \alpha_x}{\partial y} + \frac{\partial \beta_x}{\partial y} + \frac{\partial \alpha_y}{\partial x} + \frac{\partial \beta_y}{\partial x} \end{Bmatrix} = -z \begin{Bmatrix} \left(\frac{\partial \alpha_x}{\partial r} + \frac{\partial \beta_x}{\partial r} \right) \frac{\partial r}{\partial x} \\ \left(\frac{\partial \alpha_y}{\partial s} + \frac{\partial \beta_y}{\partial s} \right) \frac{\partial s}{\partial y} \\ \left(\frac{\partial \alpha_x}{\partial s} + \frac{\partial \beta_x}{\partial s} \right) \frac{\partial s}{\partial y} + \left(\frac{\partial \alpha_y}{\partial r} + \frac{\partial \beta_y}{\partial r} \right) \frac{\partial r}{\partial x} \end{Bmatrix} \\ \text{transverse shear strain } \varepsilon_{TS} &= \begin{Bmatrix} \gamma_{xz} \\ \gamma_{yz} \end{Bmatrix} = \begin{Bmatrix} \frac{\partial w}{\partial x} - (\alpha_x + \beta_x) \\ \frac{\partial w}{\partial y} - (\alpha_y + \beta_y) \end{Bmatrix} = \begin{Bmatrix} \frac{\partial w}{\partial r} \frac{\partial r}{\partial x} - (\alpha_x + \beta_x) \\ \frac{\partial w}{\partial s} \frac{\partial s}{\partial y} - (\alpha_y + \beta_y) \end{Bmatrix} \end{aligned}$$

We define the vectors containing the displacements of a 4-node plain plate as follows:

$$\begin{aligned}
a_{LS} &= [u_1 v_1 u_2 v_2 u_3 v_3 u_4 v_4] \\
a_B &= [\alpha_{x1} \alpha_{y1} \beta_{x1} \beta_{y1} \alpha_{x2} \alpha_{y2} \beta_{x2} \beta_{y2} \alpha_{x3} \alpha_{y3} \beta_{x3} \beta_{y3} \alpha_{x4} \alpha_{y4} \beta_{x4} \beta_{y4}] \\
a_{TS} &= [w_1 \alpha_{x1} \alpha_{y1} \beta_{x1} \beta_{y1} w_2 \alpha_{x2} \alpha_{y2} \beta_{x2} \beta_{y2} w_3 \alpha_{x3} \alpha_{y3} \beta_{x3} \beta_{y3} w_4 \alpha_{x4} \alpha_{y4} \beta_{x4} \beta_{y4}]
\end{aligned}$$

Then, using the derivatives from 5.4 and a discretized expression of the independent variables and global coordinates from equation 5.3 in the strain expressions of 5.5, the discretized forms of the strains (and virtual strains) can be written in matrix form as

$$\begin{aligned}
\{\varepsilon_{LS}\} &= [B_{LS}] \{a_{LS}\} \quad \{\varepsilon_B\} = [B_B] \{a_B\} \quad \{\varepsilon_{TS}\} = [B_{TS}] \{a_{TS}\} \\
\text{and} & \\
\{\delta\varepsilon_{LS}\} &= [B_{LS}] \{\delta a_{LS}\} \quad \{\delta\varepsilon_B\} = [B_B] \{\delta a_B\} \quad \{\delta\varepsilon_{TS}\} = [B_{TS}] \{\delta a_{TS}\}
\end{aligned} \tag{5.6}$$

where $[B]$ is the matrix of appropriate derivatives with respect to s and r .

The transverse shear strain combines a first order spatial derivative of the transverse displacement with a zeroth order derivative of the rotation. Since the same shape functions are being used to interpolate w and θ , the order of the polynomial approximating the part of transverse shear due to the derivative of the transverse displacement is one degree lower than the polynomial approximating the part of transverse shear due to the rotation. The ultimate result of this mismatch is that when full integration is used for transverse shear in a thin element (where the transverse shear approaches zero), the element tends to be too stiff. If however, the interpolation polynomials are evaluated at points in the element where the extra higher order terms in the rotation polynomial become zero, balance is restored and the transverse shear can tend to zero as it should for the thin plate case. This was pointed out by MacNeal (1978) and further developed by Hughes and Tezduyar (1981).

Hughes (1980) describes a method of incorporating the effective reduced integration of the transverse shear. Basically, the transverse shear is evaluated at the midpoints of the sides where θ_x and θ_y , which are, in general, linear functions of r and s respectively, retain only the constant term in the interpolation polynomial. Then once this is done, the transverse shears in the x and y direction are interpolated to the center point of the element. Displacements from all four nodes of the element contribute to the transverse shear of the element in an interpolated sense.

For implementation purposes this means that the transverse shear element matrix is modeled as

$$\varepsilon_{TS} = \left[\begin{array}{l} \frac{(1+s)}{2} \left(\frac{w_1 - w_2}{L_x} - \frac{(\alpha_{x1} + \beta_{x1}) + (\alpha_{x2} + \beta_{x2})}{2} \right) + \frac{(1-s)}{2} \left(\frac{w_4 - w_3}{L_x} - \frac{(\alpha_{x4} + \beta_{x4}) + (\alpha_{x3} + \beta_{x3})}{2} \right) \\ \frac{(1+r)}{2} \left(\frac{w_1 - w_4}{L_y} - \frac{(\alpha_{x1} + \beta_{x1}) + (\alpha_{x4} + \beta_{x4})}{2} \right) + \frac{(1-r)}{2} \left(\frac{w_2 - w_3}{L_y} - \frac{(\alpha_{x2} + \beta_{x2}) + (\alpha_{x3} + \beta_{x3})}{2} \right) \end{array} \right]$$

Once the strains have been expressed in matrix form expressions for stresses are generated. Because very small displacements are the reality in this investigation, Hooke's Law is an appropriate constitutive model. The constitutive matrices for the plain plate are defined as

$$\hat{D} = \frac{E}{(1-\nu^2)} \begin{bmatrix} 1 & \nu & 0 \\ \nu & 1 & 0 \\ 0 & 0 & \frac{1-\nu}{2} \end{bmatrix} \quad \tilde{D} = \frac{E}{2(1+\nu)} \begin{bmatrix} 1 & 0 \\ 0 & 1 \end{bmatrix} \quad (5.7a)$$

where E is the Young's Modulus and ν is the Poisson's Ratio. Now the stresses may be written in matrix form as

$$\{\sigma_{LS}\} = \left\{ \sigma_{xx}^{LS} \quad \sigma_{yy}^{LS} \quad \gamma_{xy}^{LS} \right\}^T = [\hat{D}] \{\varepsilon_{LS}\} \quad \{\sigma_B\} = \left\{ \sigma_{xx}^B \quad \sigma_{yy}^B \quad \gamma_{xy}^B \right\}^T = [\hat{D}] \{\varepsilon_{LS}\} \quad (5.7b)$$

$$\{\sigma_{TS}\} = \left\{ \gamma_{xz}^{TS} \quad \gamma_{yz}^{TS} \right\}^T = [\tilde{D}] \{\varepsilon_{LS}\}$$

When equations 5.6 and 5.7a-b are substituted into 5.1 and the resulting expression is integrated over the thickness h (z direction), we have the following

$$\begin{aligned} h \int_{-1}^1 \int_{-1}^1 \{\delta\varepsilon_{LS}\}^T \{\sigma_{LS}\} \det J \, dr \, ds &= \{\delta a_{LS}\}^T \int_{-1}^1 \int_{-1}^1 [B_{LS}]^T [D_{LS}] [B_{LS}] \det J \, dr \, ds \{a_{LS}\} \\ &= \{\delta a_{LS}\}^T [\hat{K}_{LS}] \{a_{LS}\} \end{aligned}$$

$$\begin{aligned} \frac{h^3}{12} \int_{-1}^1 \int_{-1}^1 \{\delta\varepsilon_B\}^T \{\sigma_B\} \det J \, dr \, ds &= \{\delta a_B\}^T \int_{-1}^1 \int_{-1}^1 [B_B]^T [D_B] [B_B] \det J \, dr \, ds \{a_B\} \\ &= \{\delta a_B\}^T [\hat{K}_B] \{a_B\} \end{aligned}$$

$$\begin{aligned} h \int_{-1}^1 \int_{-1}^1 \{\delta\varepsilon_{TS}\}^T \{\sigma_{TS}\} \det J \, dr \, ds &= \{\delta a_{TS}\}^T \int_{-1}^1 \int_{-1}^1 [B_{TS}]^T [D_{TS}] [B_{TS}] \det J \, dr \, ds \{a_{TS}\} \\ &= \{\delta a_{TS}\}^T [\hat{K}_{TS}] \{a_{TS}\} \end{aligned}$$

where

$$D_{LS} = t \hat{D} \quad D_B = \frac{t^3}{12} \hat{D} \quad D_{TS} = t \tilde{D}$$

Writing all the degrees of freedom together in a single vector $\{a\}$ of element displacements and creating the sparse matrices K_{LS} , K_B , and K_{TS} from their hatted counterparts (\hat{K}_{LS} etc.) above, we can rewrite equation 5.1 as

$$\begin{aligned} \{\delta a\}^T [K_{LS} + K_B + K_{TS}] \{a\} + K.E. + Work &= 0 \quad (5.8) \\ \text{or} \quad \{\delta a\}^T [K_{el}] \{a\} + K.E. + Work &= 0 \end{aligned}$$

where

$$a = \left[u_1 \, v_1 \, w_1 \, \alpha_{x1} \, \alpha_{y1} \, \beta_{x1} \, \beta_{y1} \, u_2 \, v_2 \, w_2 \, \alpha_{x2} \, \alpha_{y2} \, \beta_{x2} \, \beta_{y2} \, u_3 \, v_3 \, w_3 \, \alpha_{x3} \, \alpha_{y3} \, \beta_{x3} \, \beta_{y3} \, u_4 \, v_4 \, w_4 \, \alpha_{x4} \, \alpha_{y4} \, \beta_{x4} \, \beta_{y4} \right]$$

and K_{el} is the element stiffness matrix.

5.3 Finite Element Model for Untreated Plate – Kinetic Energy

After integration over the thickness, the kinetic energy for the plain plate may be expressed as

$$T = T_{LS} + T_B + T_{TS} = \frac{1}{2} \int \int \rho h (\dot{w} + \dot{u} + \dot{v}) + \frac{\rho h^3}{12} (\dot{\alpha}_x^2 + \dot{\alpha}_y^2 + \dot{\beta}_x^2 + \dot{\beta}_y^2 + \dot{\alpha}_x \dot{\beta}_x + \dot{\alpha}_y \dot{\beta}_y) dA$$

Note that after integration over the thickness, no coupling remains between the transverse and rotational displacement for the untreated plate. Coupling between rotational degrees of freedom is still present, however. Using the variation of this expression in the virtual work equation above we have

$$\text{Strain Energy} + \int \int_A \left(\delta \alpha_x \rho \frac{h^3}{8} \ddot{\alpha}_x + \delta \alpha_y \rho \frac{h^3}{8} \ddot{\alpha}_y + \delta \beta_x \rho \frac{h^3}{8} \ddot{\beta}_x + \delta \beta_y \rho \frac{h^3}{8} \ddot{\beta}_y \right) dA + \text{Work} = 0 \quad (5.9)$$

$$+ \delta u \rho h \ddot{u} + \delta v \rho h \ddot{v} + \delta w \rho h \ddot{w}$$

Now we use the shape functions in equation 5.2 to write the various terms in the variation of the kinetic energy equation in matrix form. For example, the term involving α_x becomes

$$\delta \alpha_x \ddot{\alpha}_x = (N \delta \alpha_x)^T N \ddot{\alpha}_x = \delta \alpha_x^T N^T N \ddot{\alpha}_x$$

Then, rewriting the above in matrix form

$$\begin{aligned}
S.E - \delta\alpha_x^T \rho \frac{h^3}{8} \int \int N^T N \det J dr ds \ddot{\alpha}_x - \delta\alpha_y^T \rho \frac{h^3}{8} \int \int N^T N \det J dr ds \ddot{\alpha}_y & \quad (5.10) \\
- \delta\beta_x^T \rho \frac{h^3}{8} \int \int N^T N \det J dr ds \ddot{\beta}_x - \delta\beta_y^T \rho \frac{h^3}{8} \int \int N^T N \det J dr ds \ddot{\alpha}_y \\
- \delta w^T \rho h \int \int N^T N \det J dr ds \ddot{w} - \delta u^T \rho h \int \int N^T N \det J dr ds \ddot{u} \\
- \delta v^T \rho h \int \int N^T N \det J dr ds \ddot{v} + B.C. + Work = 0
\end{aligned}$$

or

$$\begin{aligned}
S.E. - \delta\alpha_x^T [\hat{M}] \ddot{\alpha}_x - \delta\alpha_y^T [\hat{M}] \ddot{\alpha}_y - \delta\beta_x^T [\hat{M}] \ddot{\beta}_x - \delta\beta_y^T [\hat{M}] \ddot{\beta}_y - \delta w^T [\tilde{M}] \ddot{w} - \delta u^T [\tilde{M}] \ddot{u} \\
- \delta v^T [\tilde{M}] \ddot{v} - Q^T p + Work = 0
\end{aligned}$$

where

$$[\hat{M}] = \rho \frac{h^3}{8} \int \int N^T N \det J dr ds$$

$$[\tilde{M}] = \rho h \int \int N^T N \det J dr ds$$

$$Q = \int \int N_f^T N dr ds$$

To combine this with the final form of 5.9 the element displacement vector is used and the sub matrices $[\hat{M}]$ and $[\tilde{M}]$ are combined appropriately in a sparse matrix. Since δa is an arbitrary function this gives the final result for the structure:

$$[K_{el}] \{a\} + [M_{el}] \{\ddot{a}\} - Q^T p + Work = 0 \quad (5.11)$$

5.4 Finite Element Model – Load Vector

The loading for this investigation was generated by a loudspeaker which was facing the plate and broadcasting a white noise acoustic signal. The details of the data is discussed more thoroughly in Chapters 4 and 5. The signal level was on the order of $p(\omega)=1 \times 10^{-6}$ psi. This is modeled in the finite element model as a plane wave ($F(\omega)=p(\omega)e^{i\omega t}$). The load vector was developed by identifying the grid points that

would be within a 6.5" square at the center of the plate (based on the arrangement of the experimental apparatus) and applying $F(\omega)$.

5.5 Finite Element Model for Acoustic Cavity

As developed in many texts that discuss the topic of acoustics (e.g. Kinsler *et al.* (1999)) the following three linearized equations

$$\begin{aligned} \ddot{u}_f &= -\frac{1}{\rho_0} \nabla p && \text{equilibrium equation} \\ p &= c^2 \rho_0 s && \text{constitutive equation} \\ \nabla \cdot \dot{u}_f &= -\frac{\partial s}{\partial t} && \text{continuity equation} \end{aligned} \quad (5.12)$$

may be combined to form a single equation known as the linearized lossless wave equation:

$$\nabla^2 p = \frac{1}{c^2} \ddot{p} \quad (5.13)$$

with boundary conditions

$$\left. \frac{\partial p}{\partial n} \right|_{S \cap S_u} = \nabla p \cdot n = -\rho \frac{\partial^2 u_n}{\partial t^2} \quad p|_{S \cap S_p} = \bar{p} \quad (5.13a)$$

Here p is the pressure, ρ_0 is the density of the fluid, c is the sound speed in the fluid and $s = \frac{(\rho - \rho_0)}{\rho_0}$ is the condensation. In the boundary conditions S_u is the part of the boundary to which the known normal velocity \bar{u}_n is applied and S_p is the part of the boundary to which the known pressure \bar{p} is applied. This equation models a physical environment accurately when the following assumptions are true:

- 1) Density ρ varies only by a small amount throughout the volume of interest.
- 2) Velocities are small enough that viscous effects may be omitted.
- 3) Viscous effects that give rise to deviatoric stress can be neglected.

$$\int_V \left(\delta p \nabla^2 p - \delta p \frac{1}{c^2} \ddot{p} \right) dV = 0 \quad (5.14)$$

To develop the stiffness matrices for the air in the cavity, rather than develop expressions analogous to the strain and kinetic energies as we did for the structural part of the problem, we will apply the principle of virtual work to the equilibrium equation. Equation 5.13 is multiplied by an arbitrary virtual pressure δp and then integrated over the volume of interest:

$$\int_V \left(\delta p \nabla^2 p - \delta p \frac{1}{c^2} \ddot{p} \right) dV = 0 \quad (5.14)$$

Noting that

$$\nabla \cdot (\delta p \nabla p) = \nabla \delta p + \nabla \cdot \nabla p$$

and also recalling the divergence theorem

$$\int_V \nabla \cdot \Xi dV = \int_A \Xi \cdot n dA$$

we can write

$$\int_V \left(\nabla \cdot (\delta p \nabla p) - \nabla \delta p \cdot \nabla p - \delta p \frac{1}{c^2} \ddot{p} \right) dV = \int_S \delta p \nabla p \cdot n dS - \int_V \left(\nabla \delta p \cdot \nabla p + \delta p \frac{1}{c^2} \ddot{p} \right) dV$$

When we incorporate the velocity boundary condition from 5.13a we have the final integral formulation of the equilibrium equation

$$\int_S \delta p (-\rho) \bar{u}_n dS - \int_V \left(\nabla \delta p \cdot \nabla p + \delta p \frac{1}{c^2} \ddot{p} \right) dV = 0 \quad (5.15)$$

In this investigation the transverse velocity of the plate is the velocity normal to the fluid volume. That is, $\bar{u}_n = \dot{w}$.

5.6 Acoustic Cavity Discretization

Recognizing p as a scalar entity, and defining the Laplacian, fluid displacement, and fluid shape function vectors as

$$\nabla = \left[\frac{\partial}{\partial x} \quad \frac{\partial}{\partial y} \quad \frac{\partial}{\partial z} \right]^T \quad a_f = [p_1 \ p_2 \ \dots \ p_8] \quad N_f = [N_{f1} \ N_{f2} \ \dots \ N_{f8}]$$

for an eight-node solid element, we can approximate the scalar field $p(x, y, z, t)$ and its virtual counterpart δp as

$$p \approx N_f a_f \quad \delta p \approx N_f \delta a_f$$

Then we can rewrite the terms in equation 5.15 as

$$\begin{aligned} \int_A \delta p \bar{u}_n dS &\approx \int_A \delta a_f^T N_f^T N \dot{a} dA = \delta a_f^T Q \dot{a} & Q &= \int_A N_f^T N dA \\ \int_V \nabla \delta p \cdot \nabla p dV &\approx \int_V \delta a_f^T \nabla N_f^T \nabla N a dV = \delta a_f^T K_f a & K_f &= \int_V \nabla_f^T N_f^T \nabla N dV \\ \int_V \delta p \frac{1}{c^2} \ddot{p} dV &\approx \int_V \delta a_f^T N_f^T \frac{1}{c^2} N \ddot{a} dV = \delta a_f^T M_f \ddot{a} & M_f &= \int_V N_f^T \frac{1}{c^2} N dV \end{aligned}$$

so the discretized form of equation 5.15 is

$$\delta a_f^T K_f a_f + \delta a_f^T M_f \ddot{a}_f + \delta a_f^T \rho Q \dot{a} + Work = 0$$

and finally, since δp is an arbitrary function, we have

$$K_f a_f + M_f \ddot{a}_f + \rho Q \dot{a} + Work = 0 \quad (5.16)$$

5.7 Fluid -Structure Coupling

Coupling between the fluid and the plate occurs through the boundary conditions in equations 5.11 and 5.16. From the structural equation, coupling terms are added to the global stiffness matrix at the interface pressure degrees of freedom and from the fluid equation coupling terms are added to the global mass matrix at the degrees of freedom for acceleration normal to the plate fluid interface. This can be expressed in a matrix equation as

$$\begin{bmatrix} M & 0 \\ -\rho Q & M_f \end{bmatrix} \begin{bmatrix} \ddot{a} \\ \ddot{a}_f \end{bmatrix} + \begin{bmatrix} K & Q^T \\ 0 & K_f \end{bmatrix} \begin{bmatrix} a \\ a_f \end{bmatrix} = \begin{bmatrix} F \\ F_f \end{bmatrix} \quad (5.17)$$

5.8 Finite Element Model for Combined Three Layer Plate Element

To develop a single element that will model the behavior of the base plate, viscoelastic layer and constraining layer together, we will combine the strain energies from each layer together in a single expression. To do this we must first develop expressions for the displacements in each layer.

5.9 Kinematics for Three Layer Plate

The kinematics of this model are developed using the assumptions of the Reissner-Mindlin plate theory. Specifically of use are the assumptions that 1) only small displacements occur within the plate and 2) plane sections in the undeformed plate remain plane upon deformation.

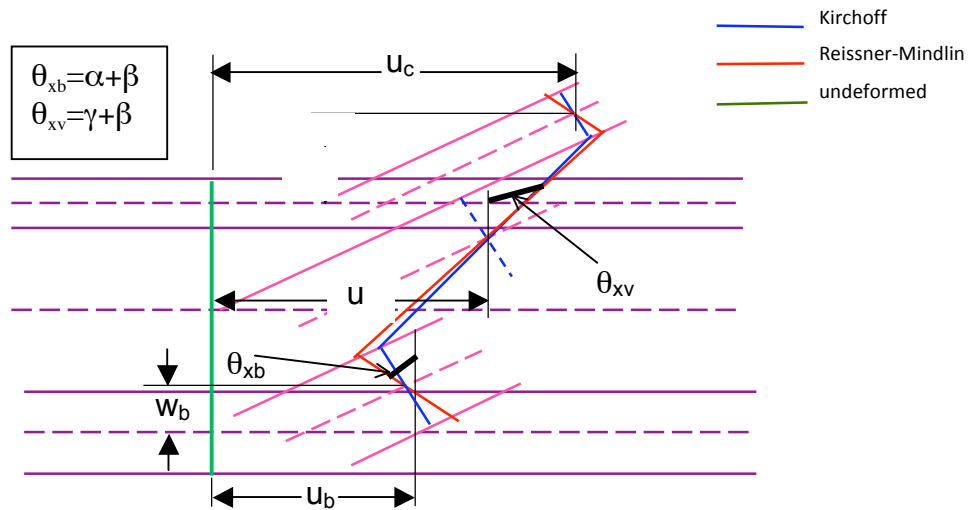


Figure 5.3: Geometry for kinematics of three layer plate

Figure 5.3 depicts the geometry involved in developing expressions for the kinematics of the three layer plate. The overall thickness of the three layers is small (0.071 in.) compared to the three layer plate length (6 in.) so the transverse displacement w is taken to be uniform throughout the three layers. As the base plate and constraining layers are both formed of the same material and are thin, the rotation of the constraining layer is taken to be the same as that in the base plate ($\theta_{cl} = \theta_b$). The viscoelastic layer is taken to have an independent rotation θ_v . These assumptions are used with the Reissner-Mindlin assumptions and trigonometric identities to generate expressions for the

extensional displacement in the viscoelastic layer and the constraining layer. Figure 5.4 illustrates the pertinent angles in the viscoelastic layer.

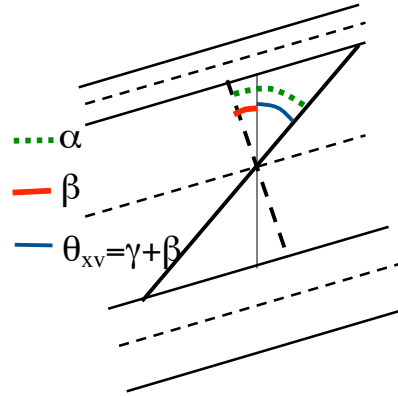


Figure 5. 4: Angles for extensions in viscoelastic and constraining layers

Also, α is the angle between the cross section normal to the mid-plane of the deformed plate and the deformed cross section using Reissner-Mindlin assumptions. It is the transverse shear angle. β is the angle between the cross section that is normal to the undeformed mid-plane and the cross section that is normal to the deformed mid-plane - this is the bending angle and is the rotation used in Kirchoff models. For small deformations $\beta = dw/dx$. The last angle, which is the rotation used in the Reissner-Mindlin models, is θ , the angle between the undeformed cross section and the deformed cross section. θ is the sum of α and β . Breaking the rotation angle into two parts makes it possible to differentiate between the case where the three layer element is made up of a base layer with $h_c = t_b$, a viscoelastic layer with $h_v = t_v$, and a constraining layer with $h_c = t_c$, and the case where the three layer element is made up of a base layer with $h_c = t_c + t_b$, a viscoelastic layer with $h_v = t_v$, and a constraining layer with $h_c = 0$. The bending angle β is

assumed constant through the three layers of the element layers, and the movement of the three layers is coupled.

With these angular definitions we can develop the following expressions for the extensional displacements u_v and u_{cl} at the midplanes of the viscoelastic and constraining layers.

$$\begin{aligned} u_v &= -\frac{h_b}{2}(\tan \alpha_b \cos \beta + \sin \beta) + \frac{h_v}{2}(\tan \gamma \cos \beta - \sin \beta) \\ u_{cl} &= -\frac{h_b + h_{cl}}{2}(\tan \alpha_b \cos \beta + \sin \beta) + h_v(\tan \gamma \cos \beta - \sin \beta) \end{aligned} \quad (5.18)$$

These expressions may be used directly in the strains and strain energy and then integrated to generate the stiffness matrix, however the resulting expression is quite complicated and it was decided to search for a simplified version of the expressions. After some experimentation it was determined that the following approximation gave good results;

$$\begin{aligned} u_v &= u_b - \frac{h_b}{2}(\alpha + \beta) + \frac{h_v}{2}(\gamma - \beta) \\ u_{cl} &= u_b - \frac{h_b + h_{cl}}{2}(\alpha + \beta) + h_v(\gamma - \beta) \end{aligned} \quad (5.19)$$

Figure 5.4 shows plots comparing the exact and approximate expressions for some of the different combinations of bending, transverse shear and total shear angles tested. The vertical axis is the extensional displacement in either the viscoelastic layer or the constraining layer, while the horizontal axis is the total shear angle in the viscoelastic layer.

Viscoelastic Layer Displacement

Constraining Layer Displacement

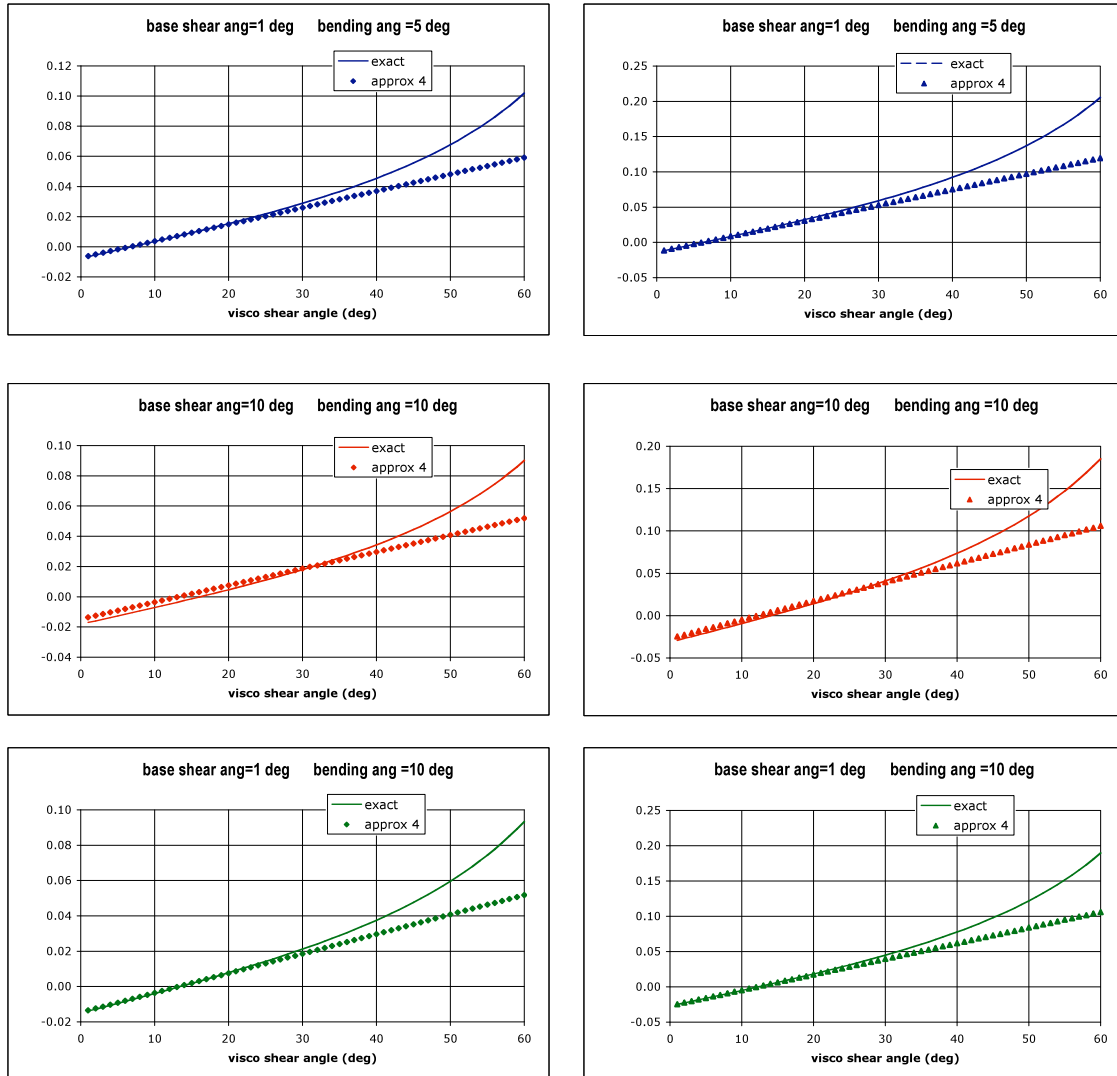


Figure 5.5: Model for the extensional displacements in the viscoelastic and constraining layers – exact expression and approximation

For these plots, the thicknesses of the materials used in the preliminary experiment were used in the calculation

As can be seen in the top two plots of Figure 5.4 the approximation performs well up to a shear angle in the viscoelastic layer of about 30 degrees when the bending angle is 5 degrees and the base plate shear angle is 1 degree. The second row of plots shows the results when the bending angle is increased to 10 degrees. Again the agreement is very

good up to a shear angle of about 30 degrees. In the third row of plots, the base shear angle was increased to an unrealistically high value of 10 degrees. Although the agreement between the exact expression and the approximation has degraded somewhat, the approximation is still fairly close to the exact expression and appears to be adequate for modeling the extensional displacements of the viscoelastic and constraining layer for this experiment.

Given these expressions for the mid-plane extensions, the displacements for the three layer element are written:

$$\begin{aligned}
 \tilde{u}_b &\approx u_b - z(\alpha_x + \beta_x) & \tilde{u}_b &= \tilde{u}_b(u_b, \alpha_{xb}, \beta_x) \\
 \tilde{u}_v &\approx u_b - \frac{h_b}{2}(\alpha_x + \beta_x) - \frac{h_v}{2}(\gamma_x + \beta_x) + z(\alpha_x + \beta_x) & \tilde{u}_v &= \tilde{u}_v(u_b, \alpha_x, \beta_x, \gamma_x) \\
 \tilde{u}_{cl} &\approx u_b - \frac{h_b + h_c}{2}(\alpha_x + \beta_x) - h_v(\gamma_x + \beta_x) - z(\alpha_x + \beta_x) & \tilde{u}_{cl} &= \tilde{u}_{cl}(u_b, \alpha_x, \beta_x, \gamma_x)
 \end{aligned} \tag{5.20a}$$

Similarly, for the y direction we have

$$\begin{aligned}
 \tilde{v}_b &\approx v_b - z(\alpha_y + \beta_y) & \tilde{v}_b &= \tilde{v}_b(v_b, \alpha_{yb}, \beta_y) \\
 \tilde{v}_v &\approx v_b - \frac{h_b}{2}(\alpha_y + \beta_y) - \frac{h_v}{2}(\gamma_y + \beta_y) + z(\alpha_y + \beta_y) & \tilde{v}_v &= \tilde{v}_v(v_b, \alpha_y, \beta_y, \gamma_y) \\
 \tilde{v}_{cl} &\approx v_b - \frac{h_b + h_c}{2}(\alpha_y + \beta_y) - h_v(\gamma_y + \beta_y) - z(\alpha_y + \beta_y) & \tilde{v}_{cl} &= \tilde{v}_{cl}(v_b, \alpha_y, \beta_y, \gamma_y)
 \end{aligned} \tag{5.20b}$$

and finally, in the z direction

$$w_b = w_v = w_{cl} = w \tag{5.20c}$$

5.10 Finite Element Model for Three Layer Plate – Strain Energy

The corresponding strains for the displacements developed in the last section are given as

Normal Strains

$$\varepsilon_{xxb} = \frac{\partial u_b}{\partial x} - z \left(\frac{\partial \alpha_x}{\partial x} + \frac{\partial \beta_x}{\partial x} \right) \quad (5.21a)$$

$$\varepsilon_{yyb} = \frac{\partial v_b}{\partial y} - z \left(\frac{\partial \alpha_y}{\partial y} + \frac{\partial \beta_y}{\partial y} \right)$$

$$\varepsilon_{xxv} = \frac{\partial u_b}{\partial x} - \frac{h_b}{2} \left(\frac{\partial \alpha_x}{\partial x} + \frac{\partial \beta_x}{\partial x} \right) - \frac{h_v}{2} \left(\frac{\partial \gamma_x}{\partial x} + \frac{\partial \beta_x}{\partial x} \right) - z \left(\frac{\partial \alpha_x}{\partial x} + \frac{\partial \beta_x}{\partial x} \right)$$

$$\varepsilon_{yyv} = \frac{\partial v_b}{\partial y} - \frac{h_b}{2} \left(\frac{\partial \alpha_y}{\partial y} + \frac{\partial \beta_y}{\partial y} \right) - \frac{h_v}{2} \left(\frac{\partial \gamma_y}{\partial y} + \frac{\partial \beta_y}{\partial y} \right) - z \left(\frac{\partial \alpha_y}{\partial y} + \frac{\partial \beta_y}{\partial y} \right)$$

$$\varepsilon_{xxcl} = \frac{\partial u_b}{\partial y} - \left(\frac{h_b + h_{cl}}{2} \right) \left(\frac{\partial \alpha_x}{\partial x} + \frac{\partial \beta_x}{\partial x} \right) - h_v \left(\frac{\partial \gamma_x}{\partial x} + \frac{\partial \beta_x}{\partial x} \right) - z \left(\frac{\partial \alpha_x}{\partial x} + \frac{\partial \beta_x}{\partial x} \right)$$

$$\varepsilon_{yycl} = \frac{\partial v_b}{\partial y} - \left(\frac{h_b + h_{cl}}{2} \right) \left(\frac{\partial \alpha_y}{\partial y} + \frac{\partial \beta_y}{\partial y} \right) - h_v \left(\frac{\partial \gamma_y}{\partial y} + \frac{\partial \beta_y}{\partial y} \right) - z \left(\frac{\partial \alpha_y}{\partial y} + \frac{\partial \beta_y}{\partial y} \right)$$

$$\varepsilon_{zzb} = \varepsilon_{zzv} = \varepsilon_{zzcl} = 0$$

Shear Strains

$$\gamma_{xyb} = \frac{\partial v_b}{\partial x} + \frac{\partial u_b}{\partial y} - z \left(\frac{\partial \alpha_x}{\partial y} + \frac{\partial \beta_x}{\partial y} + \frac{\partial \alpha_y}{\partial x} + \frac{\partial \beta_y}{\partial x} \right) \quad (5.21b)$$

$$\gamma_{xyv} = \frac{\partial v_b}{\partial x} + \frac{\partial u_b}{\partial y} - \left(\frac{h_b}{2} + z \right) \left(\frac{\partial \alpha_x}{\partial y} + \frac{\partial \beta_x}{\partial y} + \frac{\partial \alpha_y}{\partial x} + \frac{\partial \beta_y}{\partial x} \right) + \left(\frac{h_v}{2} \right) \left(\frac{\partial \gamma_x}{\partial y} + \frac{\partial \beta_x}{\partial y} + \frac{\partial \gamma_y}{\partial x} + \frac{\partial \beta_y}{\partial x} \right)$$

$$\gamma_{xycl} = \frac{\partial v_b}{\partial x} + \frac{\partial u_b}{\partial y} - \left(\frac{h_b + h_{cl}}{2} + z \right) \left(\frac{\partial \alpha_x}{\partial y} + \frac{\partial \beta_x}{\partial y} + \frac{\partial \alpha_y}{\partial x} + \frac{\partial \beta_y}{\partial x} \right) + h_v \left(\frac{\partial \gamma_x}{\partial y} + \frac{\partial \beta_x}{\partial y} + \frac{\partial \gamma_y}{\partial x} + \frac{\partial \beta_y}{\partial x} \right)$$

$$\gamma_{xzb} = \frac{\partial w}{\partial x} - (\alpha_x + \beta_x) = \gamma_{xzc} \quad \gamma_{yzb} = \frac{\partial w}{\partial y} - (\alpha_y + \beta_y) = \gamma_{yzc}$$

$$\gamma_{xzv} = \frac{\partial w}{\partial x} - (\gamma_x + \beta_x) \quad \gamma_{yzv} = \frac{\partial w}{\partial y} - (\gamma_y + \beta_y)$$

The stresses are still assumed to be Hookean functions of the strains, so an elasticity matrix **D**

$$D = \begin{bmatrix} \frac{E}{(1-\nu^2)} & \nu \frac{E}{(1-\nu^2)} & 0 \\ \nu \frac{E}{(1-\nu^2)} & \frac{E}{(1-\nu^2)} & 0 \\ 0 & 0 & \frac{1-\nu}{2} \frac{E}{(1-\nu^2)} \end{bmatrix} \quad \text{or} \quad D = \begin{bmatrix} \frac{1-\nu}{2} \frac{E}{(1-\nu^2)} & 0 \\ 0 & \frac{1-\nu}{2} \frac{E}{(1-\nu^2)} \end{bmatrix}$$

extension and bending *transverse shear*

that delineates the stress strain relationship can be used with equations 5.21 to express the stress in the three layer element. Note, however, that the moduli in the viscoelastic layer will be dependent on the spatial variables. Furthermore, the Young's modulus, shear modulus and loss factor are frequency dependent for the viscoelastic layer.

Energy dissipation is incorporated in the finite element model by noting that when a cyclic load is applied to a viscoelastic material, there is a time lag (phase difference)

between the stress and the resulting strain. Thus, the elastic moduli may be expressed in complex notation. For example, Young's modulus is written in complex form as

$$E^* = E' + iE'' \quad (5.22)$$

or

$$E^* = E' (1 + i\eta) \quad \eta = \tan\left(\frac{E''}{E'}\right)$$

Here E' is the elastic or storage modulus and is the component of stress that is in phase with the strain and is a measure of the energy that cycles between being stored and then regained in the system. E'' is the loss modulus and is a measure of the energy that is dissipated in heat from the system. Fully elastic systems have a loss modulus of zero.

The strain energy is, as usual, the integrated sum of the product of the stress and strains

$$U = \frac{1}{2} \int_A \sigma_{xx} \varepsilon_{xx} + \sigma_{yy} \varepsilon_{yy} + \gamma_{xy} \varepsilon_{xy} + \gamma_{xz} \varepsilon_{xz} + \gamma_{yz} \varepsilon_{yz} dA$$

However, now the stresses and strains are sums of the contributions from the three layers

$$\begin{aligned} \varepsilon_{xx} &= \varepsilon_{xxb} + \varepsilon_{xxv} + \varepsilon_{xxcl} & \varepsilon_{yy} &= \varepsilon_{yyb} + \varepsilon_{yyv} + \varepsilon_{yycl} & \dots \\ \sigma_{xx} &= C_{xx} \varepsilon_{xx} & \sigma_{yy} &= C_{yy} \varepsilon_{yy} & \dots \end{aligned}$$

The virtual work equation for the element can be expressed in matrix form as

$$\begin{aligned}
\int_V \delta \varepsilon^T \sigma dV = & \int_A \int_{-h_b/2}^{h_b/2} [\delta \varepsilon_b^{LS}]^T [\sigma_b^{LS}] dz dA + \int_A \int_{-h_b/2}^{h_b/2} [\delta \varepsilon_b^B]^T [\sigma_b^B] dz dA + \int_A \int_{-h_b/2}^{h_b/2} [\delta \varepsilon_b^{TS}]^T [\sigma_b^{TS}] dz dA + \\
& \int_A \int_{-h_v/2}^{h_v/2} [\delta \varepsilon_v^{LS}]^T [\sigma_v^{LS}] dz dA + \int_A \int_{-h_v/2}^{h_v/2} [\delta \varepsilon_v^B]^T [\sigma_v^B] dz dA + \int_A \int_{-h_v/2}^{h_v/2} [\delta \varepsilon_v^{TS}]^T [\sigma_v^{TS}] dz dA + \\
& \int_A \int_{-h_c/2}^{h_c/2} [\delta \varepsilon_c^{LS}]^T [\sigma_c^{LS}] dz dA + \int_A \int_{-h_c/2}^{h_c/2} [\delta \varepsilon_c^B]^T [\sigma_c^B] dz dA + \int_A \int_{-h_c/2}^{h_c/2} [\delta \varepsilon_c^{TS}]^T [\sigma_c^{TS}] dz dA + \\
& + \text{KineticEnergy} + \text{BoundaryTerms} + \text{Work} = 0 \quad (5.22)
\end{aligned}$$

5.11 Discretization for Three Layer Element

We define the vectors containing the displacements of a 4 node, three layer plate

$$\begin{aligned}
a_{LS} &= [u_1 v_1 \alpha_{x1} \alpha_{y1} \beta_{x1} \beta_{y1} \gamma_{x1} \gamma_{y1} u_2 v_2 \alpha_{x2} \alpha_{y2} \beta_{x2} \beta_{y2} \gamma_{x2} \gamma_{y2} u_3 v_3 \alpha_{x3} \alpha_{y3} \beta_{x3} \beta_{y3} \gamma_{x3} \gamma_{y3} u_4 v_4 \alpha_{x4} \alpha_{y4} \beta_{x4} \beta_{y4} \gamma_{x4} \gamma_{y4}]^T \\
a_B &= [\alpha_{x1} \alpha_{y1} \beta_{x1} \beta_{y1} \gamma_{x1} \gamma_{y1} \alpha_{x2} \alpha_{y2} \beta_{x2} \beta_{y2} \gamma_{x2} \gamma_{y2} \alpha_{x3} \alpha_{y3} \beta_{x3} \beta_{y3} \gamma_{x3} \gamma_{y3} \alpha_{x4} \alpha_{y4} \beta_{x4} \beta_{y4} \gamma_{x4} \gamma_{y4}]^T \\
a_{TS} &= [w_1 \alpha_{x1} \alpha_{y1} \beta_{x1} \beta_{y1} \gamma_{x1} \gamma_{y1} w_2 \alpha_{x2} \alpha_{y2} \beta_{x2} \beta_{y2} \gamma_{x2} \gamma_{y2} w_3 \alpha_{x3} \alpha_{y3} \beta_{x3} \beta_{y3} \gamma_{x3} \gamma_{y3} w_4 \alpha_{x4} \alpha_{y4} \beta_{x4} \beta_{y4} \gamma_{x4} \gamma_{y4}]^T
\end{aligned}$$

element as follows:

The coupling introduced by the kinematic model is evident in the large number of DOF now required for the longitudinal strain.

Then, as was done for the plain plate element, we use the derivatives from 5.4 and discretized expression of the independent variables and global coordinates from equation 5.3 in the strain expressions of 5.21 (along with the additional discretized variable γ). The strains (and virtual strains) can be written in matrix form as was done in equation 5.6, the appropriate stresses generated and then these expressions are substituted into the virtual work equation 5.22.

Writing all the degrees of freedom together in a single vector $\{a\}$ of element displacements we can rewrite equation 5.22 as

$$\begin{aligned} \{\delta a\}^T [K_{LS_3} + K_{B_3} + K_{TS_3}] \{a\} + K.E. + Work &= 0 \\ \text{or} \quad \{\delta a\}^T [K_{el_3}] \{a\} + K.E. + Work &= 0 \end{aligned} \quad (5.23)$$

$$a = [u_1 v_1 w_1 \alpha_{x1} \beta_{x1} \gamma_{x1} u_2 v_2 w_2 \alpha_{x2} \beta_{x2} \gamma_{x2} u_3 v_3 w_3 \alpha_{x3} \beta_{x3} \gamma_{x3} u_4 v_4 w_4 \alpha_{x4} \beta_{x4} \gamma_{x4}]$$

where

and K_{el_3} is the element stiffness matrix for the three layer element.

5.12 Finite Element Model for Three Layer Plate – Kinetic Energy

For the three layer element, the kinetic energy may be expressed as the sum of the kinetic energy in the base plate (discussed above), the kinetic energy in the viscoelastic layer and the kinetic energy in the constraining layer. Using the kinematic definitions for the viscoelastic and constraining layer variables discussed above, the kinetic energy in the viscoelastic layer is

$$\begin{aligned} T_{visco} &= \frac{1}{2} \int_V \rho_v (\dot{u}_v^2 + \dot{v}_v^2 + \dot{w}_v^2) dV \\ &= \frac{1}{2} \rho_v \int_V \left(\left[\dot{u}_b - \frac{h_b}{2} (\dot{\alpha}_x + \dot{\beta}_x) - \frac{h_v}{2} (\dot{\gamma}_x + \dot{\beta}_x) - z (\dot{\alpha}_x + \dot{\beta}_x) \right]^2 \right. \\ &\quad \left. + \left[\dot{v}_b - \frac{h_b}{2} (\dot{\alpha}_y + \dot{\beta}_y) - \frac{h_v}{2} (\dot{\gamma}_y + \dot{\beta}_y) - z (\dot{\alpha}_y + \dot{\beta}_y) \right]^2 + \dot{w}_b^2 \right) dV \end{aligned} \quad (5.24)$$

After Equation 5.24 is integrated over the thickness and simplified, it is substituted into Lagrange's equation to be used in developing an expression of virtual work.

This can be written as

$$\text{Strain Energy} + \text{Kinetic Energy Base} + \text{Kinetic Energy Constraining Layer} \quad (5.25)$$

$$+ \int_A \left(\delta u c_{v1} \ddot{u} + \delta v c_{v1} \ddot{v} + \delta w c_{v5} \ddot{w} + \delta \alpha_x c_{v2} \ddot{\alpha}_x + \delta \alpha_y c_{v2} \ddot{\alpha}_y \right. \\ \left. + \delta \beta_x c_{v3} \ddot{\beta}_x + \delta \beta_y c_{v3} \ddot{\beta}_y + \delta \gamma_x c_{v4} \ddot{\gamma}_x + \delta \gamma_y c_{v4} \ddot{\gamma}_y \right) dA + \text{Work} = 0$$

where

$$c_{v1} = \rho_v h_v (1 - h_b - h_v) \\ c_{v2} = \rho_v h_v \left(\frac{h_b^2 - h_b - h_b h_v}{2} \right) \\ c_{v3} = \rho_v h_v \left(\frac{3h_b^2 + 5h_v^2 - 2(h_b + h_v) + 7h_b h_v}{8} \right) \\ c_{v4} = \rho_v h_v \left(\frac{10h_v^2 - 6h_v - 9h_b h_v}{12} \right) \\ c_{v5} = \rho_v h_v$$

The analogous expression for the constraining layer can be obtained through the same process:

$$\text{Strain Energy} + \text{Kinetic Energy Base} + \text{Kinetic Energy Viscoelastic Layer} \quad (5.26)$$

$$+ \int_A \left(\delta u c_{c1} \ddot{u} + \delta v c_{c1} \ddot{v} + \delta w c_{c5} \ddot{w} + \delta \alpha_x c_{c2} \ddot{\alpha}_x + \delta \alpha_y c_{c2} \ddot{\alpha}_y \right) \\ \left(+ \delta \beta_x c_{c3} \ddot{\beta}_x + \delta \beta_y c_{c3} \ddot{\beta}_y + \delta \gamma_x c_{c4} \ddot{\gamma}_x + \delta \gamma_y c_{c4} \ddot{\gamma}_y \right) dA + \text{Work} = 0$$

Where

$$\begin{aligned}
 c_{c1} &= \rho_v h_v \left(1 - \frac{3h_v}{2} - (h_b + h_c) \right) \\
 c_{c2} &= \rho_v h_v \left(\frac{h_c^2}{6} + \frac{(h_b + h_c)^2}{2} + h_v (h_b + h_c) - \frac{(h_b + h_c)}{2} \right) \\
 c_{c3} &= \rho_v h_v \left(\frac{h_c^2}{6} + \frac{(h_b + h_c)^2}{2} + 2h_v (h_b + h_c) - \frac{(h_b + h_c)}{2} + 2h_v^2 - \frac{(h_b + h_c + h_v)}{2} \right) \\
 c_{c4} &= \rho_v h_v \left(\frac{3h_v^2}{2} + h_v (h_b + h_c) - \frac{(h_b + h_c)}{2} - h_v^2 \right) \\
 c_{c5} &= \rho_c h_c
 \end{aligned}$$

As was done in the case of a plain plate element, a matrix form of 5.26 is generated analogous to Equation 5.10 and an appropriate mass matrix is formed that models the effects of the viscoelastic and constraining layer mass on the system energy. This mass matrix takes into account the coupling between the displacements, both bending and extensional, in the three layers.

5.13 Summary

This chapter presents the development for the different elements in the finite element model of the viscoelastically damped plate/cavity system. *Reissner-Mindlin theory* is used to express displacements in terms of extensions and rotations. The rotational angle is broken into the shear and bending angles to facilitate the discrimination between a base plate with a viscoelastic layer of thickness h_v that is constrained and a thicker base plate with an unconstrained viscoelastic layer of thickness

h_v . Fluid-structural coupling is achieved by applying boundary conditions at the wetted nodes. Frequency dependent energy dissipation is modeled in the viscoelastic layer by applying complex moduli theory. Bilinear shape functions are used in all elements and direct integration is used to construct the stiffness and mass matrices. The mass matrix is consistent and all coupling between degrees of freedom is taken into account.

Chapter 6

Validation of Finite Element of Plate/Cavity Model

6.1 Introduction

In the interest of brevity and clarity, the finite element program developed for this study will be referred to as Mary F. Leibolt Finite Element (MFLFE). This distinguishes it from the commercial finite element code NASTRAN used in the setup stages of this investigation.

Development of the code was incremental in nature, that is, each element type was developed and validated before the development of the next element type took place. In cases where the configuration was simple enough, the correctness of the element was tested by comparing an analytical computation of eigenvalues to the eigenvalues generated by MFLFE. Otherwise, the element was validated either by comparing results to a commercially available finite element code or by comparing the experimental output pressure spectra at the location of the internal microphone (see Figure 4.1) to MFLFE's numerically generated pressure spectra for the same location. For validation by comparison with experiment, a number of experimental configurations were used to confirm that MFLFE could correctly predict the sound pressure spectra for a wide variety of material configurations. Experimental configuration variation included the use of

viscoelastic materials with different material properties, constrained and unconstrained viscoelastic layers, and multiple materials in the viscoelastic treatment.

6.2 Base Plate Element

The basic untreated plate element was simple enough that analytical eigen-frequencies could be computed to validate the correctness of the element operation. As presented in Flugge (1962) the eigen-frequencies for a clamped thin square plate can be predicted (using Kirchoff assumptions) by the equation

$$\omega = \frac{\lambda_i}{L^2} \sqrt{\frac{K}{\mu}}$$

where ω is the eigenfrequency, K is the bending stiffness, ρ is the plate's mass density, L is the length of the plate's sides and λ_i is a parameter listed in Flugge's Handbook of Engineering Mechanics (1962) that is dependent on mode number and boundary conditions. The program MFLFE solves the standard FE eigenvalue problem

$$\omega^2 [M] \mathbf{q} = [K] \mathbf{q}$$

where $[M]$ is the mass matrix, $[K]$ is the stiffness matrix and the ω are the natural frequencies of the system. The comparison of the results is shown in the table below:

METHOD	MESH	1ST EIGEN FREQ (HZ)	2ND EIGEN FREQ (HZ)	3RD EIGEN FREQ (HZ)
Thin plate theory		38.94	79.82	117.77
NASTRAN	12x12	38.87	79.16	114.96
MFLFE	12x12	38.40	80.03	119.19

Table 6.1: Comparison of analytical solution, NASTRAN and MFLFE eigenvalues for an untreated plate

The agreement is good. It appears that as NASTRAN goes up in frequency it tends to be slightly softer than the Kirchoff prediction, while MFLFE tends to be slightly stiffer than Kirchoff theory predictions.

6.3 Acoustic Element

As discussed in section 3.2, the eigenvalues of an acoustic cavity with rigid walls can be predicted using Equation 3.2

$$f = \frac{c}{2\pi} \left[\left(\frac{l\pi}{L_x} \right)^2 + \left(\frac{m\pi}{L_y} \right)^2 + \left(\frac{n\pi}{L_z} \right)^2 \right]^{\frac{1}{2}}$$

Again using the standard finite element eigenvalue solution approach, MFLFE calculated the eigenvalues for the acoustic cavity and the results for a 12x12x12 mesh of 8-noded elements (excluding the eigenvalue at zero) are listed in Table 6.2 along with the theory and the NASTRAN results for an 8 noded solid element. To increase the agreement

between the 2nd and 3rd modes of the analytical solution and MFLFE, the longitudinal mesh size was refined to be 12x12x24. These results also appear in the table.

METHOD	MESH	1ST EIGEN FREQ (HZ)	2ND EIGEN FREQ (HZ)	3RD EIGEN FREQ (HZ)	4 TH EIGEN FREQ (HZ)
Analytical		225.06	450.12	562.65	605.99
NASTRAN	12x12x12	225.70	455.29	564.27	607.35
MFLFE	12x12x12	225.71	455.29	564.27	607.74
MFLFE	12x12x24	225.23	451.42	564.27	607.56

Table 6.2: Comparison of analytical solution, NASTRAN and MFLFE eigenvalues for an acoustic cavity

6.4 Coupled Plate and Cavity

The final configuration for which eigenvalues can be calculated in MFLFE is the plain, untreated plate coupled with the acoustic cavity. An analytical prediction of eigenfrequencies for the coupled plate and cavity was not attempted. Instead, the eigenfrequencies calculated by MFLFE's were compared to those calculated for this configuration by NASTRAN. A 12x12x12 element mesh was used for the calculations. Note that the runs in NASTRAN were done using 8 noded plate elements and 20 noded acoustic elements, while MFLFE uses 4 noded plate elements and 8 noded acoustic elements. The results are presented in Table 6.3.

METHOD	1ST EIGEN FREQ (HZ)	2ND EIGEN FREQ (HZ)	3RD EIGEN FREQ (HZ)	4TH EIGEN FREQ (HZ)	5TH EIGEN FREQY (HZ)	6TH EIGEN FREQ (HZ)
NASTRAN	55.7	77.1	115.8	140.7	141.2	177.5
MFLFE	55.5	77.7	115.9	148.1	149.4	184.6

Table 6.3: Comparison of NASTRAN and MFLFE eigenvalues for a coupled plate and acoustic cavity

Sound pressure spectra were also generated for this configuration using MFLFE and compared to the experimental pressure spectra. This comparison is shown below in Figure 6.1. The agreement between the two curves is very good.

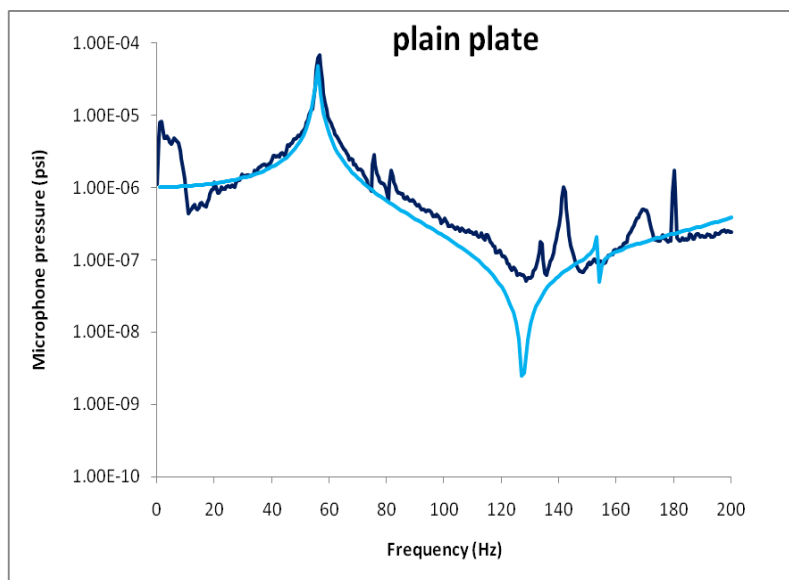


Figure 6. 1: Comparison between MFLFE numerical pressure data and preliminary experiment pressure data for an untreated plate

6.5 Three Layer Plate Element

Once correct operation of the plain plate, acoustic and coupling elements was verified, program development proceeded with the design of the treated plate element. As mentioned earlier, the rotational degrees of freedom were split into the rotation due to bending and the rotation due to shear within the material. Thin plate theory assumes that the bending angle can be considered constant through the three layers of the plate. Design of the three layer element allows the shear angle rotation to vary with material differences. Thus in the constrained layer case there is a shear angle α for the aluminum base and the aluminum constraining layer, and a second shear angle γ for the viscoelastic layer. The unconstrained case is modeled in the three layer element by allowing the thickness of the constraining layer to go to zero. Since the contributions to the mass and stiffness matrices from each layer are added in the element matrices, and since the plain plate layer is always present, this approach does not lead to singularity in the element matrices. Note that setting both the constraining layer thickness and the viscoelastic layer thickness to zero gives the same result as a plain plate element. Figure 6.2 shows a sketch of a cross section of the three cases possible in the three layer element.

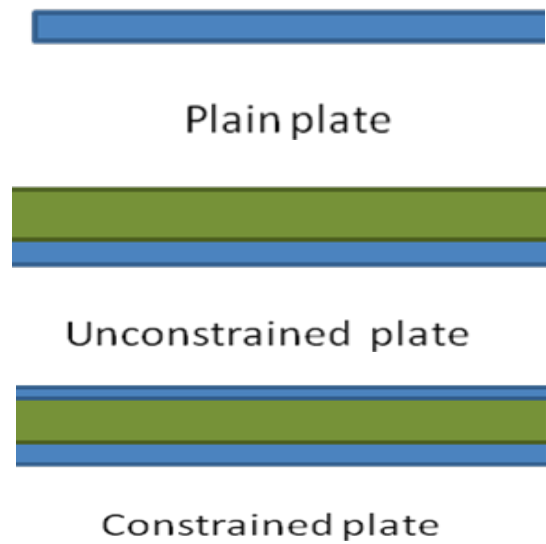
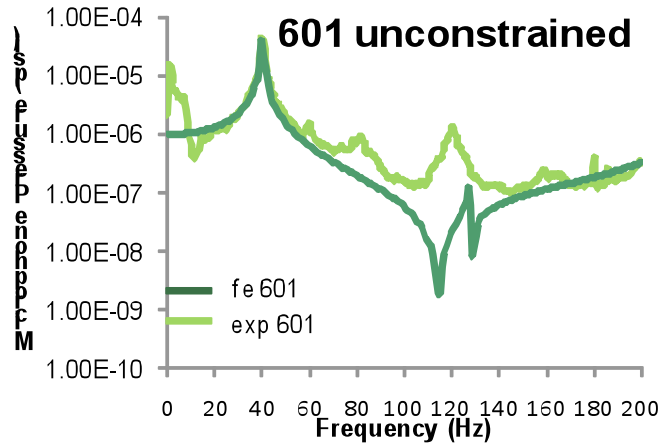
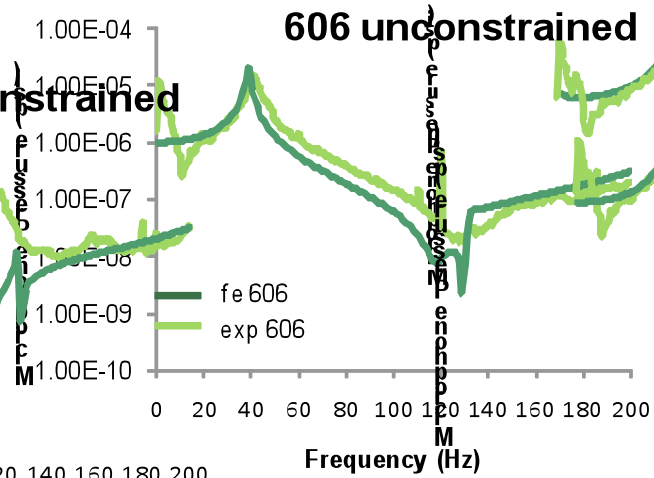


Figure 6. 2: Three possible configurations of three layer element

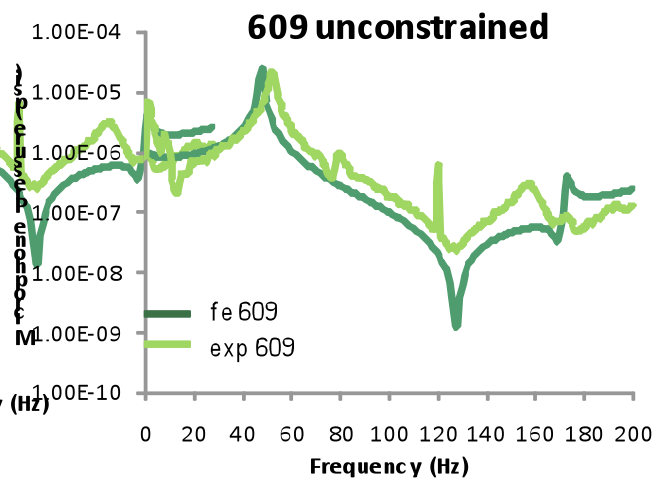
This element's correct operation was verified by comparing pressure data from the preliminary experiment described in Chapter 4 to the output of MFLFE for the same configuration. The comparison for the unconstrained case is shown in Figure 6.3. There are three graphs, one for each of the three different viscoelastic materials used in the preliminary experiment. The three materials have different Young's modulus and loss factors as a function of frequency (see Figure 4.4). Soundcoat 601 is the softest material, Soundcoat 609 is the stiffest material and Soundcoat 606 is between the two others as regards stiffness.



(a)



(b)

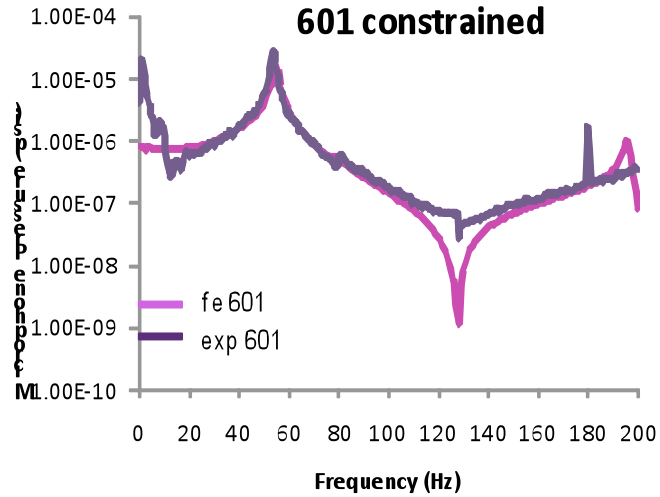


(c)

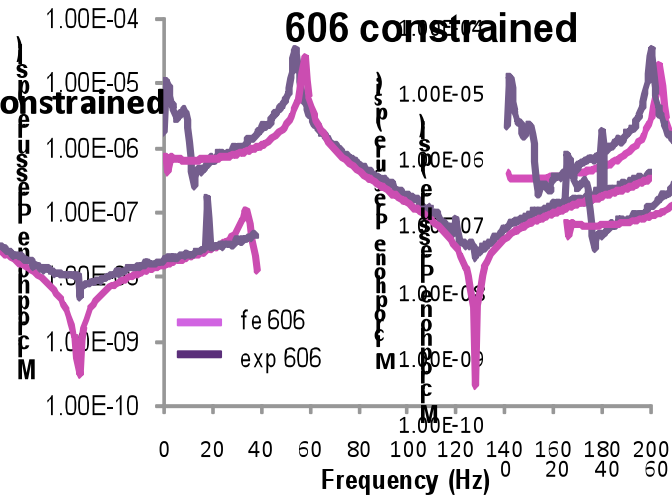
Figure 6. 3: Comparison between MFLFE numerical pressure data and preliminary experiment pressure data for a plate with an unconstrained viscoelastic layer

The MFLFE code performed reasonably well for the unconstrained case, though the comparison with experiment differed in some instances. MFLFE predicts that the frequency of the first resonance will increase with increasing stiffness as should be the case, however experimental data shows a somewhat greater shift in frequency than MFLFE predicted. The null that occurs between 100 Hz and 130 Hz which is controlled by the acoustic elements also shifts up in frequency as the stiffness of the material increases and although MFLE captures this physical phenomenon, again the agreement between frequencies of the null was slightly different. Also, MFLFE tends to underpredict the amplitude of the curve for the unconstrained configuration by 2-3 dB in much of the frequency region. Overall, the agreement between the experimental and numerical sets of data is acceptable and MFLFE captures the correct trends for the physical phenomena affecting the acoustic cavity system.

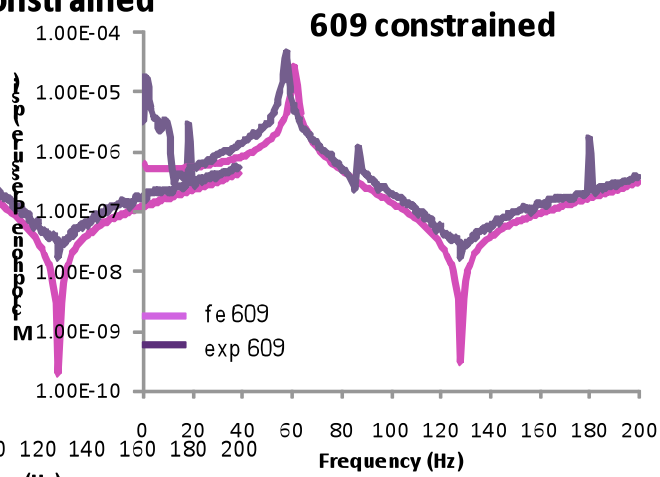
Agreement between experiment and prediction improved for the constrained case. Figure 6.4 shows the comparison between experiment and numerical data for the constrained layer single material configuration.



(a)



(b)

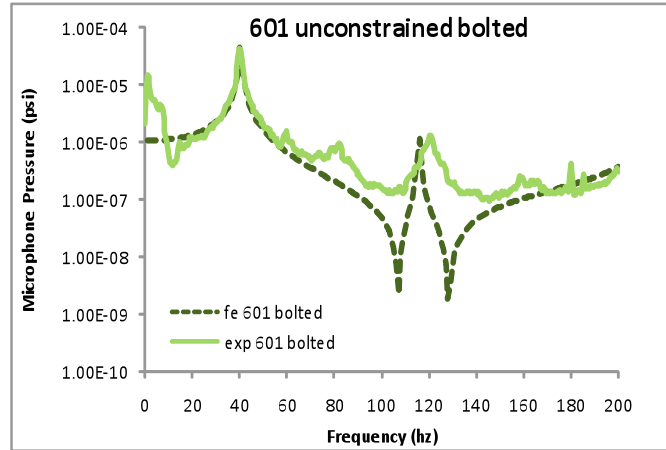


(c)

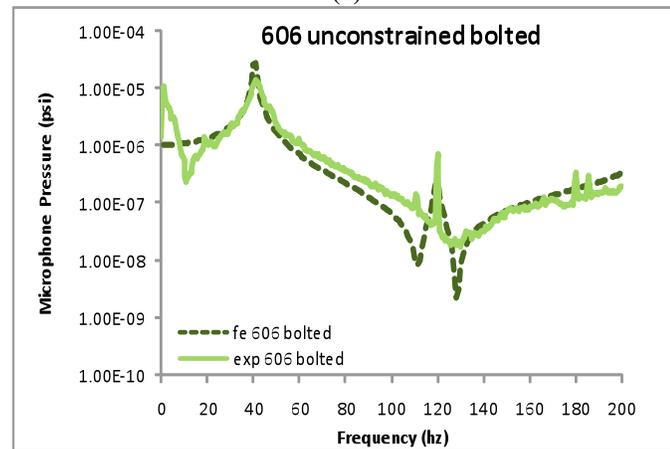
Figure 6. 4: Comparison between MFLFE numerical pressure data and preliminary experiment pressure data for a plate with a constrained single material viscoelastic layer

Although MFLFE predicted somewhat less of a frequency shift for the first resonance than that which was observed in the preliminary experiment, the amplitude of the predicted pressures matched that of the experiment well as did the frequency of the first null. Overall, the agreement between the experimental and numerical sets of data is good for the constrained layer configuration.

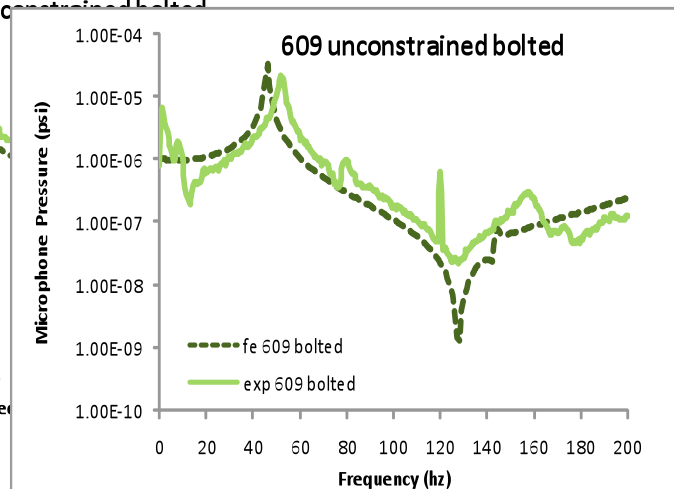
It was noted that the experimental configuration was slightly different than the numerical model in that the numerical model assumed that all points on the plate boundary were clamped to the Plexiglas cavity, that is that all degrees of freedom for the plain plate elements had a value of zero at the flexible plate's edge. In fact, in the experiment, the plate is attached to the Plexiglass cavity by 16 bolts (4 per side). To replicate this, it was decided to run the numerical model with the boundary conditions such that only the points at the bolt locations were fully clamped. The results on the pressure field in the acoustic cavity as predicted by MFLFE are illustrated in Figures 6.5 and 6.6 below. It can be seen that there is some improvement in the overall amplitude agreement between experiment and MFLFE for the unconstrained SC 606 case (Figure 6.5 upper right). Also, it appears that there is some improvement in the agreement between the frequency of the second resonance peak. Overall the comparison is not dramatically changed by bolted boundary conditions for the unconstrained configuration.



(a)

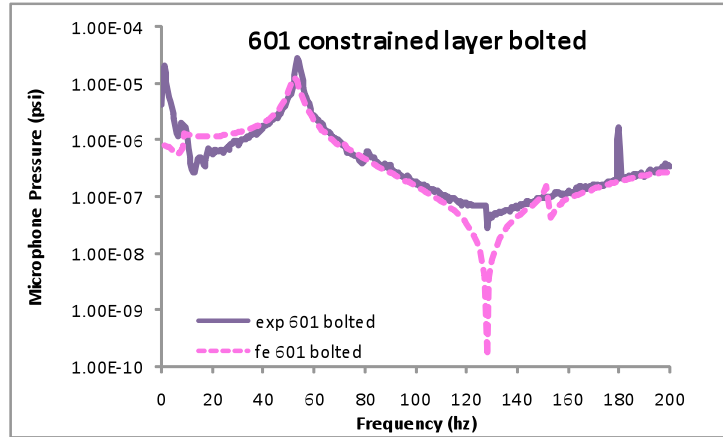


(b)

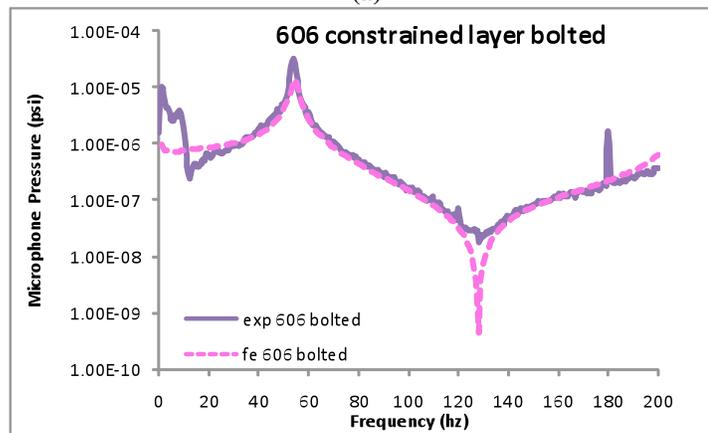


(c)

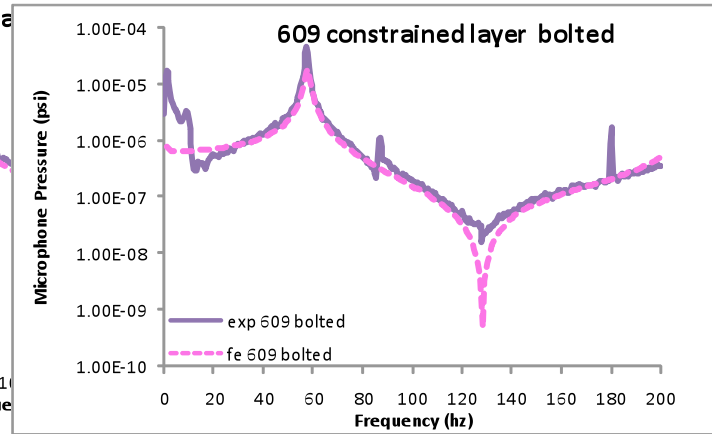
Figure 6. 5: Comparison between MFLFE numerical pressure data and preliminary experiment pressure data for a plate with an unconstrained single material viscoelastic layer. Bolted boundary conditions



(a)



(b)



(c)

Figure 6. 6: Comparison between MFLFE numerical pressure data and preliminary experiment pressure data for a plate with a constrained single material viscoelastic layer. Bolted boundary conditions

However, the bolted boundary conditions do provide better frequency agreement for the constrained case as can be seen in Figures 6.6. It was decided to use the bolted boundary conditions as the basis for modeling the experimental acoustic cavity system.

A final comparison was made between MFLFE output and experimental data for the spatially varying (mixed material) constrained layer configuration. The mixed material layout was a combination of the stiffest and softest materials laid out as shown in the bottom left hand corner of Figure 4.3. The comparison between experimental and numerical data is shown in Figure 6.5. The agreement between the two curves for the mixed material configuration is very good.

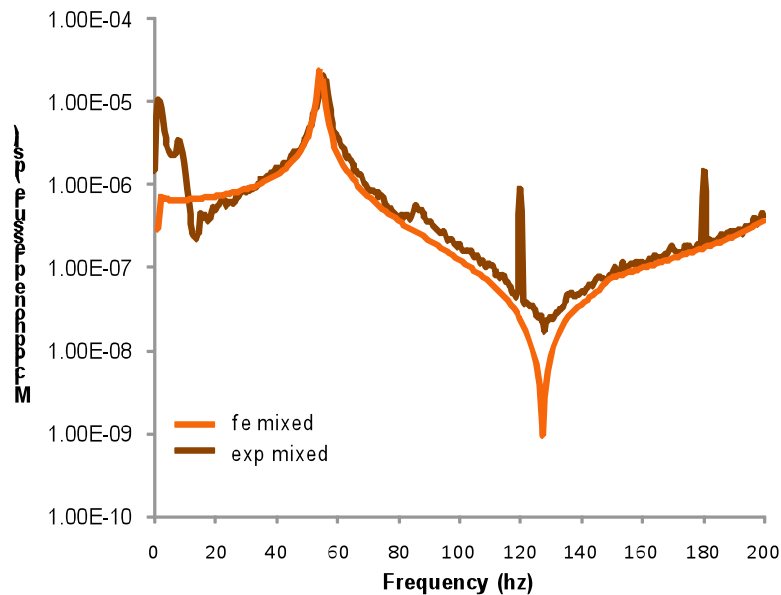
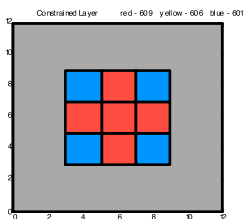


Figure 6. 7: Comparison between MFLFE numerical pressure data and preliminary experiment pressure data for a plate with a multiple material constrained viscoelastic layer

6.6 Summary

The finite element code MFLFE was validated using analytical expressions, experimental data and comparison with a commercial code. MFLFE performed well, predicting pressure data that matched the validation data well overall. The overall agreement indicates that the code is capable of modeling the underlying physical phenomena that govern the response of the acoustic cavity.

Chapter 7

Comparison of Geometric Layouts for Constrained Layer Multi-Material Treatments

7.1 Introduction

Once reasonable confidence was established that the MFLFE code was capable of modeling the experimental acoustic cavity system, a parametric study was undertaken to identify effective geometric layouts. Current features in the MFLFE program design constrain the choice of geometric layout to those that can be made of a combination of rectangular elements. It was decided to use a combination of the softest viscoelastic material (Soundcoat 601 or SC 601) and the stiffest viscoelastic material (Soundcoat 609 or SC 609) to maximize the amount of energy absorbed by shear displacement in the treatment.

7.2 Single Material Property Variation

To gain some knowledge of the magnitude of the effect that varying material properties had on the acoustic cavity system, the viscoelastic Young's Modulus, viscoelastic density and the viscoelastic loss factor were varied for single material constrained layer treatments. Presented in Figures 7.1 a-c are parametric plots for the pressures in the acoustic cavity for a plate treated with a constrained square of SC

601. Figures 7.2 a-c present the parametric plots for a plate treated with a constrained square of SC 609. In the interest of expediency, a slightly coarser grid was used in the fluid for this parametric study although the resolution for the plate elements remained the same. Because the intent in this case was to examine trends rather than absolute magnitude this strategy was acceptable.

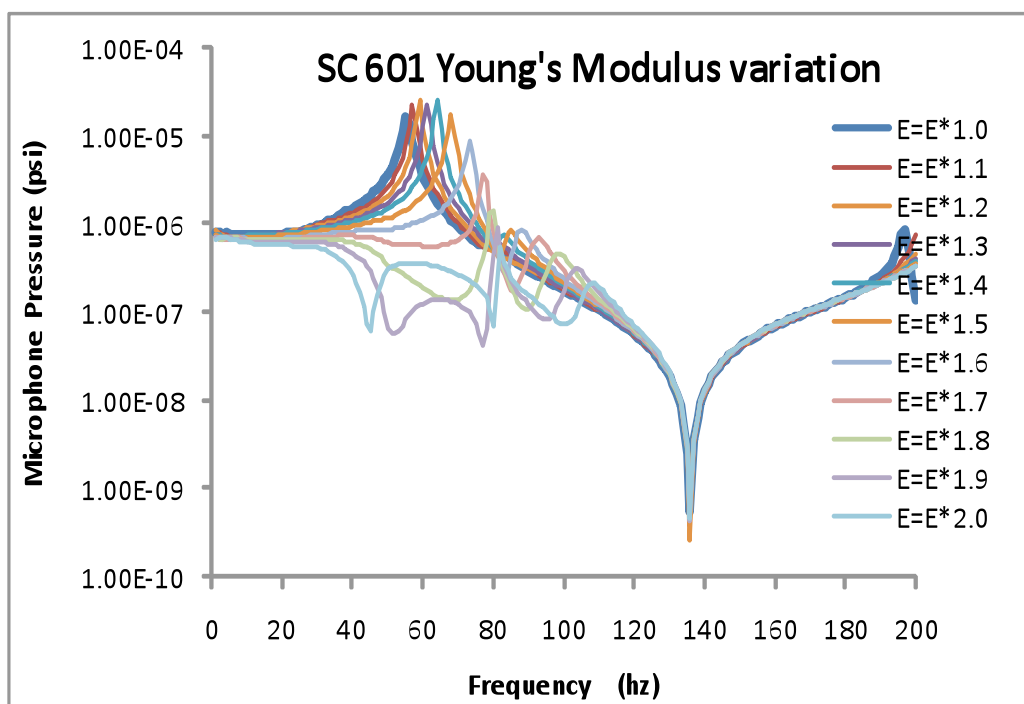


Figure 7. 1a: Pressures predicted in the acoustic cavity using MFLFE and parametric variation of Young's modulus in the viscoelastic layer for SC 601

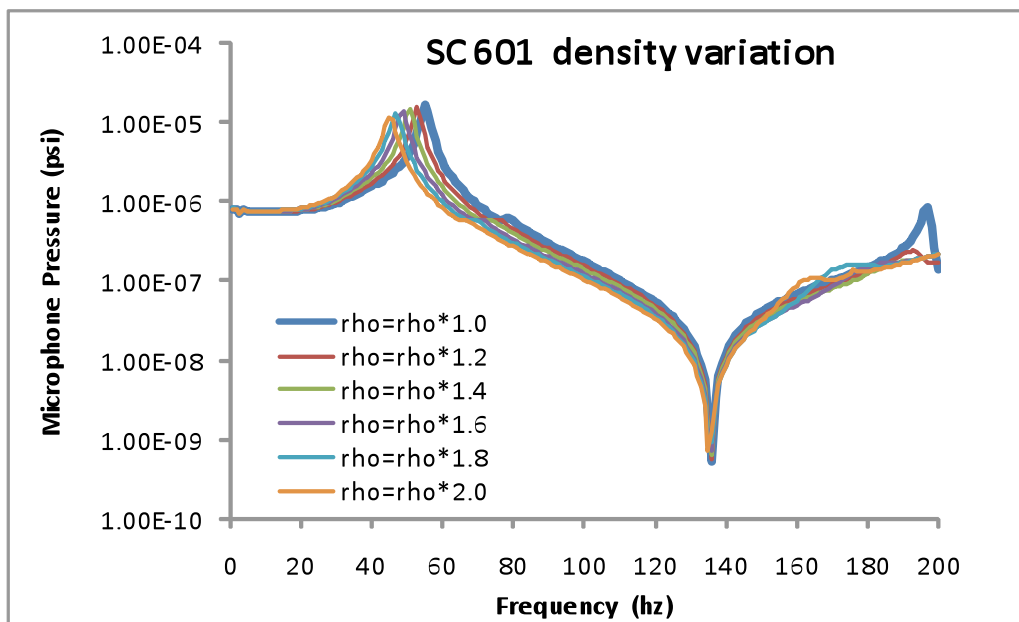


Figure 7. 1b: Pressures predicted in the acoustic cavity using MFLFE and parametric variation of the density in the viscoelastic layer for SC 601

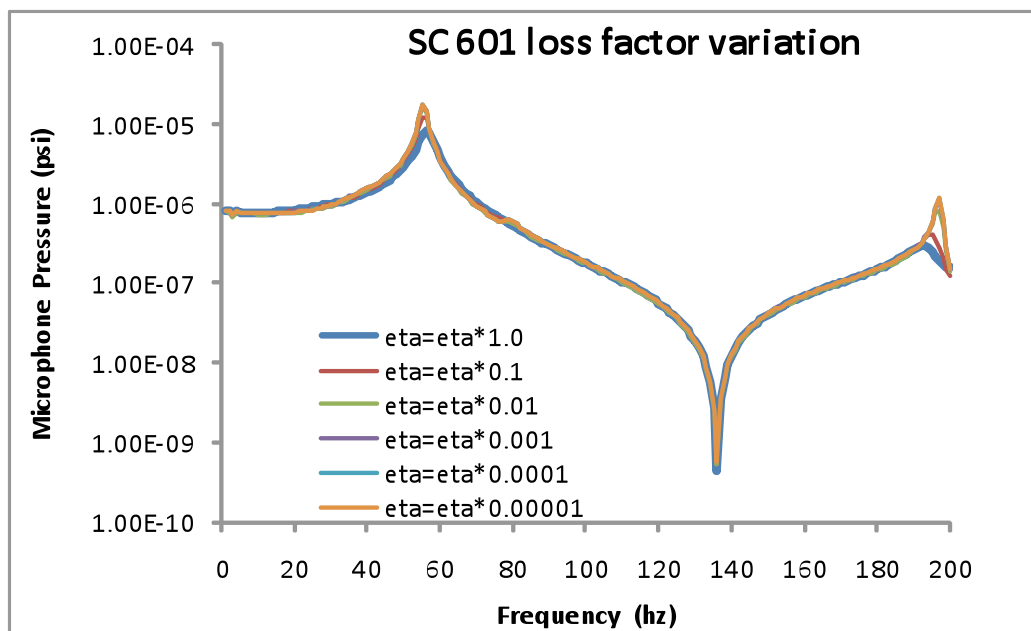


Figure 7. 1c: Pressures predicted in the acoustic cavity using MFLFE and parametric variation of the loss factor in the viscoelastic layer for SC 601

In the graphs, the prediction of pressure using the original value of the material property that was collected from manufacturer's data is shown as the heaviest line in the set of curves and the parametric variations are plotted with lighter weight lines. As can be seen in the legend of the graphs, for Young's modulus parametric variation, the value was increased in 10% increments until the value was double the original value given in the manufacturer's data sheet. The viscoelastic density was changed in increments of 20% until the value was doubled and finally, the loss factor was changed to have five orders of magnitude lower than the original value. Both Young's modulus and loss factor are functions of frequency for the viscoelastic materials.

Figure 7.1a shows the expected rise in frequency of the first resonance peak for increasing Young's modulus. It appears that for SC 601, variation in this material property has a significant effect on the acoustic cavity system. Density variation also affects the system noticeably for SC 601, driving the first resonance peak down in frequency as expected. Finally, it can be seen in Figure 7.1c that varying the loss factor affects the amplitude, not the frequency of the first resonance peak.

Considering Figure 7.2a, it can be seen that doubling the Young's modulus for SC 609 had very little effect on the acoustic cavity system. Further experimentation with varying the Young's modulus for SC 609 revealed that even changing Young's modulus by a factor of 9 only shifted the resonance from 63 Hz to 65 Hz for the constrained case. For the unconstrained case increasing the value of Young's modulus by a factor of 9 caused the first resonance from 46 Hz to 60 Hz, so it seems

likely that in the constrained case, the stiffness of the viscoelastic material is close enough to that of the constraining layer that it has reached a limiting value.

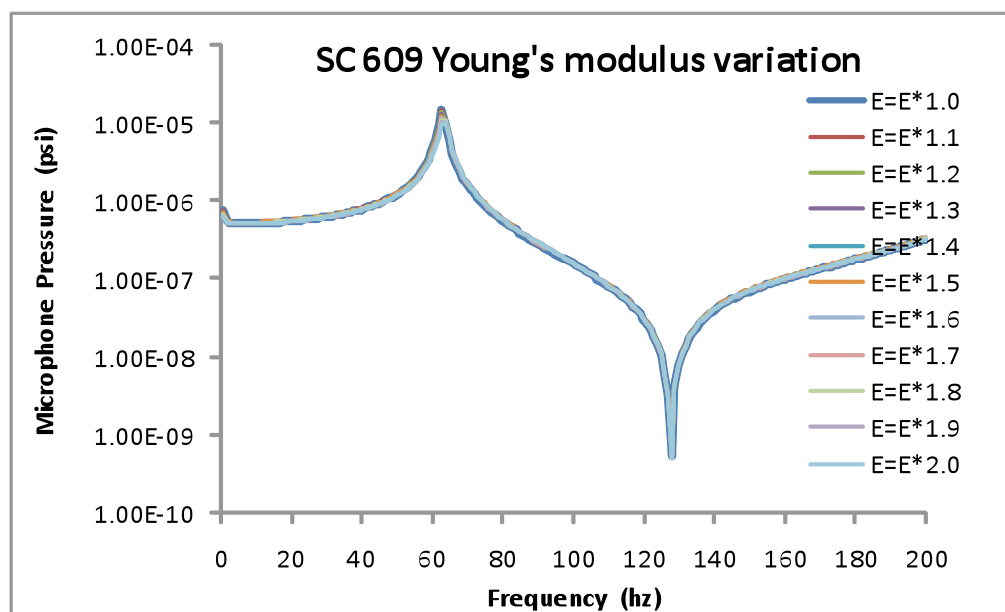


Figure 7. 2a: Pressures predicted in the acoustic cavity using MFLFE and parametric variation of the density in the viscoelastic layer for SC 609

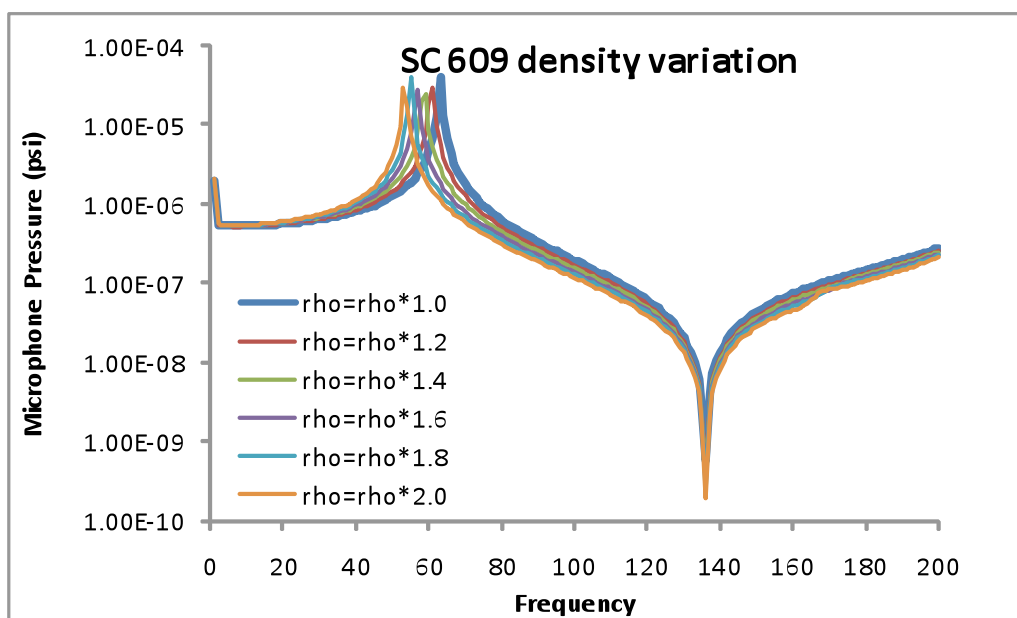


Figure 7. 2b: Pressures predicted in the acoustic cavity using MFLFE and parametric variation of Young's modulus in the viscoelastic layer for SC 609

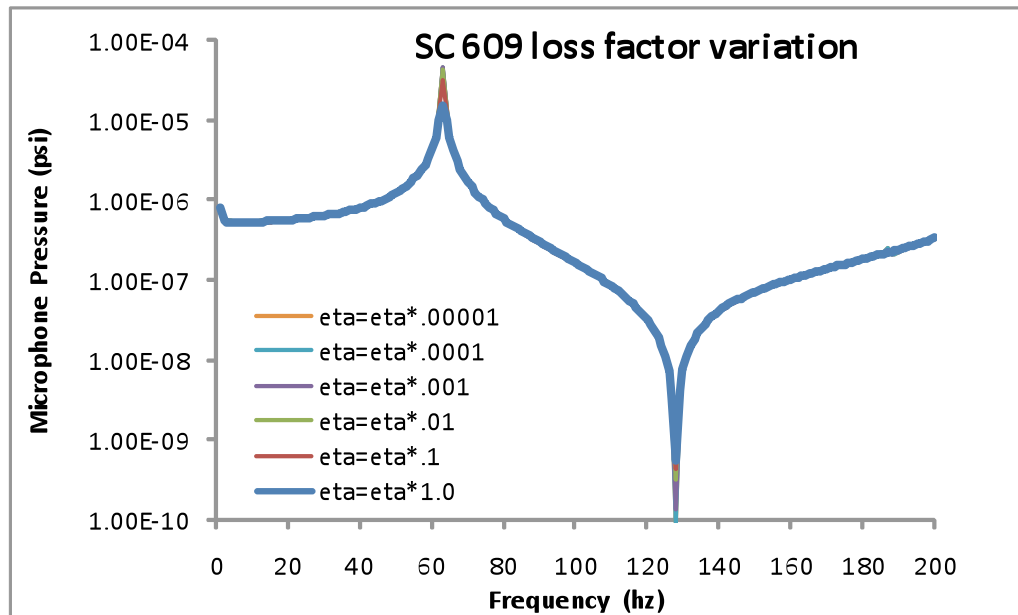


Figure 7. 2c: Pressures predicted in the acoustic cavity using MFLFE and parametric variation of loss factor in the viscoelastic layer for SC 609

As in the case of SC 601, increasing the value of viscoelastic density for SC 609 causes the frequency of the first resonant peak to decrease, while decreasing the value of the loss factor causes the amplitude of the first resonant peak to increase though the frequency remains constant.

The significant difference in the sensitivity to variation in the material properties for SC 609 compared to SC 601 can be understood by looking at the nomographs for the two materials. Nomographs plot a family of curves for various temperature and frequency ranges in a single curve, providing a concise data set that is useful for a wide range of temperature and frequencies. Viscoelastic materials typically exhibit three distinctly different behaviors depending on the temperature of the material. At the lowest temperatures the material is quite stiff. This is referred to as the "glassy

region." At the highest temperatures, the material is very flexible and soft. This region is the "rubbery region." The temperature range between the highest temperatures and the lowest temperatures is called the "transition region" and it is here that the loss factor takes its highest value. In Figures 7.3a and 7.3b the temperature -frequency region applicable to the experimental conditions is shown in a red box for SC 609 (Figure 7.3a) and in a blue box for SC 601 (Figure 7.3b). It can be seen that while the environmental conditions are in the transition region for SC 601, SC 609 is in its glassy region for the environmental conditions.

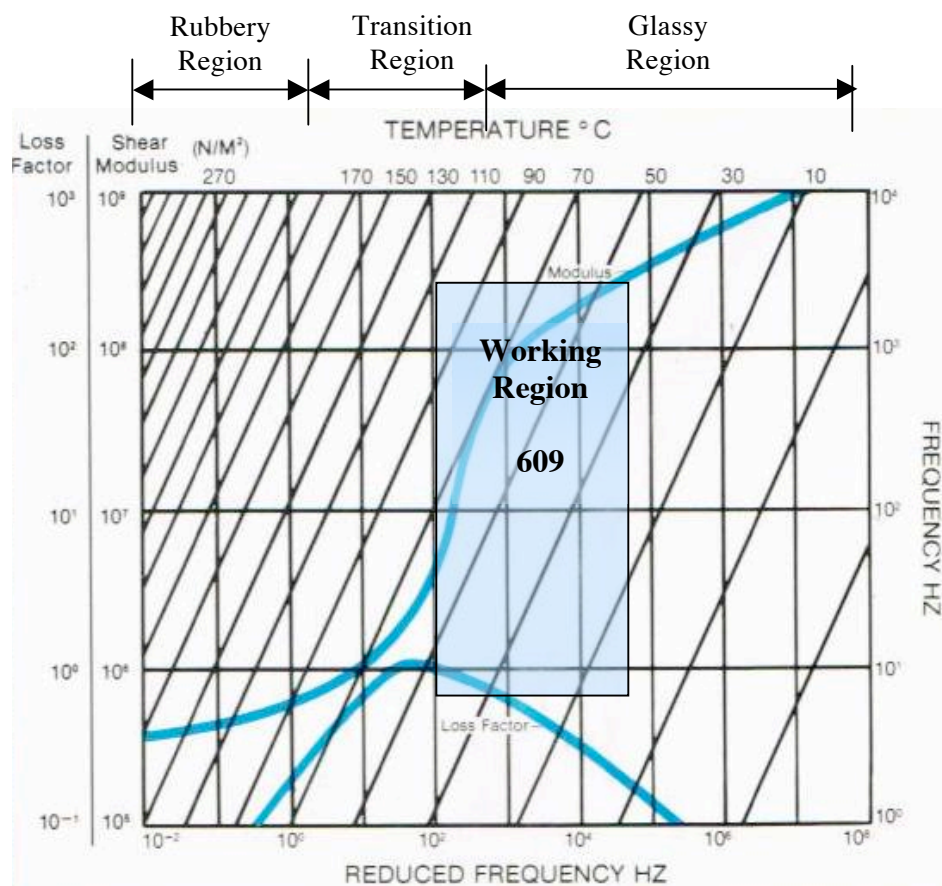


Figure 7. 3a: Sketch of the nomograph for SC 609. Working region for experimental frequency range and temperature shown in red box

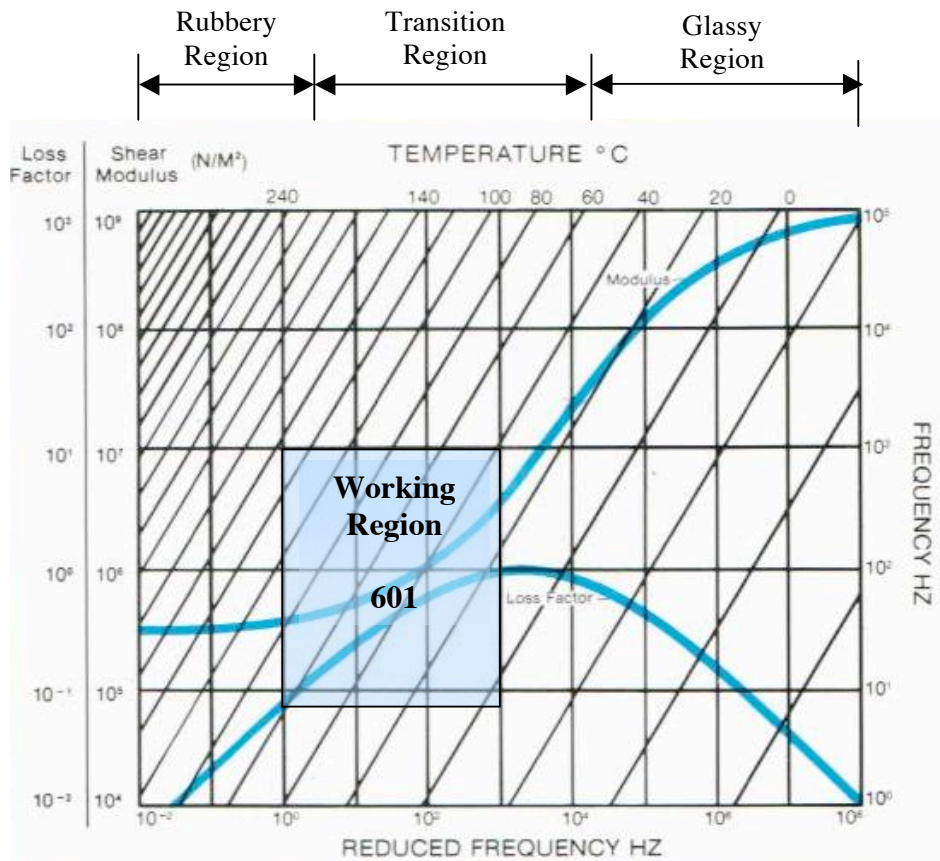


Figure 7. 3b: Sketch of the nomograph for SC 601. Working region for experimental frequency range and temperature shown in blue box

The data from the parametric study of material property variation for single material constrained layer treatment suggest that stiffness variation in the system can potentially have significant effect on the pressure field in the acoustic cavity. This implication adds impetus to the investigation of how changing the overall stiffness of the system by using a multiple material constrained layer treatment affects the pressure field in the acoustic cavity.

7.3 Geometric Layouts

In all cases, the flexible plate was treated by applying a 6 inch square patch that was applied to the center of the plate. Comparison was made between the sound pressures measured inside the cavity behind a plate treated by a square single material patch and those behind a plate treated with a square multi material patch.

The layouts were designed to place material with a high shear modulus in the region of highest shear displacement, on the edge of the treatment. Also, the question of whether there was any degradation or improvement in performance when the layout was asymmetrical along one of the axes was addressed by developing appropriate geometric combinations. As mentioned above, the range of geometric layouts possible to model with MFLFE is constrained to those that can be built using rectangles.

Figure 7.4 presents the geometric layouts investigated in this study. In each configuration, the red area denotes the stiffer material and the blue area indicates use of the softer material. Though by no means an exhaustive collection of all possible geometric permutations, the layouts represent a selection to possibilities that give an indication of which layouts are likely to be effective.

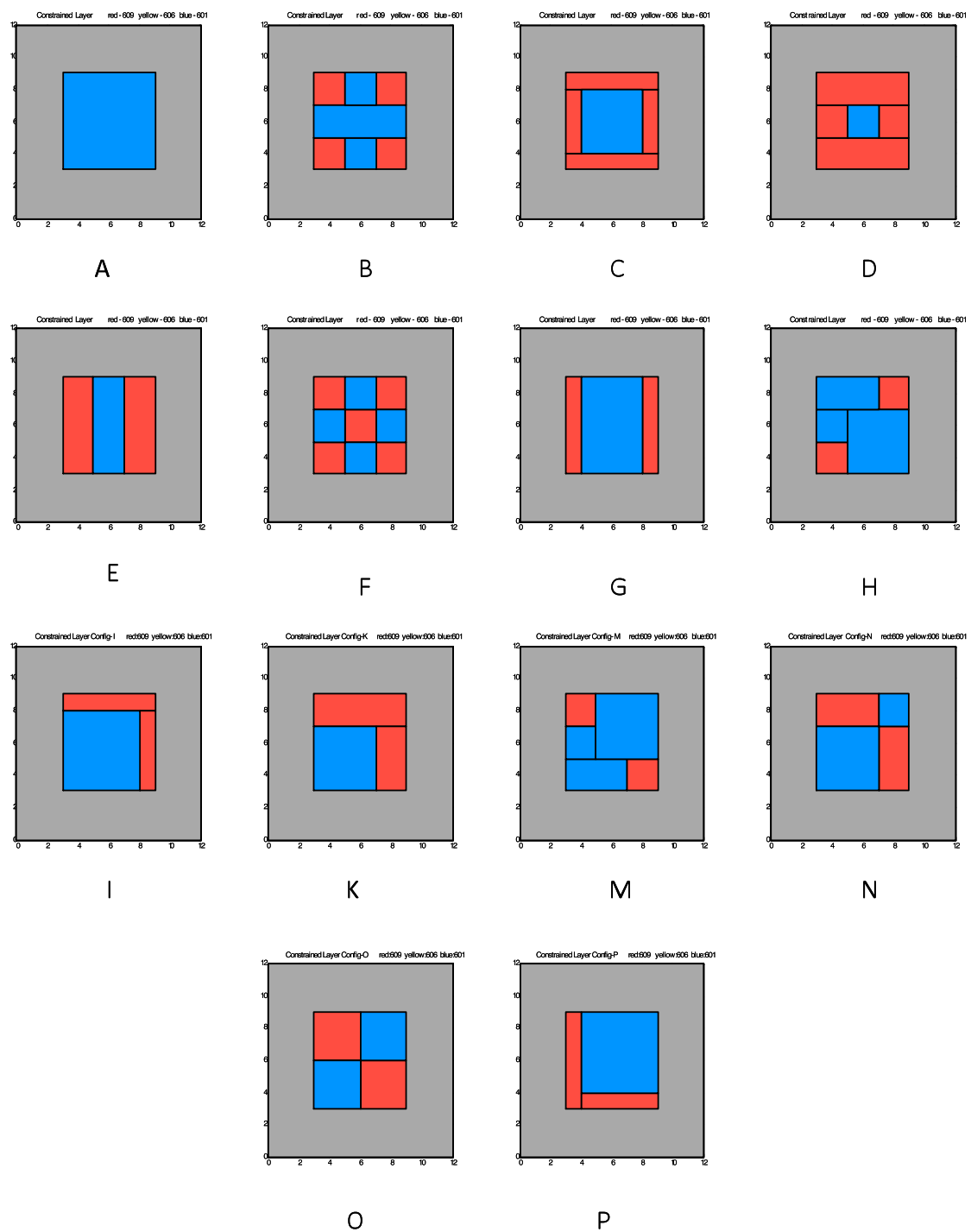


Figure 7.4 Geometric layouts of the multi-viscoelastic material treatments (red = stiff material, blue = soft material)

7.4 Mixed Material Parametric Study Results

The program MFLFE was used to calculate the pressure field in the acoustic cavity for the above collection of mixed material layouts. Figure 7.5 shows pressure field data for the full frequency spectrum and a zoom in the frequency range of the first resonant peak.

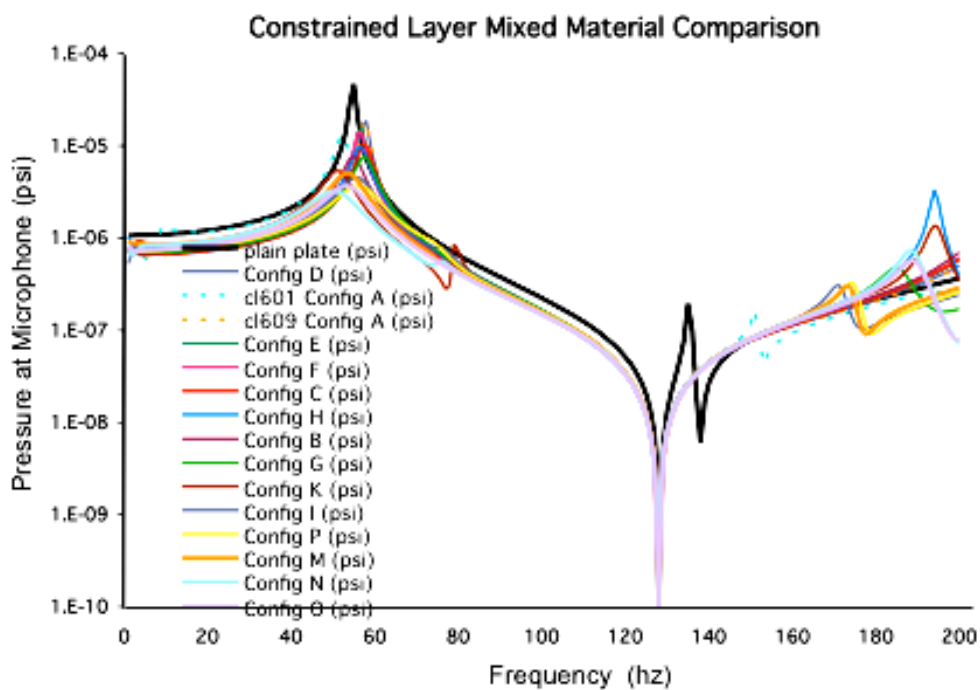


Figure 7.5a: Mixed material configuration calculated pressure spectra (full frequency range)

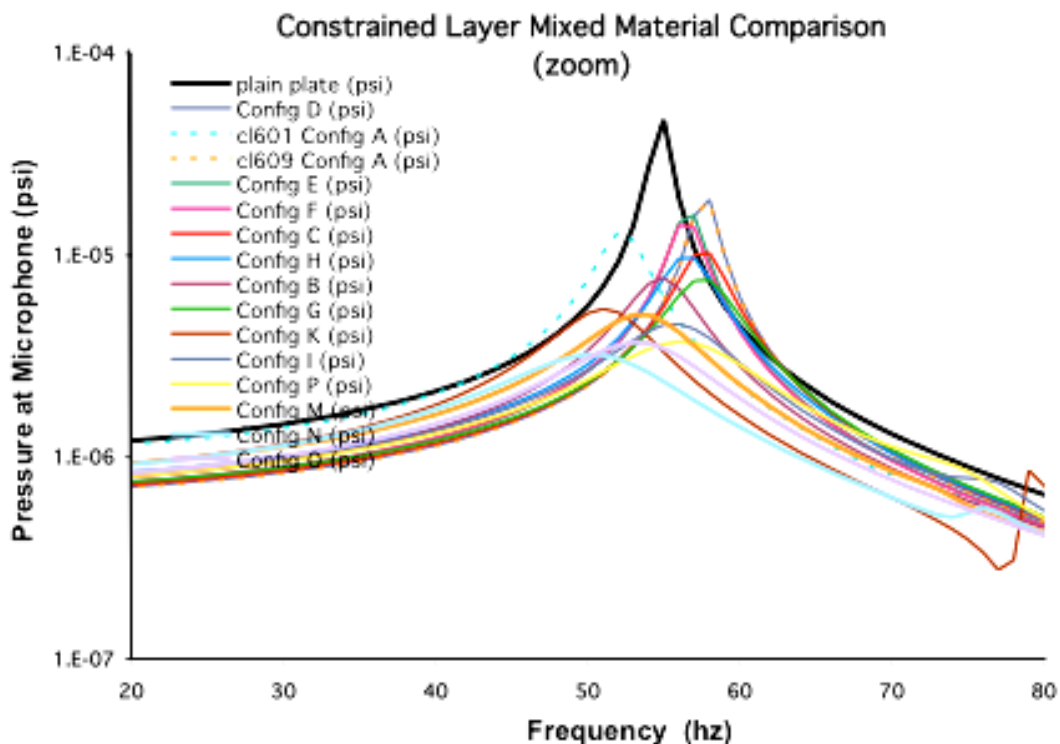
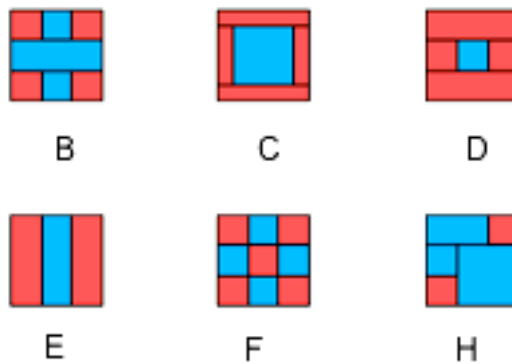


Figure 7.5b: Mixed material configuration calculated pressure spectra (zoom)

The plots in Figure 7.5 compare the pressure data of an untreated plate (black curve) to those of the single material treatment (Configuration A 601 and Configuration A 609 - dashed curves) and the multiple material treatments (Configurations B-P - solid color curves). In Figure 7.6, the zoomed curves have been divided among two plots (a) and (b) according to their effectiveness in lowering the pressure in the acoustic field. (Configuration H has been included on both graphs to facilitate comparison).



Less Effective Configurations

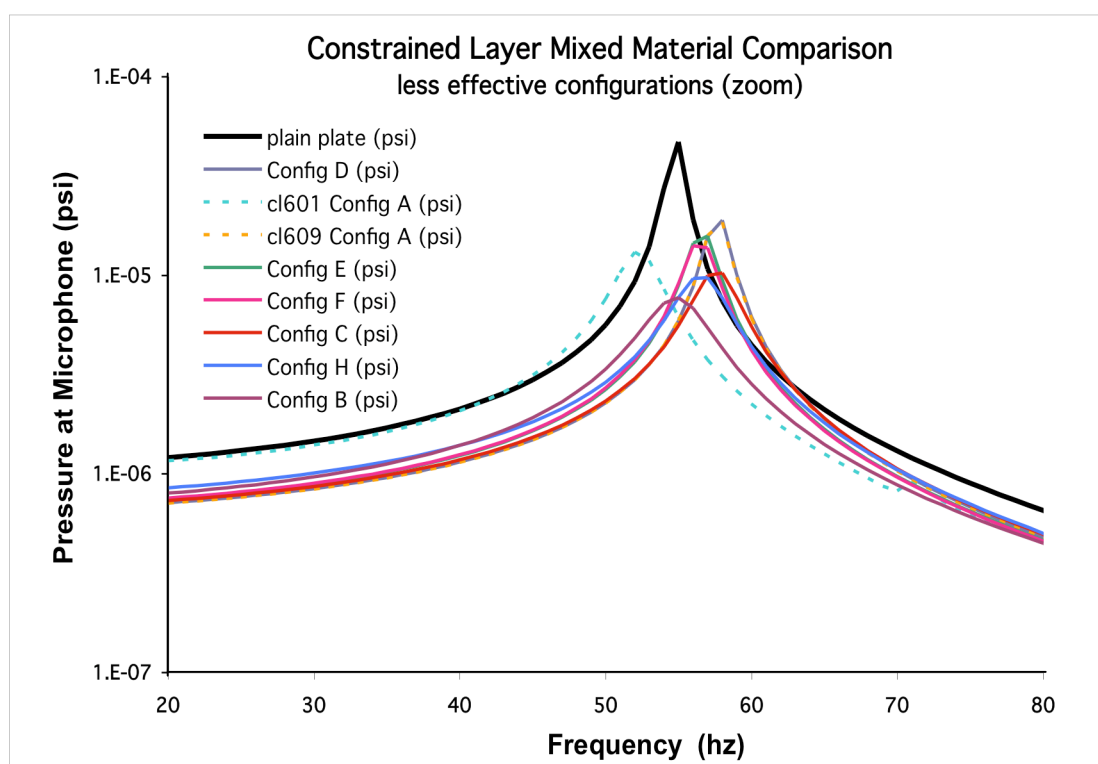


Figure 7. 6a: Sorted mixed material configuration calculated pressure spectra (zoom)

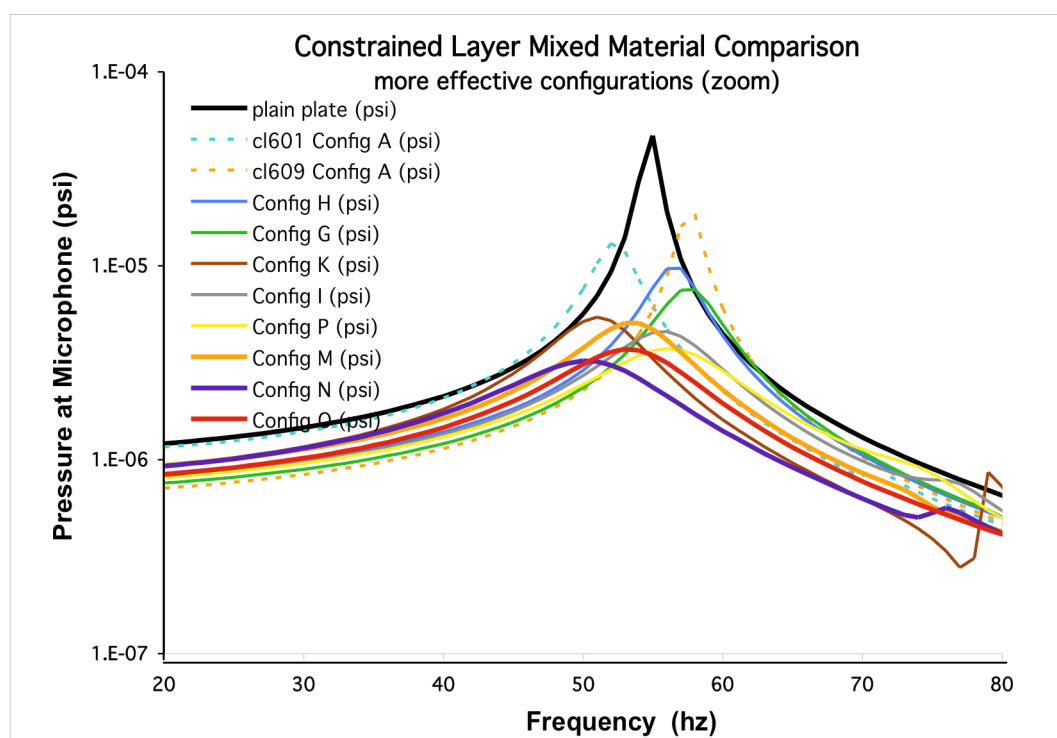
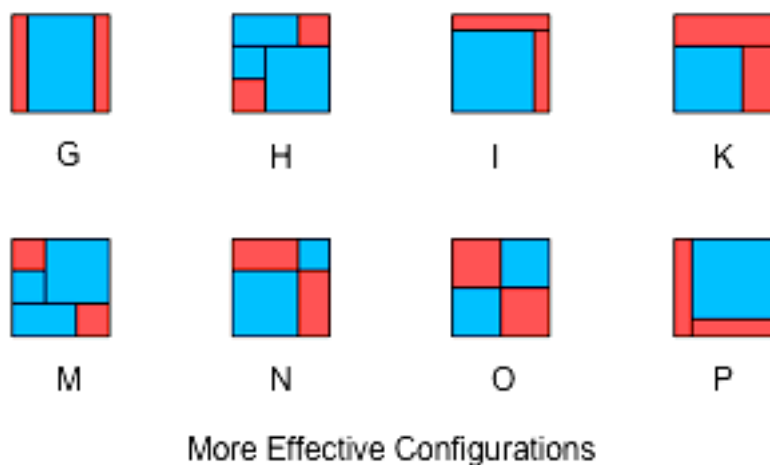


Figure 7. 6b: Sorted mixed material configuration calculated pressure spectra (zoom)

7.5 Displacements, Pressure Contours, and Strains

The program MFLFE was used to produce contour plots of the out of plane displacements at the frequency of the first resonance in the treated region for the geometric layouts shown in Figure 7.4. These plots are displayed in Figure 7.7.

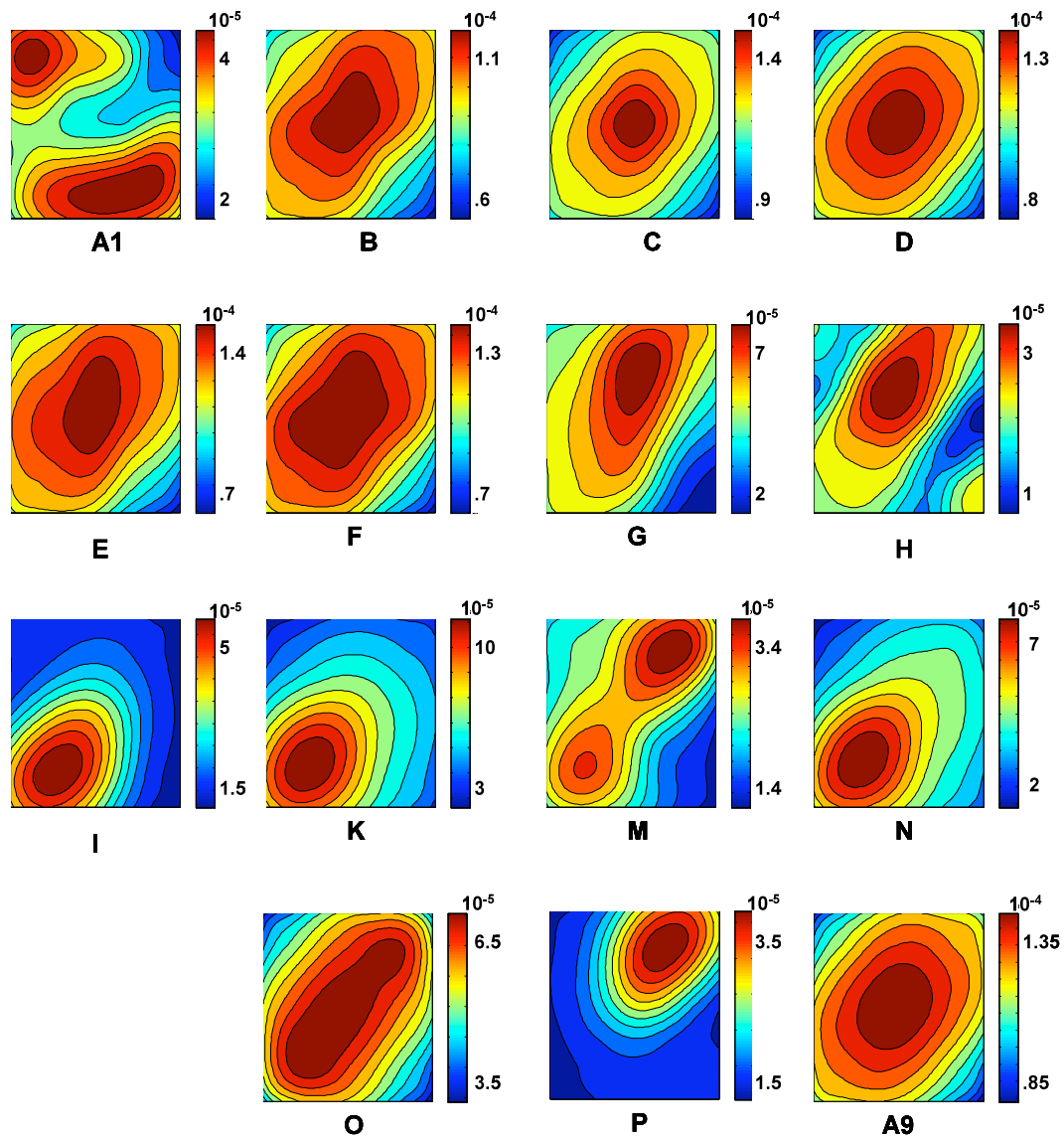


Figure 7.7: Out of plane displacements predicted by MFLFE in the treated region for various geometric layouts

It can be seen in Figure 7.7 that for the configurations which were more effective in lowering the first resonance peak, the spatial pattern of the displacements is moving away from the first mode (the "drum" mode), which, since it effectively acts as a monopole, is a highly effective acoustic radiator. The spatial distributions of out-of-plane displacements for the effective configurations are more like the second mode shape which is closer in character to a dipole distribution of sources. This would account for their success in lowering the first resonance peak as dipole sources radiate sound much less efficiently than monopole sources. Note that the single material SC 601 patch (labeled *A1* in Figure 7.7), which was more effective at reducing the first resonant peak than the single material SC 609 patch, displays the dipole character in its spatial displacement contour plot while the SC609 patch (labeled *A9* in Figure 7.7) displays a monopole-like character.

To enable visualization of the modes in the longitudinal direction the pressure distribution along the length of the acoustic cavity is presented in Figure 7.8 for four frequencies between 0 and 200 including the frequency at which the first resonant peak appears in the frequency spectrum (57 Hz). Below each plot, a cut along the z direction is given for $y=6$ to illustrate the amount of variation of pressure (P) that occurs along the length of the box. It can be seen that for most of the acoustic cavity the pressure is almost constant in the y direction, although close to the plate in the nearfield there is some variation along the y axis. For low frequencies, the increase in z is monotonic with the maximum pressure at the end of the cavity opposite the flexible plate because of the rigid boundary condition there. As the frequency increases, the next mode

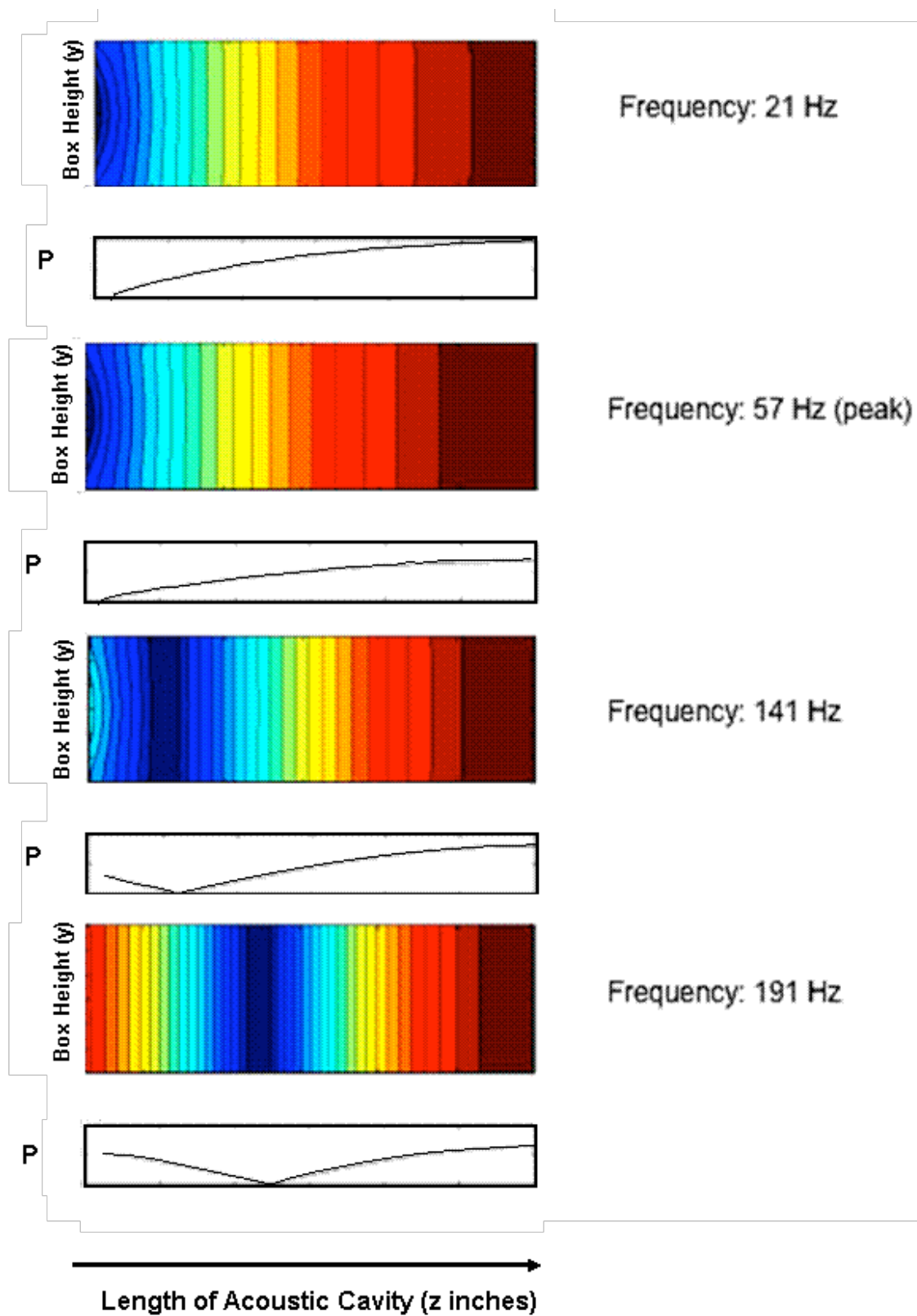


Figure 7. 8: Pressure contour plots in the yz direction calculated by MFLFE.

appears and its null moves up the z axis as the frequency increases. These plots were made for the single material SC 609 configuration but the same general spatial characteristics appear in the yz plane for yz contour plots of all of the single and multimaterial configurations.

Pressure contour plots made for the xy plane of the microphone location are presented in Figure 7.9 for the two single material configurations ($A1$ and $A9$), a less effective configuration (C) and for three of the most effective multimaterial configurations (H , P and I). A white circle on each of the contour plots gives an approximate location of the microphone in the plane. A number of observations may be made after inspection of these plots. First, in accordance with Bernoulli's principle, we can see that the magnitude of the pressure is lowest in the center where the velocity of the air moved by the plate is greatest.

Next, it is noticeable that the pressure field is not constant in the xy plane. Thus some of the variation in the magnitude of the first resonant peak is attributable to the spatial variation of the pressure within the xy plane. For example, although the P and I configurations are rotated versions of one another, the microphone, which is located off center, will register higher levels in one case than in the other. Note however, that although there is spatial variation in pressure level, it is not large - ranging between 0.8 and 1.6 percent (difference between min and max over max) for the xy planes of each configuration

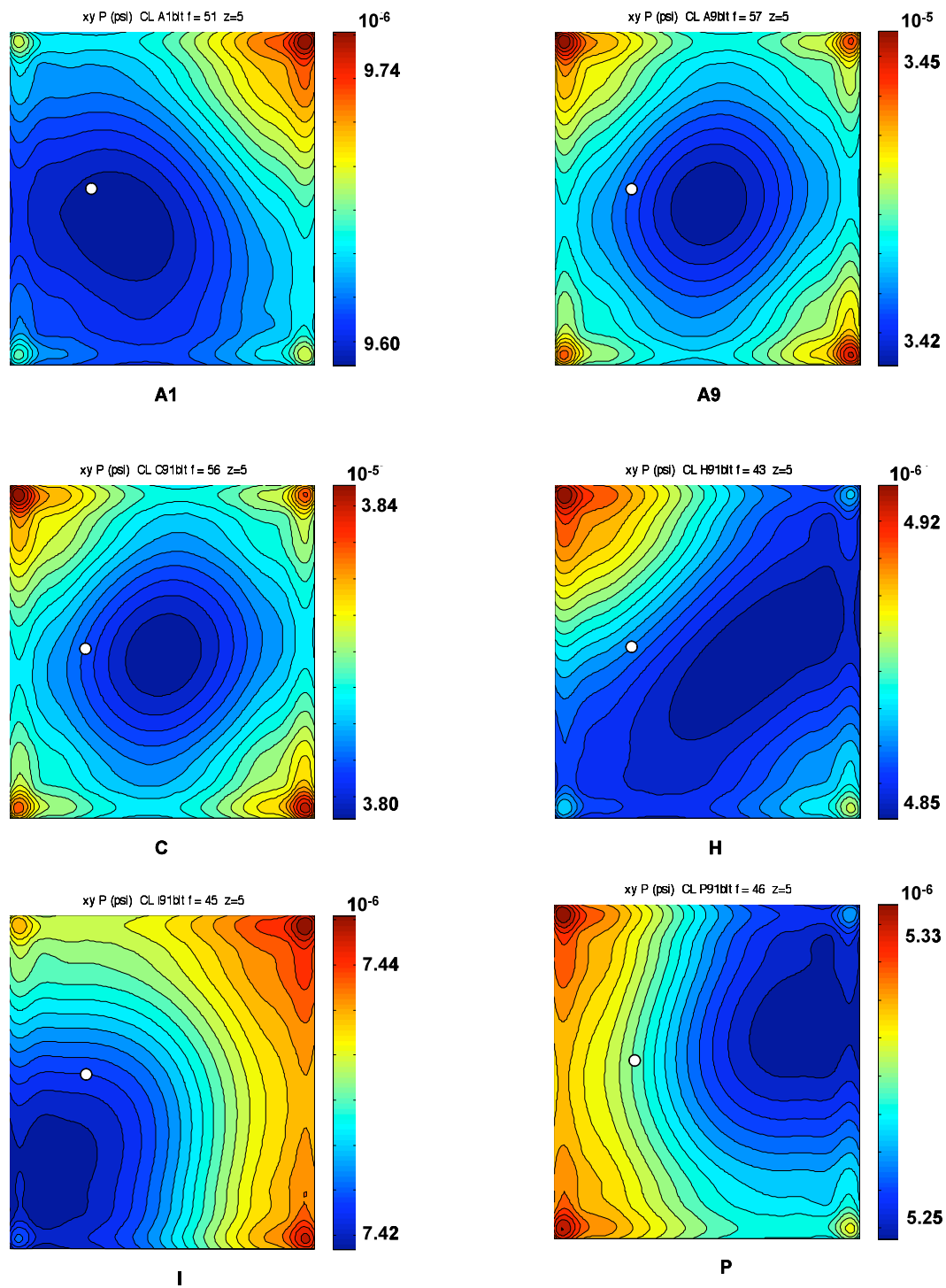


Figure 7. 9: Pressure contour plots in the xy plane at the microphone position. White circle indicates microphone location.

To rank the configurations as to their effectiveness, all the pressures in the acoustic cavity were summed. Since all configurations had the same number of pressure points, this is equivalent to calculating a spatial average of pressure for the cavity. The configuration was considered more effective if the sum of the pressures was lower than that of another configuration. From least to greatest, the configuration pressure sum order was : *H-P-I-M-AI-N-G-O-K-D-B-E-F-A9-C*.

This ranking order is similar but not exactly the same as that developed by looking at the pressure frequency spectra for the microphone. The variation between the two rankings can be attributed to spatial differences in the yz plane as discussed above.

To investigate the hypothesis that higher strain was occurring in the region with the stiffer material, the strain energy

$$U(x,y)_{visco} = G^*(x,y)[\gamma_{xz}^2(x,y) + \gamma_{yz}^2(x,y)]$$

was calculated for each point in the viscoelastic layer. Contour plots of the results are shown in Figure 7.10.

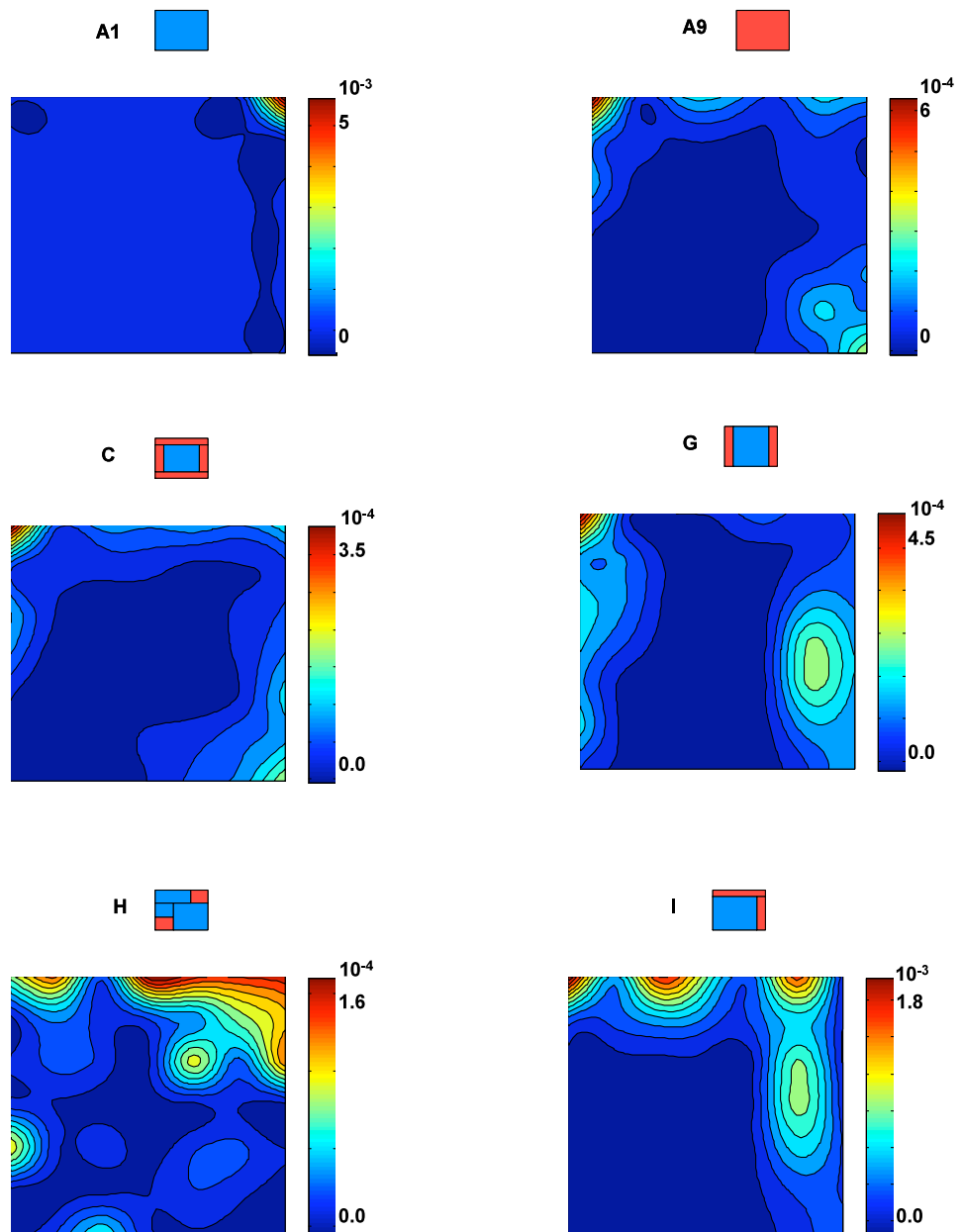


Figure 7. 10: Strain energy calculated on the plate for various configurations

The plots confirm that indeed the strain energy is higher in the region of the stiffer material in the viscoelastic layer as predicted,

7.6 Summary

The program MFLFE was used to calculate the pressure field for single and multiple material constrained layer treatments. Single material parametric variation highlighted the sensitivity of the system to the stiffness value of the softer material. A number of different geometric layouts for the multiple material constrained layer treatment generated encouraging results for using this technique to decrease the magnitude of the acoustic pressure field for this system.

It can be seen that many of the mixed material configuration hold promise of improved performance in decreasing the magnitude of the pressure field for the system when compared to the single material pressure spectra. It appears that in general there is an optimal limit to the width of the stiff material and that layouts which are not fully symmetrical about the center are usually more effective in reducing the pressure within the acoustic cavity. This is correlated with the fact that the treatments that are not symmetric about the center develop displacement patterns that will not radiate as a monopole. It would prove useful in future work to investigate the development of optimal expressions for geometric layouts of multiple material constrained layers and extend the observations that can be arrived at from the collection of layouts used in this study

Chapter 8

More Experimental Validation of Finite Element Model of Plate/Cavity System

8.1 Experimental Setup

The final experimental data was gathered using the system that was used for the preliminary experiment. It is fully described in Chapter 4 but basically consists of a 5 sided Plexiglas cavity that is closed on one end with a flexible aluminum plate which is bolted to the Plexiglas cavity (Figure 4.1). A microphone inside the cavity monitors the internal pressure, an external microphone tracks the ambient noise environment and a laser doppler velocimetry (LDV) apparatus enables the collection of plate displacement data.

The two photographs shown in Figure 8.1 depict the experimental setup. The LDV system is not shown here, but when it is being used it is positioned behind the Plexiglas cavity, on the end of the cavity that is opposite the flexible plate and speaker.

To ameliorate the problem, a heat gun was turned on the material as it was being cut so that the material became slightly softer. On the other hand, the soft Soundcoat 601 material tended to stretch as it was cut at room temperature. To cut it as precisely as possible, the material was pinned beneath a metal straight edge as it was being cut. The cut edges were filed and sanded to make as tight a fit as possible. The viscoelastic

materials were then bonded to the flexible plate using a two-part epoxy which is sold for use with the Soundcoat materials.

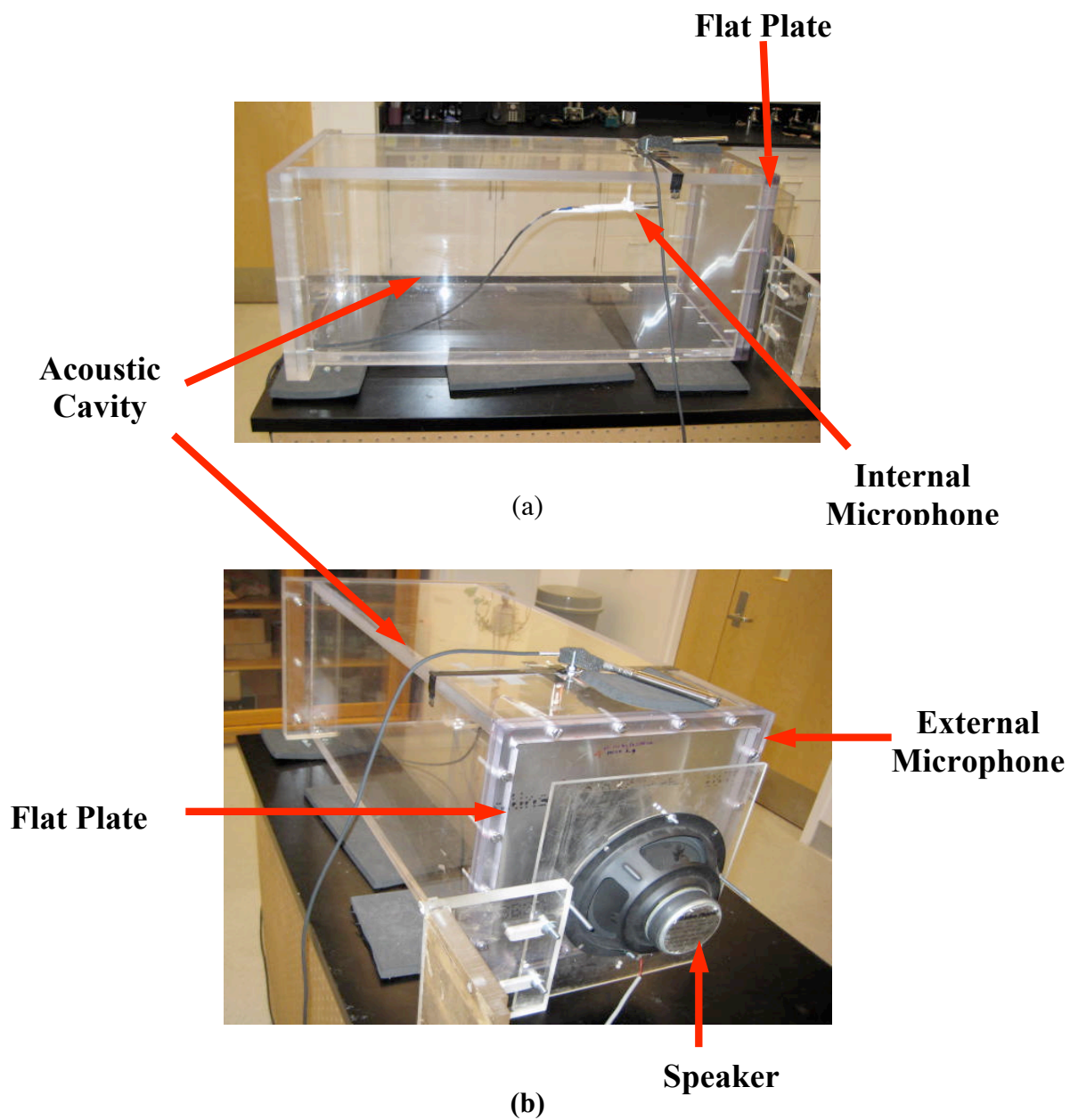


Figure 8.1: Experimental apparatus includes internal microphone, external microphone, flexible plate, Plexiglas cavity, and source speaker

Creating multi-material constrained layers posed several challenges. Cutting the stiff Soundcoat 609 material was difficult because the material was quite stiff at room temperature. According to manufacturer's guidelines, the epoxy takes 24 hours to set up. In practice, the material did not fully cure for at least 48 hours. Sound pressure spectra for plates with a bonded treatment that were measured before 48 hours had passed showed considerable variation. After 48 hours had passed since the application of the epoxy, measurements of the pressure spectra remained consistent. Bonding the viscoelastic pieces to the plate and to each other for each configuration required careful attention to the removal of air bubbles that can become trapped inside the bonding layer. The last step in creating the constrained layer multi-material treatment involved bonding the constraining layer to the viscoelastic material after the first epoxy application had cured. Since the constraining layer is opaque, air bubble removal was even more difficult than it was when applying the viscoelastic layer to the plate.

Because of the difficulty in manufacturing constrained multi-material viscoelastic layers in the laboratory that had small tolerance fit between pieces and no trapped air bubbles, only two of the most effective geometric layouts were tested. These configurations were: Configuration I and Configuration G which are shown in Figures 7.3 and 8.2. Note that Configuration G is the two dimension analog of the configuration used by Baz et al.'s (2003) beam experiment with mixed materials which is shown in Figure 1.1.

Sound pressure spectra were collected for the untreated plated and then for the constrained layer configurations.

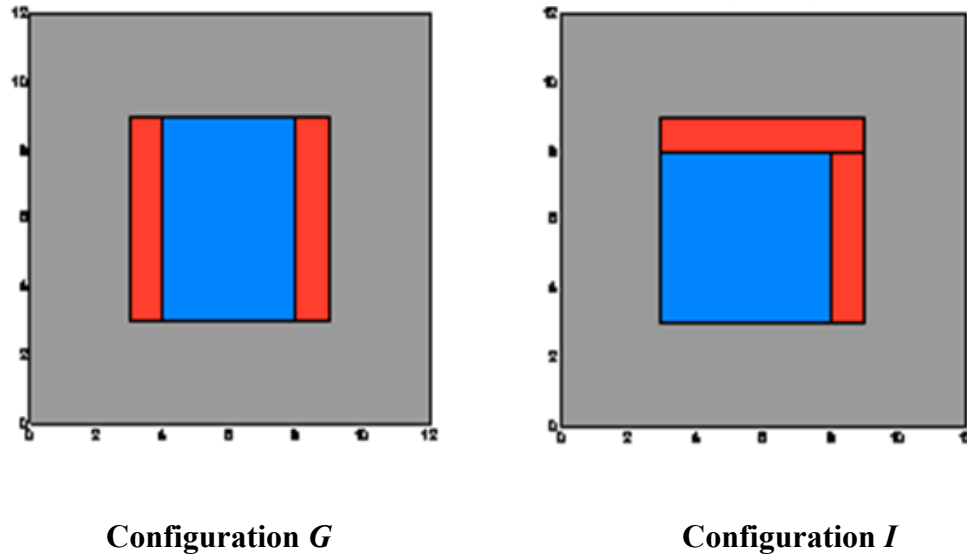


Figure 8. 2: Mixed material configurations used in final experiment

8.2 Experimental Results

The results for the final experimental data are shown in Figures 8.3 a-c. Figure 8.3a shows a comparison of the experimental constrained layer pressure spectra for the stiffer single material SC 609, the softer single material SC 601, the mixed material configuration G and the mixed material configuration I.

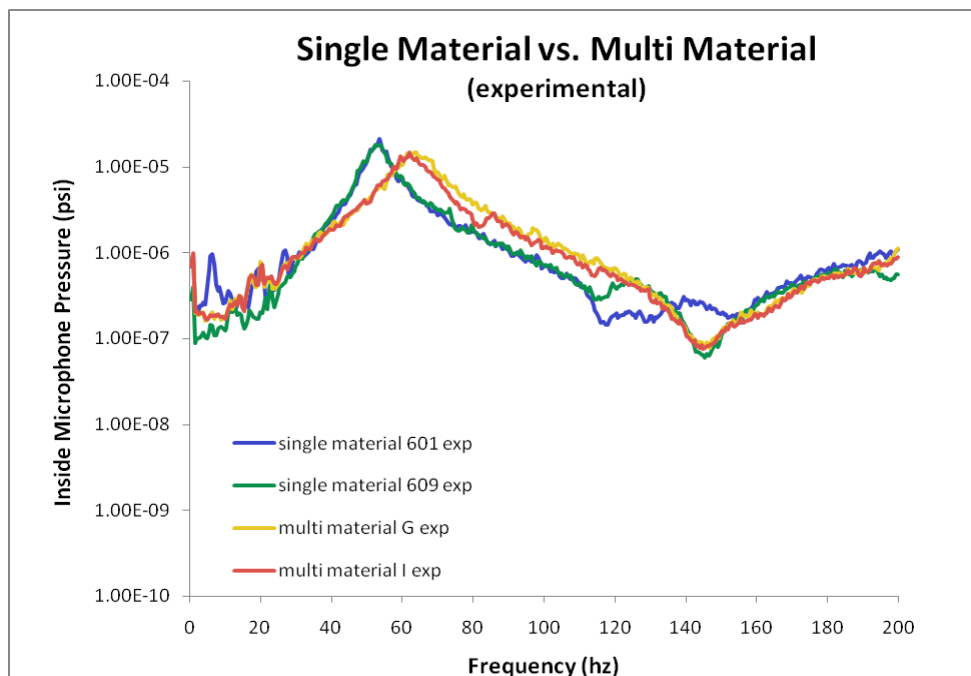


Figure 8. 3a: Comparison of the experimental sound pressure spectra for constrained layer treatments, for both single material and mixed material viscoelastic cores.

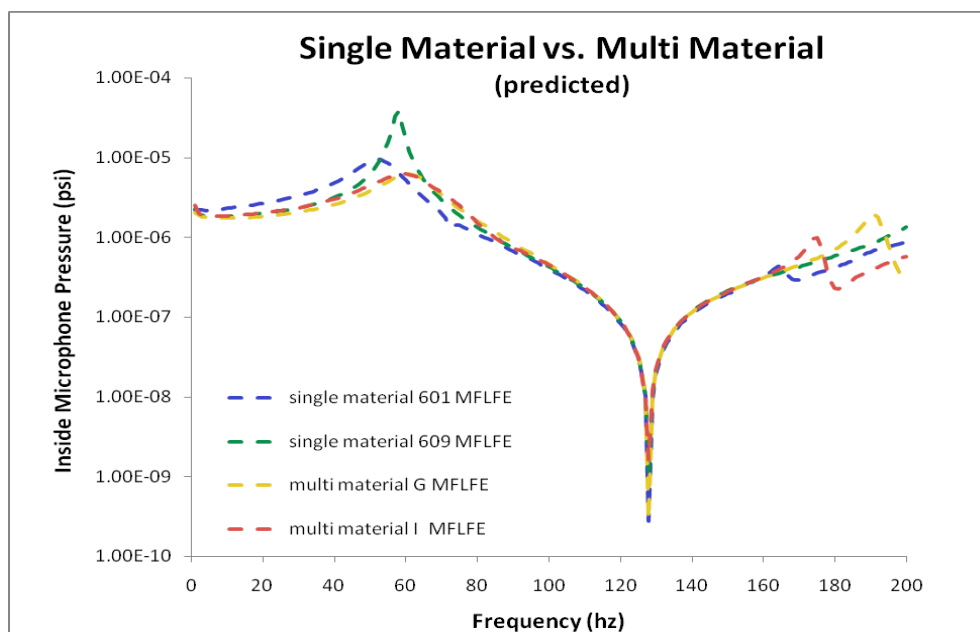


Figure 8.3b: Comparison of the predicted (MFLFE) sound pressure spectra for constrained layer treatments, for both single material and mixed material viscoelastic cores

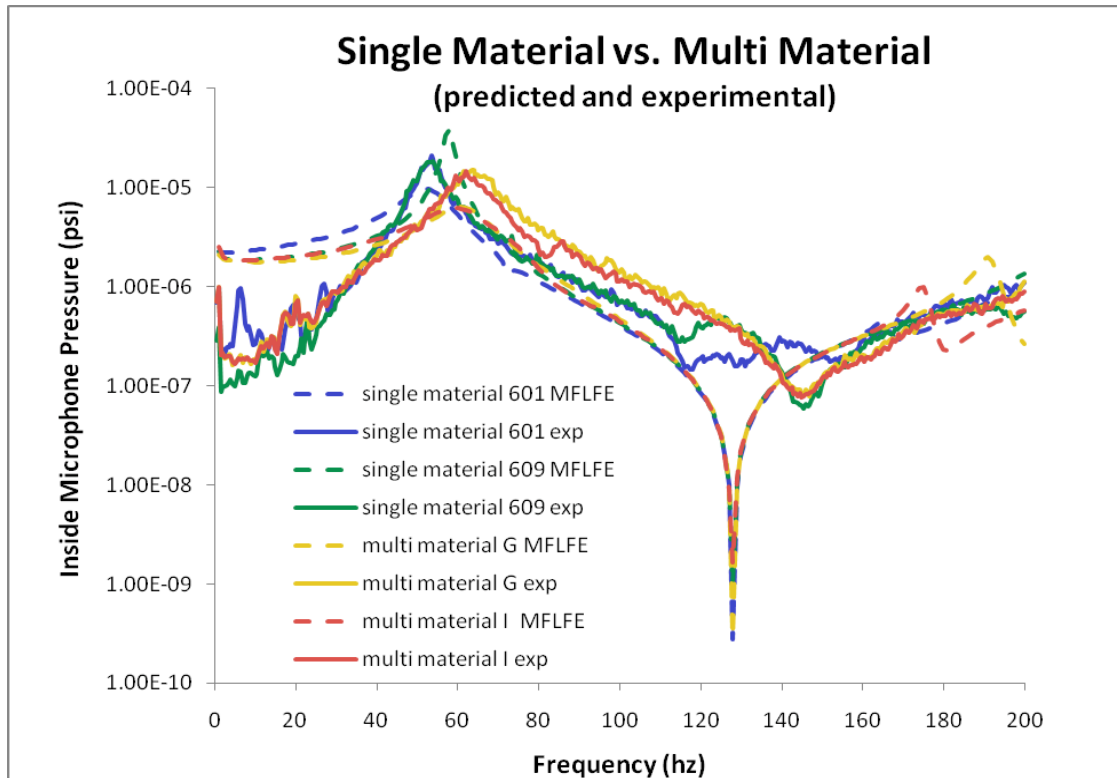


Figure 8.3c: Comparison of the predicted (MFLFE) and experimental sound pressure spectra for constrained layer treatments, for both single material and mixed material viscoelastic cores

Figure 8.3b shows a comparison of the constrained layer pressure spectra predicted by MFLFE for the stiffer single material SC 609, the softer single material SC 601, the mixed material configuration G and the mixed material configuration I.

For the sake of completeness both the experimental and predicted sets of curves are displayed in Figure 8.3c. It can be seen that as predicted by MFLFE, a decrease in the pressure spectrum occurred at the first resonant peak when a multi-material treatment was used. MFLFE predicted that the mixed configuration peak would occur close to the same frequency as the SC 609 resonant peak. The experiment showed a shift in the mixed material peak, but the SC 609 peak remained at the same frequency as the SC601 peak. The experiment also showed a mid frequency range (70 to 120 Hz) increase in

amplitude of 3 to 5 dB that was not predicted by MFLFE for the multi-material configurations. Finally the amplitude of the SC 609 single material treatment was greater in amplitude in the prediction than in the experiment. The differences are likely the result of a number of factors. First, the validation experiment was done in a different location than the preliminary experiments. The current location has a centrally controlled air conditioning system with a noisy blower which cannot be turned off during data collection. The air conditioning system also dropped the room temperature 10 or more degrees below the temperature specified for viscoelastic material properties provided by the manufacturers. Finally, the difficulties discussed above in creating a multi material layer may have contributed to differences between predicted and measured spectra. Overall, however, the experiment verifies the prediction of MFLFE that the mixed material configurations would produce a decrease in the first resonant peak of the pressure spectrum.

8.3.. Summary

The chapter has presented an experimental validation of the effectiveness of the multi-viscoelastic material configurations in attenuating the sound pressures generated by the coupling of a vibrating flexible plate and an acoustic cavity. Furthermore, comparisons have also been presented between the experimental results and the theoretical predictions using the developed finite element model (MFLFE). Close agreements are evident between theory and experiments.

Chapter 9

Conclusions and Recommendations

9.1..Conclusions

A multi-material constrained viscoelastic layer is shown to be more effective in decreasing the low frequency sound pressure field than a single-material constrained layer. This improved performance can be leveraged into weight savings for noise treatments of enclosed cavities.

A new *Reissner-Mindlin* plate type finite element has been developed. This element, which enables the modeling of multi-material constrained viscoelastic layers. The element combines the contributions from the three layers of a constrained layer damping treatment to the strain energy to give accurate predictions of a system treated with a multi- material constrained layer. The element incorporates extensional, bending and transverse shear energy for each of the three layers into the stiffness matrix. The element has also a fully consistent mass matrix which has been designed to account for coupling between the extensional and bending displacements.

A finite element program that uses the new three layer element along with untreated *Reissner-Mindlin* plate elements, coupling elements and solid-fluid elements was developed and used to model the fluid-structure interactions between a flexible plate

coupled with an acoustic cavity. Sound pressure spectra were predicted by this program for systems with an untreated plate, with a plate treated with a single-material constrained layer, and with a plate treated with a multi-material constrained layer. Agreement between a preliminary experimental data set and the predicted data set was good.

A parametric study was performed using the developed finite element code MFLFE. The obtained results indicated that a multi-material constrained layer had the potential to outperform the single-material constrained layer treatment in attenuating sound radiation into acoustic cavities. An experiment validated the trend indicated by the parametric study. The imperfect agreement in amplitude between experimental and predicted results is attributed to lower ambient temperatures which affected the treatment's material properties and difficulty in manufacturing the multi-material treatment in the laboratory.

9.2 Recommendations

This dissertation has presented invaluable theoretical and experimental tools for the design and predictions of sound radiation by plates treated with spatially varying damping treatments into coupled acoustic cavities. However, the developed tools can be easily extended to more complex structural/cavity systems such as automobile, aircraft, and helicopter cabins as well as ship hulls.

Although the emphasis in this dissertation has been on the use of damping treatments made of bi-viscoelastic materials, the presented theory can be directly applied

to viscoelastic cores consisting of multi-viscoelastic materials. Such an extension is a natural extension to the examples presented in this dissertation.

Also, this work has targeted mainly the first modes of vibration of the flexible plates and the placement of the multi-viscoelastic material core has been limited accordingly to the center of the plate. Further work is needed to optimize the location of the multi-viscoelastic material core to target multi-modes of vibrations. Such an extension should also be validated experimentally.

The use of multi-material constrained layers in structural acoustic noise abatement would have most success if an improved method of construction of the multi-material viscoelastic core were developed. Also, better performance would have been obtained if the tests were carried out inside tightly temperature-controlled environment.

This dissertation has also opened the door for more extensive studies on the use of viscoelastic cores with functionally graded properties both in-the-plane and across the thickness.

REFERENCES

Aboudi, J., M.J. Pindera, S.M. Arnold, "Higher Order Theory for Functionally Graded Materials," *Composites Part B:Engineering*, Vol. 30, pp.777-832, 1999.

Bathe, K.J., *Finite Element Procedures*, Prentice-Hall, Upper Saddle River, New Jersey, 1996.

Bathe, K.J. and E.N. Dvorkin, "A Four Node Plate Bending Element Based on Mindlin/Reissner Plate Theory and a Mixed Interpolation," *International J. for Numerical Methods in Engineering*, Vol. 21, pp. 367-383, 1985.

Baz, A. and J. Ro, "Finite Element Modeling and Performance of Active Constrained Layer Damping," *Proc. 9th VPI & SU Symposium Dynamics and Control of Large Structures (Blacksburg, VA)*, pp. 345-357, May 1993.

Baz, A. and J. Ro, "Vibration Control of Plates with Active Constrained Damping," *Smart Materials and Structures*, Vol. 5, pp. 272-280, 1996.

Bigili, E., "Computer Simulation as a Tool to Investigate the Shearing Deformation of Nonhomogeneous Elastomers." *J. Elastomers and Plastics*, Vol. 34, pp. 239-264, Jul 2003.

Cremer, L., Heckl, M. and Ungar, E. E., *Structure-Borne Sound*. 1988, Springer-Verlag, NY.

Flugge, W., *Handbook of Engineering Mechanics*, McGraw-Hill, New York, New York, 1962.

Hoff, N. J. and S. E. Mautner, " Bending and Buckling of Sandwich Beams," *J. Aeronautical Sciences*, Vol. 12, No. 1, pp. 707-702, Dec 1948.

Hughes, T. J. R., "Generalization of Selective Integration Procedures to Anisotropic and Nonlinear Media," *International J. Numerical Methods in Engineering*, Vol. 15, pp. 1413-1418, 1980.

Hughes, T.J.R. and T.E. Tezduyar, "Finite Elements Based upon Mindlin Plate Theory with Particular Reference to the Four Node Bilinear Isoparametric Element," *J.I of Applied Mechanics*, Vol. 48, pp. 587-596, 1981.

Johnson, C. D. and D. A. Kienholz, "Finite Element Prediction of Damping in Structures with Constrained Viscoelastic Layers," *AIAA Journal*, Vol. 20, No. 9, pp. 1284-1290, Sep. 1982.

Kao, J.S., "Axisymmetrical Deformation of Multi-Layer Circular Sandwich Cylindrical Shells," *J. Franklin Institute*, Vol. 282, No. 1, pp. 31-41, Jul. 1966.

Kao, J.S. and R.J. Ross, "Bending of Multilayer Sandwich Beams," *AIAA Journal*, Vol.6, No. 8, pp. 1583-1585, Aug. 1968.

Kerwin, E. "Mechanisms and Measurement of Structural Damping," *Ship Silencing Symposium (Groton, CT)*, pp. 1021-1048, May 1963.

Kerwin, E., "Damping of Flexural Waves by a Constrained Viscoelastic Layer," *J. Acoustic Society America*, Vol. 31, No. 7, pp. 952-962, Jul 1959.

Kinsler, L., Frey, A., Coppens, A. and Sanders, J., *Fundamentals of Acoustics*, 4th Edition, John Wiley and Sons Inc., 1999.

Khatua, T.P. and Y. K. Cheung, "Bending and Vibration of Multilayer Sandwich Beams and Plates," *International J. Numerical Methods in Engineering*, Vol. 6, pp. 11-24, 1973.

Kim, J. H. and G. H. Paulino, "Isoparametric Graded Finite Elements for Nonhomogeneous Isotropic and Orthotropic Materials," *J. Applied Mechanics (ASME)*, Vol. 69, pp. 502-514, Jul 2002.

Lazan, G. J., A. F. Metherell, and G. Sokol," Multiple Band Surface Treatments for High Damping," *AFML-TR-65-269*, Sep. 1965.

Lesieutre, G.A. and E. Bianchini, "Time Domain Modeling of Linear Viscoelasticity Using Anelastic Displacement Fields," *J. Vibration and Acoustics (ASME)*, Vol. 117, pp. 424-430, Oct. 1995.

Lesieutre, G. A. and U. Lee, "A Finite Element for Beams Having Segmented Active Constraining Layers with Frequency-Dependent Viscoelastics," *Smart Materials and Structures*, Vol. 5, pp. 615-627, 1996.

Liaw, B. D. and R. W. Little, "Theory of Bending Multilayer Sandwich Plates," *AIAA Journal*, Vol.5, No. 2, pp. 301-304, Feb 1967.

Liu, G.R., X Han, K.Y. Lam, "Stress Waves in Functionally Gradient Materials and its Use for Material Characterization," *Composites Part B: Engineering*, vol. 30, pp.383-394, 1999.

MacNeal, R. H., "A Simple Quadrilateral Shell Element," *Computers and Structures*, Vol. 8, pp.175-183, 1978.

McTavish, D.J. and P.C. Hughes, "Modeling of Linear Viscoelastic Space Structures," *J. Vibration and Acoustics (ASME)*, Vol. 115, pp. 103-110, 1993.

Mindlin, R.D., "Influence of Rotary Inertia and Shear on Flexural Motions of Isotropic, Elastic Plates," *J. Applied Mechanics (ASME)*, Vol. 18, pp. 31-38, 1951.

Parfitt, G. G., "The Effects of Cuts in Damping Tapes," *4th International Congress of Acoustics (Copenhagen)*, pp.21-28, Aug. 1962.

Pindera, M.J. and P. Dunn, "Evaluation of the Higher Order Theory for Functionally Graded Materials via the Finite Element Method," *Composites Part B: Engineering*, 28B, pp. 109-119, 1997.

Plunkett, R and C.T. Lee, "Length Optimization for Constrained Viscoelastic Layer Damping," *J. Acoustic Society of America*, Vol. 48, No. 1 (Part II), pp. 150-161, 1970.

Reissner, E., "On Bending of Elastic Plates," *Quarterly of Applied Mathematics*, Vol.5, pp.55-68, 1947.

Ross, D., E. Ungar. and E. Kerwin, "Damping of Plate Flexural Vibrations by means of Viscoelastic Laminae," *Structural Damping (Section III)*, ASME, New York, pp.49-87, 1959.

Sutradhar, A., G.H. Paulino, L.J. Gray, "Transient Heat Conduction in Homogeneous and Non-homogeneous Materials by the Laplace Transform Galerkin Boundary Element Method," *Engineering Analysis with Boundary Elements (Elsevier)*, Vol 26, pp. 119-132, 2002.

Ventkataraman, S. and B.V. Sankar, "Analysis of Sandwich Beams with Functionally Graded Core," AIAA Paper 2001-1281.

Yiu, Y. C., "Finite Element Analysis of Structures with Classical Viscoelastic Materials," *Proc. 34th Structures, Structural Dynamics, and Materials Conference (La Jolla, CA)*, Vol 3, pp. 2110-2119, 1993.

Yiu, Y. C., "Substructure and Finite Element Formulation for Linear Viscoelastic Materials," *Proc. 35th Structures, Structural Dynamics, and Materials Conference (Hilton Head, SC)*, Vol 3, pp. 1585-1594, 1994.

Zienkiewicz, O.C., *Finite Element Method*, McGraw Hill, 1977.